

Infrared Spectroscopy and Nano-imaging of  $\text{La}_{0.67}\text{Sr}_{0.33}\text{MnO}_3$  Films

Peng Xu

Xi'an, China

Master of Science, College of William and Mary, 2010  
Bachelor of Science, Harbin Institute of Technology, 2008

A Dissertation presented to the Graduate Faculty  
of The College of William & Mary in Candidacy for the Degree of  
Doctor of Philosophy

Department of Physics

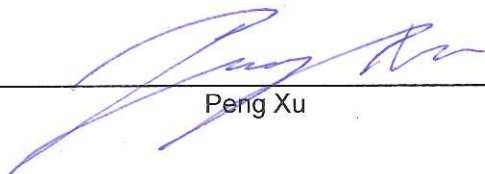
College of William & Mary  
August 2017



## APPROVAL PAGE

This Dissertation is submitted in partial fulfillment of  
the requirements for the degree of

Doctor of Philosophy



---

Peng Xu

Approved by the Committee, June, 2017



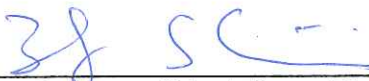
---

Committee Chair  
Associate Professor M. Mumtaz Qazilbash, Physics  
College of William & Mary



---

Professor Henry Krakauer, Physics  
College of William & Mary



---

Professor Shiwei Zhang, Physics  
College of William & Mary



---

Associate Professor Seth A. M. Aubin, Physics  
College of William & Mary



---

Adina Allen Term Distinguished Associate Professor Hannes C. Schniepp,  
Applied Science  
College of William & Mary

## ABSTRACT

Charge transport properties of manganites can be significantly modified by temperature, chemical doping, strain, and interfacial boundaries. In this dissertation, we report studies on broadband far-field infrared spectroscopy and near-field infrared imaging of single crystalline thin films of Sr doped manganite  $\text{LaMnO}_3$  at 0.33 doping level. At this Sr-doping level, the manganite films undergo a phase transition between a ferromagnetic metallic phase at low temperatures to a paramagnetic, insulating phase at higher temperatures. The films were grown on different substrates with different thicknesses by pulsed laser deposition method. The temperature dependent far-field infrared data on 85 nm thick  $\text{La}_{0.67}\text{Sr}_{0.33}\text{MnO}_3$  (LSMO) film grown on (100) lanthanum aluminate substrate reveals that electron and hole free carriers behave quite similarly in the low temperature ferromagnetic metallic state of the thin film. The number densities, effective masses and relaxation response of the delocalized electrons and holes are quantified. We discover that only one-third of the doped charges are coherent and contribute to the dc transport. The temperature dependence of the relaxation rate of the free carriers at low temperatures fulfills the formula  $A+BT^2$  with anomalously large  $A$  and  $B$  coefficients compared to a conventional metal like gold. We detected some of the 8 infrared-active phonons predicted for the rhombohedral lattice. We also observed splitting of the  $580\text{ cm}^{-1}$  infrared-active phonon at high temperatures which we attribute to the local Jahn-Teller distortion effect. We performed detailed scattering-type scanning near-field mid-infrared microscopy on an 18 nm thick  $\text{La}_{0.67}\text{Sr}_{0.33}\text{MnO}_3$  film grown on (100) strontium titanate substrate. In contrast to a percolative type first-order phase transition, a continuous, non-percolative phase transition is observed within the bulk of the thin film when this sample is heated up from room temperature to 330K. The infrared near-field amplitude data is consistent with a second order phase transition from the ferromagnetic metallic phase to the paramagnetic insulating phase. We discover critical fluctuations at a fixed temperature within the bulk of the thin film near its nominal phase transition temperature. We also discover temperature independent phase segregation near the film-substrate interface which we attribute to more conducting regions with A-type antiferromagnetic order coexisting with less conducting ones with C-type antiferromagnetic structure.

# TABLE OF CONTENTS

Acknowledgements.....	iii
Dedication.....	iv
CHAPTER 1: Introduction.....	1
CHAPTER 2: The manganite $\text{La}_{1-x}\text{Sr}_x\text{MnO}_3$ .....	7
2.1 Phase diagram .....	7
2.2 Lattice structure of $\text{La}_{0.67}\text{Sr}_{0.33}\text{MnO}_3$ .....	9
2.3 Crystal Field Splitting.....	11
2.4 Jahn-Teller Distortion .....	14
2.5 Double exchange.....	17
CHAPTER 3: Far Field Experimental Methods.....	27
3.1 Fourier Transform Infrared (FTIR) spectroscopy .....	27
3.2 Variable Angle Spectroscopic Ellipsometry .....	30
CHAPTER 4: Near Field Experimental Methods .....	32
4.1 Pseudoheterodyne Scattering Scanning Near Field Infrared Microscopy .....	32
4.2 Point dipole model .....	45
4.3 Monopole (or Finite Dipole) Model.....	49
CHAPTER 5: Novel aspects of charge and lattice dynamics in $\text{La}_{0.67}\text{Sr}_{0.33}\text{MnO}_3$ on LAO .....	53
5.1 Experimental method.....	54
5.2 Metallic conductivity.....	57
5.3 Infrared active phonons .....	66
5.4 Conclusions.....	71
CHAPTER 6: Dichotomy between bulk and interface properties of $\text{La}_{0.67}\text{Sr}_{0.33}\text{MnO}_3$ thin films .....	73
6.1 Introduction.....	73
6.2 Experimental Methods.....	74
6.3 Results and discussion.....	77

CHAPTER 7: Conclusions and Outlook.....	91
---	----

## Acknowledgements

I would like to thank my advisor, Professor Mumtaz Qazilbash for his patience and hard work in providing me a supportive environment for the excellent scientific research. I appreciate the direct and intuitive way he treats physical problems with emphasis on experimental observation. The most important thing I learned about research is that one should make minimal assumptions and treat problems step by step firmly based on the available data while avoiding unnecessary conclusions. I wish to give thanks to my colleagues and collaborators Tyler Huffman, Zhen Xing, A. J. Hollingshad, N.C. Branagan, D. J. Brooker, N. E. Penthorn, In Hae Kwak, Amlan Biswas, Grace Yong, Vera Smolyaninova, and Raj Kolagani for their support and tolerance during the exciting and time consuming research. Certainly, I also wish to thank all my other friends and professors in the department as well as my parents without whom my current success will not be possible.

To those still struggling on the path of scientific endeavor

# CHAPTER 1

## Introduction

Materials with charge, spin, orbital and lattice degrees of freedom that are coupled to one another are fascinating systems for studying fundamental many-particle physics. These coupled degrees of freedom lead to competing ground states that are close to one another in free energy. Hence, phase transitions are commonly observed in such materials. It follows that the properties of these materials are, in general, highly susceptible to perturbations like chemical doping, temperature, and strain. Hence manipulation of their internal degrees of freedom via external perturbations provides an insight into the interactions that determine their physical properties. Moreover, precise control over large, non-linear changes in the physical properties of these materials can be exploited for applications. The oxides of manganese with the perovskite lattice structure which are commonly called “manganites” are undoubtedly among the most remarkable strongly interacting systems [1]. They have a diverse phase diagram and attract intense interest due to the emergence of metal-insulator transitions, charge ordering, orbital ordering, and magnetic transitions. The mechanisms that lead to phase transitions, phase coexistence, and ordering phenomena in these materials have been the subject of intense investigations [2]. Moreover, some of the manganites exhibit colossal magnetoresistance that has been explored for technological applications in information storage and processing [3].

In this dissertation, films of Sr doped manganite  $\text{LaMnO}_3$  with Sr doping level of 0.33 grown by pulsed laser deposition (PLD) on different substrates have been studied by far field infrared spectroscopy, spectroscopic ellipsometry and scattering type scanning near field infrared microscopy (s-SNIM). Films of  $\text{La}_{0.67}\text{Sr}_{0.33}\text{MnO}_3$  (LSMO) were obtained from collaborators at Towson University and the University of Florida. Infrared microscopy and spectroscopy experiments were performed at William & Mary. Bulk LSMO exhibits a metal-insulator transition coupled to a ferromagnetic-paramagnetic transition at  $T_c \sim 360$  K. The ground state is metallic and ferromagnetic while the high temperature phase is insulating and paramagnetic. This phase transition is second order in zero external magnetic field. It can be qualitatively explained in terms of competition between the double-exchange mechanism and Jahn-Teller distortion of the lattice. The former mechanism favors an itinerant ferromagnetic phase while the latter is thought to induce localization. However, the dynamical properties of free carriers in the metallic phase are not properly understood. This provides us the motivation to study charge dynamics of LSMO with infrared spectroscopy.

The broadband infrared and optical spectrum is important because it covers the optical signatures of metallic conductivity of the medium described by the Drude model [4], infrared-active phonons which are usually described by a Lorentz model [5], as well as charge localization and optical interband transitions which can be fit with a Lorentz or Tauc-Lorentzian model [6]. The advantage of broadband optical spectroscopy is that it provides multi-faceted information about materials [7]. This advantage becomes very helpful especially for the study of

correlated systems with coupled charge, lattice, spin and orbital degrees of freedom and whose properties are sensitive to external stimuli. For example, infrared-active phonons which serve as a fingerprint of structural properties of the material provide important information about the symmetry of the crystal structure and strain within the material. The phonons can be well resolved in the infrared spectrum. Moreover, the infrared spectrum simultaneously captures the charge conductivity of materials which allows us to investigate charge dynamics and electronic bonding. Hence broadband infrared spectroscopy is a good technique to study the metal-insulator phase transition, charge localization and electron-lattice coupling in manganite compounds[8–18].

The availability of high quality, smooth film manganite samples that are grown epitaxially on nearly lattice-matched substrates provides an attractive alternative to polycrystalline and bulk single crystal samples. In recent years, the development of high precision film growth methods allows researchers to accurately control film thickness, morphology, and surface roughness. Manganite thin films allow us to study the effect of the substrate on its physical properties. The presence of the substrate may significantly alter the physical properties of the film near the film-substrate interface due to one or more of the following reasons: strain, symmetry-breaking and charge transfer from the substrate. Moreover, ultra-smooth epitaxial manganite films allow us to probe local variations of the film's properties without possible artifacts arising from rough surfaces.

Phase separation and a variety of magnetic domain patterns have been observed in some manganites with magnetic force microscopy (MFM). These manganites, for example, films of  $\text{La}_{0.33}\text{Pr}_{0.34}\text{Ca}_{0.33}\text{MnO}_3$ ,  $\text{La}_{0.8}\text{Ba}_{0.2}\text{MnO}_3$ ,  $\text{La}_{0.67}\text{Ca}_{0.33}\text{MnO}_3$ , and  $\text{La}_{0.7}\text{Sr}_{0.3}\text{MnO}_3$  grown on different substrates exhibit temperature-dependent coupled metal-insulator and magnetic phase transitions with different critical temperatures [19–26]. Strain effects from lattice mismatch to the substrate are generally understood to lead to different patterns of magnetic domains in the ferromagnetic phase. We note that MFM measurements usually introduce an external magnetic field as a perturbation to the sample due to the magnetization of the tip itself, which can affect the local phases of manganites especially near the critical temperature of the phase transition. The addition of an external magnetic field usually converts a second order phase transition to a first order one near  $T_c$  [27]. Also, with MFM, solely the local magnetization is recorded and it provides no information on the conductivity.

Scanning tunneling microscopy (STM) has been used to probe local phase coexistence between metallic and insulating domains [28,29]. The colossal magnetoresistive behavior of thin film  $\text{La}_{0.73}\text{Ca}_{0.27}\text{MnO}_3$  on strontium titanate (STO) is found to be related to the percolative type phase separation at a fixed temperature near  $T_c$  while varying the external magnetic field [29]. Phase separation is also reported in a thin film  $\text{La}_{0.7}\text{Sr}_{0.3}\text{MnO}_3$  on MgO substrate during the phase transition measured by increasing the temperature across  $T_c$  without an external magnetic field [28]. We note that STM is highly sensitive to surface states because electrons are readily screened inside materials and therefore it

does not provide information about properties below the surface nor about the film-substrate interface.

The spatial resolution of far field optical measurements is constrained by the Abbe diffraction limit [30] and optical properties on the nanometer scale cannot be accessed by conventional optical focusing methods. However, the technique of scattering-type scanning near-field infrared microscopy (s-SNIM) can provide local nanometer scale information about conductivity in materials. Moreover, s-SNIM is sensitive to depths of tens of nanometers and can access the film-substrate interface of thin films. Unlike aperture-type near-field microscope whose imaging wavelength and the optical bandwidth are constrained by the cutoff imposed by the internal diameter of the metallic coated optical fiber [31], the apertureless scattering type near field optical and infrared microscopy can be used with broadband spectroscopic capability from the far infrared to the visible wavelengths. The spatial resolution of this technique is about 20 nm and is solely constrained by the radius of the tip of the atomic force microscope [32]. The s-SNIM method is used in our work to study ultra-thin films of LSMO to search for possible phase coexistence and to study the effect of the substrate on the film properties near the film-substrate interface.

This dissertation is organized as follows. The properties of LSMO and their origin in the physics of Jahn-Teller distortion and double exchange mechanism are described in chapter 2. Far-field infrared methods and near-field infrared methods and models are discussed in chapters 3 and 4 respectively. Novel aspects of charge and lattice dynamics of a bulk-like LSMO film are

presented in chapter 5. Near-field infrared nano-imaging data and analysis of an 18 nm LSMO thin film are presented in chapter 6. Finally, the conclusions of this research and the outlook in this field are outlined in chapter 7.

## CHAPTER 2

### The manganite $\text{La}_{1-x}\text{Sr}_x\text{MnO}_3$

#### 2.1 Phase diagram

The phase diagram of  $\text{La}_{1-x}\text{Sr}_x\text{MnO}_3$  single crystals grown by the floating zone method is shown in Figure 2.1. The chemical doping level of Sr can be tuned to change the type of phase transitions and their transition temperatures. The phase diagram of the Sr-doped manganite  $\text{La}_{1-x}\text{Sr}_x\text{MnO}_3$  is quite complex and diverse exhibiting a variety of structural, electronic and magnetic phases. The parent compound  $\text{LaMnO}_3$  is a highly correlated insulator that exhibits anti-ferromagnetic and orbital ordering. Both the on-site Coulomb repulsion and cooperative Jahn-Teller distortion are thought to contribute to the insulating behavior. The Sr doping introduces charge carriers and suppresses the long-range Jahn-Teller effect. Pulsed neutron diffraction provides evidence for local Jahn-Teller distortion for doping levels between 0.16 and 0.4, even though crystallographic analysis does not reveal a macroscopic, long-range Jahn-Teller effect. Higher hole carrier number, and loss of both long-range cooperative Jahn-Teller distortion and orbital ordering lead to the emergence of a double-exchange driven ferromagnetic metallic phase as the low temperature ground state for Sr doping levels between 0.17 and 0.5 [33,34].

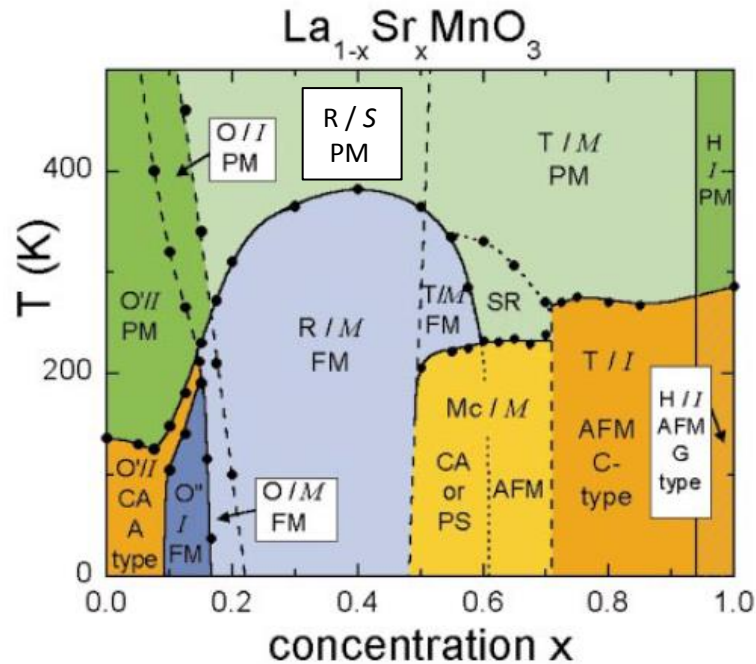


Figure 2.1: Phase diagram of the  $\text{La}_{1-x}\text{Sr}_x\text{MnO}_3$ . O' distorted orthorhombic structure; O orthorhombic; O'' orbital ordered orthorhombic; R rhombohedral; T tetragonal; Mc monoclinic; H hexagonal. PM (green) paramagnetic; SR short range order; CA canted; AFM (yellow) A type antiferromagnetic structure; FM (blue) ferromagnetic; PS phase separated. I (dark) insulating; M (light) metallic. S semiconducting (Ref [33]).

Note that manganite thin films of different thicknesses grown on different substrates can manifest much more complicated phase diagrams. The effects of strain on the magnetic phase diagram due to different substrates and thicknesses of the thin films are extensively studied in reference [35]. The Curie temperature of the ferromagnetic to paramagnetic phase transition of  $\text{La}_{0.7}\text{Sr}_{0.3}\text{MnO}_3$  films on  $\text{LaAlO}_3$  (LAO) is different from the Curie temperature of the LSMO film on  $\text{SrTiO}_3$  (STO). Films grown on LAO substrates exhibit an out-of-plane tensile strain and a corresponding in-plane compression while

films grown on STO exhibit opposite strain states, i.e., out-of-plane compression and in-plane tensile strain. The varying thickness of  $\text{La}_{0.7}\text{Sr}_{0.3}\text{MnO}_3$  thin films can also lead to a dramatic change in the Curie temperature and the type of phase transition [36]. (see Fig. 2.2 ) The temperature dependent metal insulator phase transition disappears in the  $\text{La}_{0.7}\text{Sr}_{0.3}\text{MnO}_3$  thin film grown on  $\text{SrTiO}_3$  (001) substrate by the PLD method when the film thickness becomes less than 8 unit cells.

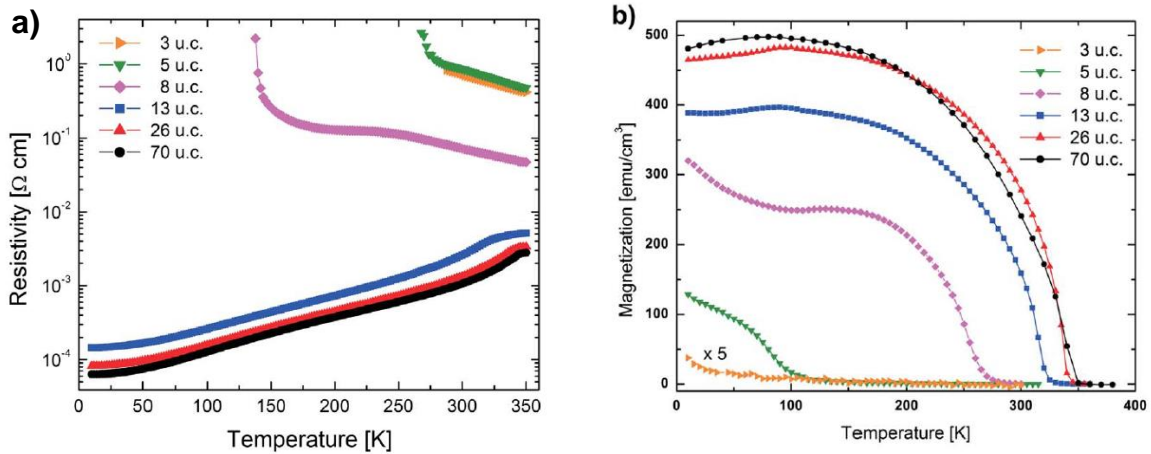


Figure 2.2 a) Temperature dependent resistivity curve of  $\text{La}_{0.7}\text{Sr}_{0.3}\text{MnO}_3$  films of different thicknesses grown on STO (001) substrate. b) Temperature dependence of the magnetization of  $\text{La}_{0.7}\text{Sr}_{0.3}\text{MnO}_3$  films of different thicknesses grown on STO (001) substrate measured at 100 Oe. All samples were field cooled at 1 T from 360 K along the [100] direction before the measurement (Ref [36]).

## 2.2 Lattice structure of $\text{La}_{0.67}\text{Sr}_{0.33}\text{MnO}_3$

The unit cell of the perovskite lattice structure is shown in Figure 2.3. The “A” sites at the corner of the cube are where the La ions are located. The Mn ion in the center is at a “B” site. The Mn ion is surrounded by six oxygen ions in an

octahedral arrangement. The oxygen ions are located at the center of the cube faces.

Due to the different chemical doping, strain and oxygen nonstoichiometry, the crystal lattice of manganites can be slightly distorted (Figure 2.4) and leads to the complex phase diagram.

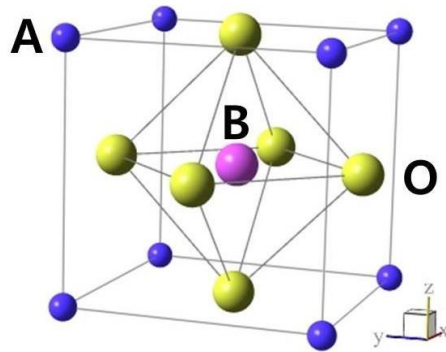


Figure 2.3 The perovskite structure with  $ABO_3$  chemical formula. The La (and Sr) are present on the “A” sites, and Mn is located on the “B” sites. The symbol “O” represents oxygen ions.

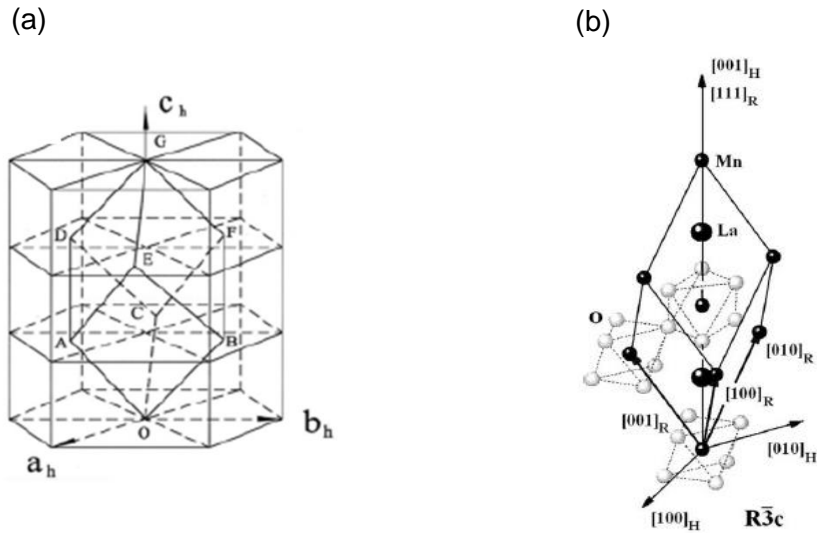


Figure 2.4 a) Schematic illustration showing the hexagonal unit cell of LSMO; [37]; b) Rhombohedral unit cell of lanthanum manganite [38]

### 2.3 Crystal Field Splitting

The  $3d$  orbitals of single Mn atom are 5-fold degenerate. When one considers the six oxygen ions surrounding the manganese, the degeneracy is lifted due to the external Coulomb potential (or “crystal field”) from the octahedral arrangement of the oxygen ions. By symmetry, the  $d_{xy}$ ,  $d_{yz}$ , and  $d_{zx}$  orbitals must all be affected similarly as the three axes ( $x$ ,  $y$ ,  $z$ ) are equivalent in a cubic environment. Hence they should form a triplet of states. The other two  $d$ - orbitals,  $d_{x^2-y^2}$  and  $d_{3z^2-r^2}$  form a doubly degenerate pair. The doublet has a higher energy than the triplet because the “lobes” of the doublet orbitals point towards the negative oxygen ions thereby increasing the energy due to Coulomb repulsion.

For calculating the crystal field splitting between the doublet and triplet one starts by solving the single  $3d$  electron energy eigenvalue problem of the  $\text{Mn}^{6+}$  ion within an isolated oxygen octahedron using degenerate perturbation theory. It is assumed that the local hybridization with the oxygen  $p$ -orbitals is ignored and oxygen ions are treated solely as providing a spatially inhomogeneous electrostatic background. It is further assumed that the electron is located close to the origin.

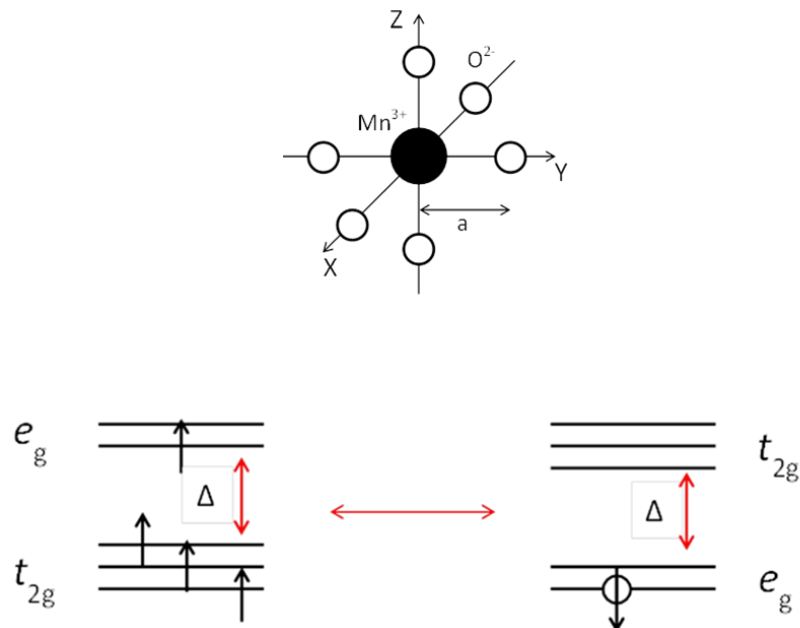


Figure 2.5 The schematic picture of the spatial configuration of a single oxygen octahedron (upper); the electron configuration of  $\text{Mn}^{3+}$  ion and its hole correspondence.

If the oxygen ion has the charge  $Zq$ , (typically  $-2q$  when  $q$  is defined positive), the external electric potential from the oxygen octahedron becomes [1]

$$V(x, y, z) = Zq\left(\frac{6}{a} + \frac{35}{4a^5}(x^4 + y^4 + z^4 - \frac{3}{5}r^4)\right) \quad 2.1$$

$$r^2 = x^2 + y^2 + z^2 \quad 2.2$$

Where  $(x, y, z)$  is the coordinate of a single 3d electron with the origin attached to the Mn ion, and  $a$  is the distance between the Mn ion and the nearest oxygen ion. Then the energy splitting due to the crystal field of the oxygen octahedron can be shown to be  $\Delta = \frac{5Zq}{3a^5}\langle r^4 \rangle \sim 1 \text{ to } 2 \text{ eV}$ , where  $\langle r^4 \rangle = \int_0^\infty dr r^6 R_{32}^2(r)$ , and  $R_{32}^2(r)$  is the radial part of the wavefunction of a single 3d electron for  $n = 3$  and  $l = 2$  [1], [39].

The crystal field energy splitting  $\Delta$  is often referred to as  $10Dq$  in the literature. The four electrons of the  $\text{Mn}^{3+}$  ion (relevant for the manganites) are in a state of maximum spin  $S=2$  due to strong Hund's coupling. This is equivalent to having just one "hole" with opposite spin in a fully spin-polarized shell. Thus the single 3d electron ( $\text{Mn}^{6+}$ ) or single 3d hole ( $\text{Mn}^{3+}$ ) problem have the same crystal field splitting except that in the  $\text{Mn}^{3+}$  case the triplet will be higher in energy compared to the doublet because one considers a single positive charge assuming the fully spin polarized shell is highly symmetric and not as significantly split by the crystal field of the oxygens around it as the single electron state. However, if we return to the actual case of four electrons in the crystal field, the spectra should be inverted again, and the crystal field splitting in the  $\text{Mn}^{3+}$  ion is the same as that in  $\text{Mn}^{6+}$  ion.

The orbitals whose splitting we discussed above are in fact symmetry-related combinations of the manganese  $d$ -orbitals and the oxygen  $p$ -orbitals. The

$d_{x^2-y^2}$  and  $d_{3z^2-r^2}$  orbitals form  $\sigma$ -bonding orbitals that fall into the symmetry class  $e_g$ . The  $d_{xy}$ ,  $d_{yz}$ , and  $d_{zx}$  orbitals for  $\pi$ -bonding fall into the symmetry class  $t_{2g}$  [1]. Of course, more accurate calculations of the crystal field splitting would be required if one were to take into account the hybridization of the  $d$ - and  $p$ - orbitals. However, the results are expected to be similar to those discussed above.

## 2.4 Jahn-Teller Distortion

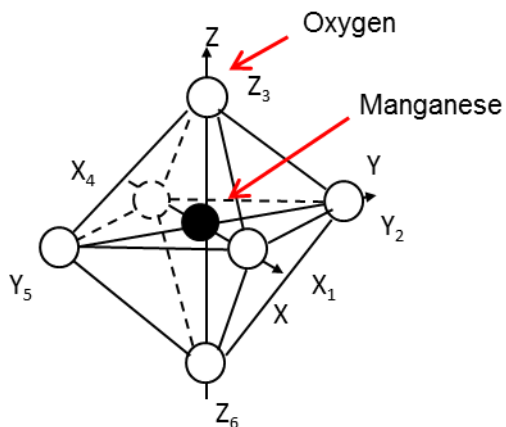


Figure 2.6 The spatial coordinates of a single oxygen octahedron

The crystal field in a lattice with cubic symmetry leads to the splitting between the  $t_{2g}$  triplet and the  $e_g$  doublet. The remaining degeneracy is lifted by the distortion of the oxygen octahedron around the manganese ion also known as the Jahn-Teller distortion. A shift of the oxygen ions leads to asymmetry between different directions and removes the degeneracy. The Jahn-Teller distortion or cooperative effect can be understood as an orbital-lattice interaction.

It is energetically favorable to distort the lattice thereby lifting the degeneracy of the orbitals. The Jahn-Teller distortion is termed “static” when the equilibrium positions of the distorted oxygen ions are frozen in time. Or it can be “dynamic” which means the distorted ion evolves among several different configurations with time although the time-averaged effect will reveal no net distortion.

Assuming that the deviation of a single oxygen ion is small relative to the constant  $a$  defined previously, the change in the potential caused by the ligands with coordinates  $(X,Y,Z,$  see figure 2.6) on the manganese electron with coordinates  $(x, y, z)$  is [1]:

$$\Delta V = -\frac{1}{2}\left(\frac{9}{a^4}\right) [x^2(X_1 - X_4) + y^2(Y_2 - Y_5) + z^2(Z_3 - Z_6)] \quad \mathbf{2.3}$$

The modified potential is first order in the coordinates of the ligands and second order in the electron coordinates. Terms of order  $X_1x$  do not contribute to perturbation theory because their matrix elements vanish [1]. Group theory arguments involving symmetry considerations lead to the result that only two normal modes  $Q_2$  and  $Q_3$  are relevant for lifting the degeneracy of the  $e_g$  sector:

Given that  $X_4 = -X_1$ ,  $Y_5 = -Y_2$ , and  $Z_6 = -Z_3$ , we define  $Q_2 = \frac{1}{\sqrt{2}}(X_1 - Y_2)$  and  $Q_3 = \frac{1}{\sqrt{6}}(2Z_3 - X_1 - Y_2)$ .

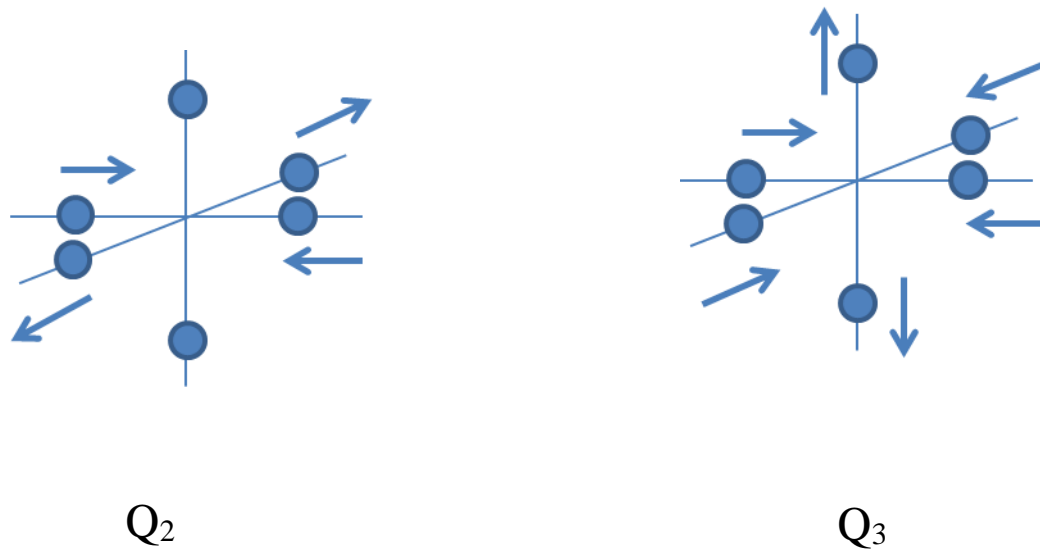


Figure 2.7  $Q_2$  and  $Q_3$  modes of Jahn-Teller phonons

These two normal modes of vibration are shown in Figure 2.7.

As a result, the JT perturbing potential becomes

$$\Delta V|_{JT} = -\sqrt{\frac{2}{3}}\gamma \left[ \sqrt{\frac{3}{2}}(x^2 - y^2)Q_2 + \frac{1}{2}(2z^2 - x^2 - y^2)Q_3 \right] \quad 2.4$$

where  $\gamma = 9/a^4$ . If one considers the transformation,

$$2z^2 - x^2 - y^2 = 4r^2 \sqrt{\frac{\pi}{5}} Y_2^0(\theta, \varphi) \quad 2.5$$

$$x^2 - y^2 = 2r^2 \sqrt{\frac{2\pi}{15}} \left( Y_2^2(\theta, \varphi) + Y_2^{-2}(\theta, \varphi) \right) \quad 2.6$$

and the Hilbert space spanned by the two  $e_g$  orbital basis  $d_{x^2-y^2}$  and  $d_{3z^2-r^2}$  of the 3d electron, the perturbing Hamiltonian will become a 2 by 2 matrix:

$$\Delta V|_{JT} = \frac{2\sqrt{6}}{21}\gamma\langle r^2 \rangle \left[ Q_2 \begin{pmatrix} 0 & 1 \\ 1 & 0 \end{pmatrix} + Q_3 \begin{pmatrix} 1 & 0 \\ 0 & -1 \end{pmatrix} \right] \quad 2.7$$

This gives an energy splitting of  $2gQ$  (1eV scale) [14] between the two eigenstates of this Hamiltonian if we define  $g = -(2\sqrt{6}/21)\gamma\langle r^2 \rangle$ .

There is an energy penalty due to the lattice distortion, and the full perturbative Hamiltonian should be:

$$H = -g(Q_2\sigma_x + Q_3\sigma_z) + \frac{1}{2}M\omega^2(Q_2^2 + Q_3^2) \quad 2.8$$

Then the eigenvalues of  $H$  are:  $E = \mp gQ + \frac{1}{2}M\omega^2Q^2$ . The energy splitting between the two  $e_g$  levels is still  $2gQ$ , if we write:  $Q_3 = Q \cos \theta$ ,  $Q_2 = Q \sin \theta$ .

The model for Jahn-Teller distortion discussed above will need to be modified when the following realistic scenarios are considered: the sharing of oxygen ions by neighboring oxygen octahedra in the lattice, the exchange and hopping process of manganese  $3d$  electrons and  $2p$  oxygen electrons, and the bond angle change of the O-Mn-O chain [40,41]. If so, other normal modes of the oxygen ions distortion will also be involved in the perturbing potential of the Jahn-Teller effect.

## 2.5 Double exchange

After the experimental discovery of the correlation between the electrical conductivity and ferromagnetism in the compounds of manganese with

perovskite structures [42], Clarence Zener proposed the double exchange mechanism to explain this phenomenon [43]. In a nutshell, this mechanism involves indirect coupling between incomplete d-shells via the conducting electrons. According to Hund's rule, the lowest energy configuration for all the unpaired electrons in an atom or ion is to have the electron spins parallel to one another (as in  $Mn^{3+}$ ). The conduction electrons carry their own spins unchanged as they move from site to site, so they will be highly mobile when they move in an environment in which all *d*-electron spins on all the sites are pointing in the same direction. Hence there is a clear connection between ferromagnetism and metallicity in Zener's model.

Since conventional band theory at that time could not explain the semiconducting property of the parent compound  $LaMnO_3$  and the doped compounds with low concentrations of up to 10 percent of Ca, Sr or Ba, Zener used the 3d atomic orbitals of Mn as the starting point to discuss his double exchange idea. For small doping levels ( $x < 0.1$ ), the hole carriers are dilute and conductivity is low. For doping levels  $0.2 < x < 0.4$ , the conductivity increases significantly and ferromagnetism is the strongest. Even though the long range periodic structure of the solid lattice is important to explain the real system, it is useful to understand the physics by following Zener's arguments based on a simple model consisting of solely three atoms (two manganese atoms with an oxygen atom in the center). Zener first considers the toy model of NaCl to introduce the concept of double exchange. Two configurations  $\psi_1 : Na Cl^- Na^+$  and  $\psi_2 : Na^+ Cl^- Na$  are energetically degenerate states.

$$\begin{bmatrix} \langle \psi_1 | H | \psi_1 \rangle & \langle \psi_1 | H | \psi_2 \rangle \\ \langle \psi_2 | H | \psi_1 \rangle & \langle \psi_2 | H | \psi_2 \rangle \end{bmatrix} \begin{bmatrix} c_1 \\ c_2 \end{bmatrix} = E \begin{bmatrix} c_1 \\ c_2 \end{bmatrix} \quad 2.9$$

is the secular equation for the energy eigenvalue problem where  $H$  is the Hamiltonian and  $E$  is the eigenvalue. We can rewrite the secular equation as

$$\begin{bmatrix} \epsilon_0 & \Delta^* \\ \Delta & \epsilon_0 \end{bmatrix} \begin{bmatrix} c_1 \\ c_2 \end{bmatrix} = E \begin{bmatrix} c_1 \\ c_2 \end{bmatrix} \quad 2.10$$

Here degenerate perturbation theory has been applied and to the zeroth order approximation,  $\psi_1$  and  $\psi_2$  are wavefunctions that correspond to the degenerate states with energy  $\epsilon_0$ . The off-diagonal terms are  $\Delta^* \equiv \langle \psi_1 | H | \psi_2 \rangle$  and  $\Delta \equiv \langle \psi_2 | H | \psi_1 \rangle$ . Then, we get the solution for the system energy,  $E = \epsilon_0 \pm |\Delta|$  with  $\psi_+ = \psi_1 + \psi_2$  as the eigenfunction for  $E_+ = \epsilon_0 + |\Delta|$ , and  $\psi_- = \psi_1 - \psi_2$  as the eigenfunction for  $E_- = \epsilon_0 - |\Delta|$ .

When the system is in a superposition state of the symmetric and antisymmetric state, the tunneling of the electron will happen at the frequency =  $\frac{2|\Delta|}{\hbar}$ . Let's assume that initially the system is in the state  $\psi = (\psi_+ + \psi_-)/2$ . After time evolution, the quantum state becomes

$$\psi = e^{-i\frac{E_+}{\hbar}t} \left( \frac{\psi_1 + \psi_2}{2} + \frac{\psi_1 - \psi_2}{2} e^{i\frac{2|\Delta|}{\hbar}t} \right) \quad 2.11$$

and

$$|\psi|^2 = \frac{1}{4} (|\psi_1 + \psi_2|^2 + |\psi_1 - \psi_2|^2) + \frac{1}{2} (|\psi_1|^2 - |\psi_2|^2) \cos\left(\frac{2|\Delta|}{\hbar}t\right) + \frac{i}{2} (\psi_1 \psi_2^* - \psi_1^* \psi_2) \sin\left(\frac{2|\Delta|}{\hbar}t\right) \quad 2.12$$

For an effective description, consider a single conducting electron on the ion chain  $Na^+Cl^-Na^+$  as the static background. The configuration states  $\psi_1$  and  $\psi_2$  can also be replaced by the single electron quantum wave functions at the atomic sites on the  $Na^+$  ion at the two ends of the ion chain. Due to the limited overlap of the wavefunctions  $\psi_1$  and  $\psi_2$ , the main contribution to the temporal part of the charge density distribution comes from the second cosine term of the formula above which corresponds to the charge density oscillation between the two  $Na^+$  ions at the frequency  $\omega = \frac{2|\Delta|}{\hbar}$ .

A more detailed theoretical investigation of the double exchange effect in the manganites was carried out by P. W. Anderson and H. Hasegawa [44]. In figure 2.8 the basic unit of the chain formed by two Mn ions and the intermediary O ion is plotted. The relevant configurations are labelled in the table 2.1.

A. Orbitals	$Mn_1$	O	$Mn_2$
Mobile $d$ electron	$d_1$		$d_2$
O $2p$ shell electron		$p$	
Fixed $d$ electrons	$d'_1$		$d'_2$
B. Configurations			
I	$d'_1 d_1$	$p^2$	$d'_2$
II	$d'_1$	$p^2$	$d'_2 d_2$
III	$d'_1 d_1$	$p$	$d'_2 d_2$

Table 2-1. Labeling of wavefunctions in double exchange.

Configurations I and II are energetically degenerate while the configuration III is an energetically excited state. Considering that the perturbation induced by

the processes involving the transitions between configurations I and III as well as configurations II and III are higher order in perturbation theory, we focus here on processes involving configurations I and II.

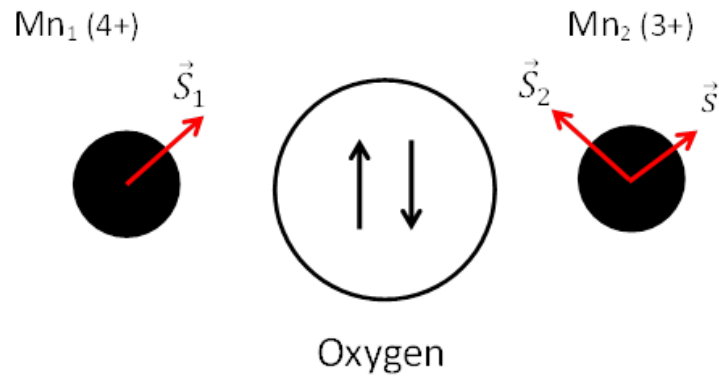


Figure 2.8 a pair of manganese ions with different electron occupations and the intermediary oxygen.  $\vec{S}_1$  and  $\vec{S}_2$  are core spins of the  $Mn_1$  and  $Mn_2$  ions respectively, and  $\vec{S}$  is the spin of the itinerant electron.

One starts by using a semi-classical approach which treats the core spin from the three  $t_{2g}$  electrons ( $d'_1$  and  $d'_2$ ) whose spins are lined up in the  $3d$  orbitals of the Mn ions as a classical vector with a fixed spatial orientation.

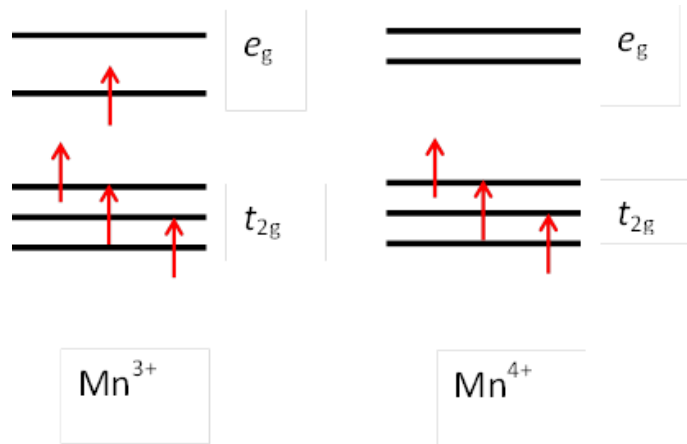


Figure 2. 9 the electron configuration of  $Mn^{3+}$  and  $Mn^{4+}$  ions

Assuming that the classical core spins  $\vec{S}_1$  and  $\vec{S}_2$  span the angle  $\theta$  as shown in figure 2.10,

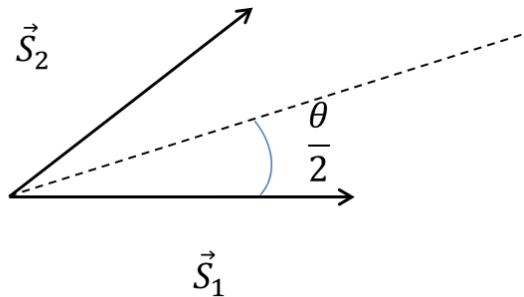


Figure 2. 10 the classical core spins  $\vec{S}_1$  and  $\vec{S}_2$  span the angle  $\theta$

For the configuration I and II, the onsite intra-atomic coupling of the  $d_1$  and  $d_2$  electrons (the  $e_g$  electron in the  $3d$  orbital of the Mn ion) to the  $d'_1$  and  $d'_2$  respectively can be described by  $E(d'_{1\uparrow}d_{1\uparrow}) = -JS$ , where  $S$  is  $3/2$  for the core spins and  $J$  is the intra-atomic exchange integral between the itinerant electron and the core electrons. Here, the spin of the  $e_g$  electron lines up with the core

spin provided by the  $t_{2g}$  electrons. If the spin of the  $e_g$  electron is anti-parallel to the core spin, then the energy is given by  $E(d'_{1\uparrow}d_{1\downarrow}) = J(S + 1)$ .

The two  $p$  orbital electrons ( $p^2$ ) of the oxygen atom form a singlet state with a total spin of zero. The numbering of wavefunctions is shown in table 2-2 below for the three configurations shown in table 2-1

	$d_1$	$p$	$p$	$d_2$
Configuration I	1	2	3	
Configuration II		1	3	2
Configuration III	1	3		2

Table 2-2. Numbering of wavefunctions used for the three configurations in Table 2-1.

Note that 1, 2, 3 are the labels of the 3 electrons and solely the hopping between the nearest neighbor atoms is considered. If you project their spins onto the spatial direction fixed by the classical core spins of one of the two  $Mn$  atoms of the three atom chain, for example  $\vec{S}_1$ , the spin part of the wavefunction of configuration I and II can be written as

$$\alpha(1)(\alpha(2)\beta(3) - \alpha(3)\beta(2)) \leftrightarrow (\alpha(1)\beta(3) - \alpha(3)\beta(1))\alpha(2)$$

and

$$\beta(1)(\alpha(2)\beta(3) - \alpha(3)\beta(2)) \leftrightarrow (\alpha(1)\beta(3) - \alpha(3)\beta(1))\beta(2)$$

during the transition from the configuration I to the configuration II and vice versa since the total spin state of the chain formed by the three atoms is assumed unchanged. The spin of the  $d_1$  electron has the probability amplitude of  $\alpha(1)$  on

the basis state with the spin pointing along  $\vec{S}_1$ , and the probability amplitude of  $\beta(1)$  on the basis state with the spin pointing against  $\vec{S}_1$ . Then we can write:

$$|d_1\rangle = |\varphi(r_1)\rangle \otimes \begin{pmatrix} \alpha(1) \\ \beta(1) \end{pmatrix} \quad \mathbf{2.13}$$

The spin states of electrons labelled by 2 and 3 are also written with the same basis set of the Hilbert space.

After being projected to the new basis determined by the direction of the classical spin  $\vec{S}_2$  which makes the angle  $\theta$  relative to  $\vec{S}_1$ , the probability amplitudes of the same spin quantum state become  $\alpha'(1)$  and  $\beta'(1)$  which are related to  $\alpha$  and  $\beta$  by

$$\begin{pmatrix} \alpha(1) \\ \beta(1) \end{pmatrix} = \begin{pmatrix} \cos\frac{\theta}{2}\alpha'(1) + \sin\frac{\theta}{2}\beta'(1) \\ -\sin\frac{\theta}{2}\alpha'(1) + \cos\frac{\theta}{2}\beta'(1) \end{pmatrix} \quad \mathbf{2.14}$$

Considering that onsite spin flipping is forbidden, it follows that

$$\langle d_1\alpha | H | d_1\beta \rangle = 0 \quad \mathbf{2.15}$$

$$\langle d_2\alpha | H | d_2\beta \rangle = 0 \quad \mathbf{2.16}$$

For the transition between the configurations I and II, the exchange integral may be written in the form

$$\int \varphi(1)\chi(2)H\varphi(2)\psi(1) d\tau$$

$\varphi(i)$  corresponds to the wave function of the  $p$  state, while  $\chi(i)$  and  $\psi(i)$  correspond to the wave functions of  $d_2(2)$  and the  $d_1(1)$  with the label  $i$  of the electrons shown in Table II.

As a result, the transfer matrix element between configuration I and II is

$$\langle d_1\alpha | H | d_2\alpha \rangle = b \quad 2.17$$

if  $\theta = 0$ .

Then the Hamiltonian can be written as

$$H = \begin{matrix} & d_1\alpha & d_1\beta & d_2\alpha' & d_2\beta' \\ \begin{matrix} d_1\alpha \\ d_1\beta \\ d_2\alpha' \\ d_2\beta' \end{matrix} & \begin{pmatrix} -JS & 0 & b \cos \theta/2 & b \sin \theta/2 \\ 0 & J(S+1) & -b \sin \theta/2 & b \cos \theta/2 \\ b \cos \theta/2 & -b \sin \theta/2 & -JS & 0 \\ b \sin \theta/2 & b \cos \theta/2 & 0 & J(S+1) \end{pmatrix} & \end{matrix} \quad 2.18$$

The solution of the energy eigenvalue problem then becomes

$$E = \frac{1}{2}J \pm \left\{ \left[ J \left( S + \frac{1}{2} \right) \pm b \cos(\theta/2) \right]^2 + b^2 \sin^2(\theta/2) \right\}^{\frac{1}{2}} \quad 2.19$$

Since  $J$  (at the scale of 1eV) [14] is much larger than  $b$  (at the scale of 10meV) [45], the solution becomes:

$$E = \begin{cases} J(S+1) \pm b \cos(\theta/2) \\ -JS \pm b \cos(\theta/2) \end{cases} \quad 2.20$$

The ground state is  $E = -JS - b$  when  $\theta = 0$  which is a ferromagnetic metallic state. But when  $\theta = \pi$ ,  $E = -JS$ . This excited state is not far away from the ferromagnetic metallic state, but is an antiferromagnetic metallic state with a

nonzero exchange integral. The energy scale of  $b$  can be estimated from the spin wave excitation energy. This may explain the low temperature monoclinic AFM metallic ground state near the Sr doping level of 0.6 in the phase diagram in Figure 2.1. The doping level and strain can lead to the variation of the bond angle and bond length, and thereby change the ground state energy.

Anderson's result can be expanded to the whole lattice with long range periodicity either by considering the method of Linear Combination of Atomic Orbitals (LCAO) type method (hybridizing the relevant Mn and O atomic orbitals and apply them as the new basis when dealing with the lattice problem in perturbation theory) [46] or applying it directly in real space with empirical parameters and nearest neighbor hopping [47]. The simple model misses other details such as the correct lattice symmetry due to the actual lattice distortion from the cubic lattice [33,40] and physical processes such as the Jahn-Teller effect [11]. However, it still can provide the correct ground state at low temperature for certain types of lattice structures and chemical doping. Moreover, the local configuration-type consideration discussed here without detailed band structure also provides an acceptable prediction to the relevant central peak values of the Lorentzian type photoemission bands directly corresponding to the energy density of states [48].

## CHAPTER 3

### Far Field Experimental Methods

#### 3.1 Fourier Transform Infrared (FTIR) spectroscopy

Fourier Transform Infrared (FTIR) Spectroscopy is based on a Michelson-type interferometric measurement. Both symmetric and asymmetric-type measurement can be done depending on whether the sample is placed within the combined beams [49] or in one arm of the interferometer [50]. Our setup (Bruker Vertex 80v) enables us to obtain the spectrum range covering 2 meV to 2.5 eV in a symmetric FTIR configuration. Information about the electronic structure and dynamics, phonons, and magnetic resonances can be obtained through reflectance and/or transmission measurements and subsequent analysis that yields the optical conductivity of the relevant sample.

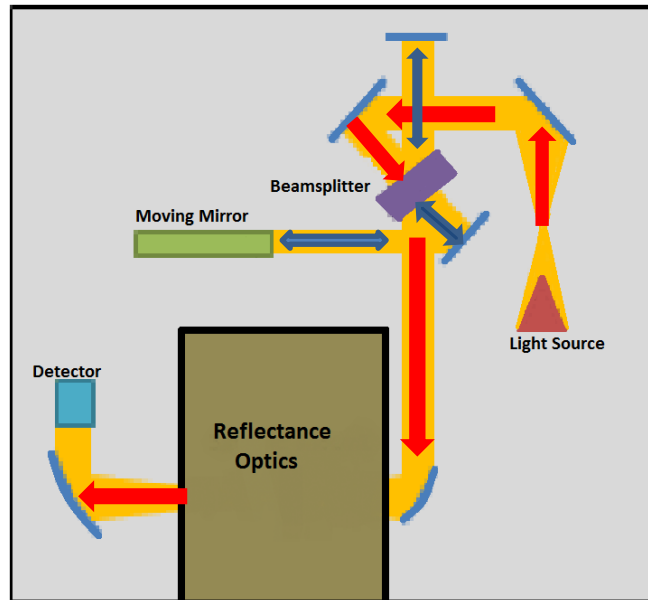
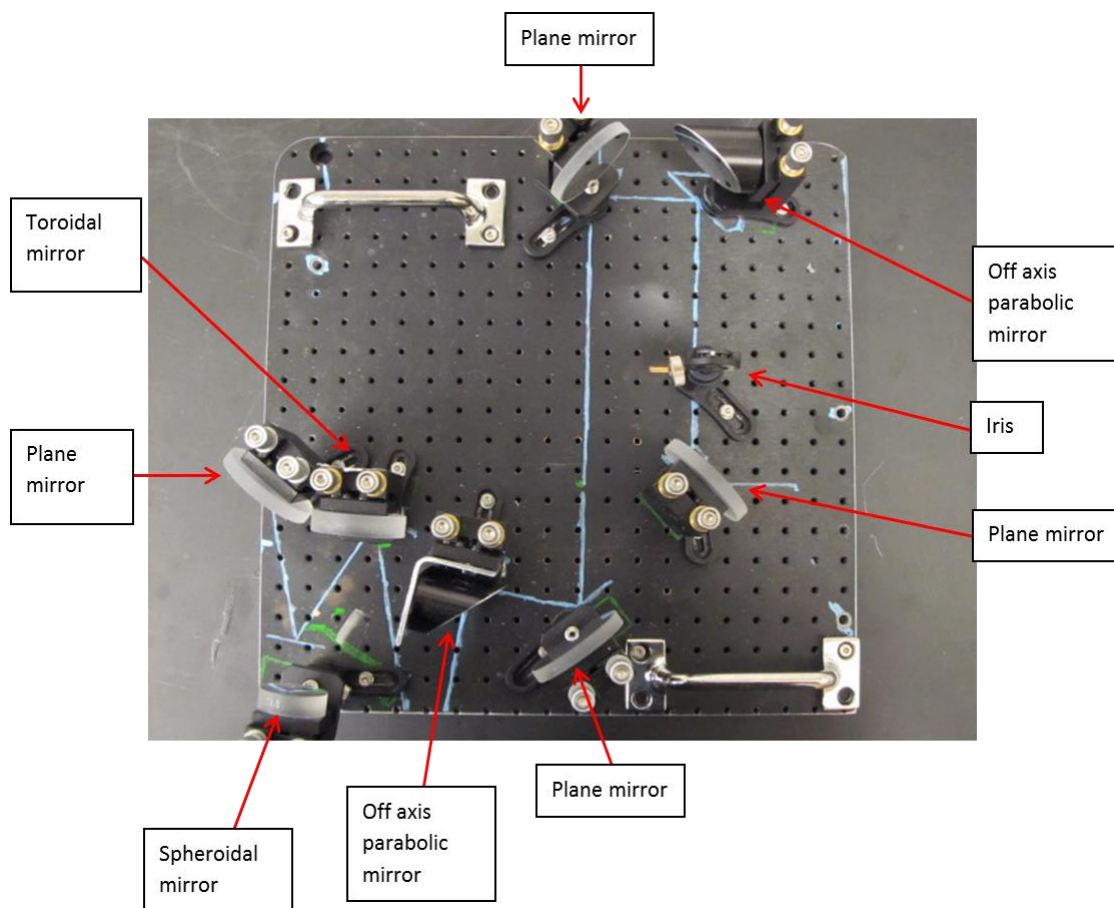


Figure 3.1 The beam path of an FTIR Spectrometer [51]. The reflectance optics are described in figure 3.2.

Software such as WVASE32 [52] is used to fit broadband reflectance and/or transmission data with Kramers-Kronig consistent oscillators in order to determine the dielectric function. If the sample is a thin film on a substrate, then data is obtained on both the sample and a bare substrate. The dielectric function of the substrate is obtained first and this is used in the model for extracting the dielectric function of the thin film. In general, reflectance and/or transmission data is modeled together with ellipsometry data obtained at higher photon energies. This enables more accurate determination of the broadband dielectric function.



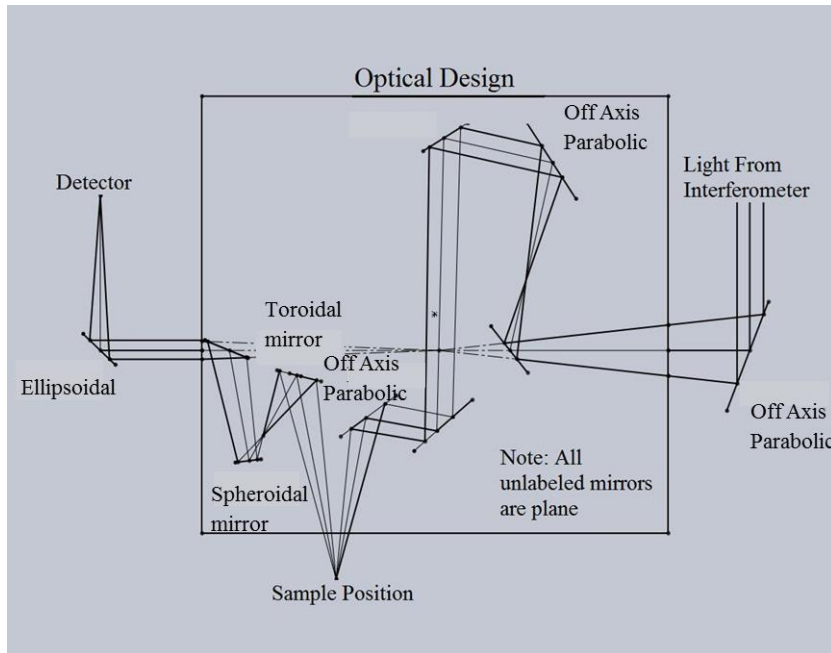


Figure 3.2 The two panels show a picture of the optics of the reflection unit and its schematic optical design

The Bruker Vertex 80v spectrometer is configured for transmission measurements on transparent samples. However, many samples are opaque in part or all of the spectral range and can only be measured in the reflectance geometry. Hence it was necessary to design and construct optical and mechanical additions to the spectrometer to allow reflectance measurements.

Fig 3.2 shows the reflectance unit which is removable and convenient to set up. I worked on the optical design of this reflectance unit. The optical components and the beam path are chosen keeping in view the constraints on the parameters of the beam going into and exiting the sample chamber of the spectrometer. Considering the conservation of etendue, the pair of off-axis parabolic mirrors is chosen to minimize the spot size on the sample by using a

mirror with a relatively shorter effective focus length immediately before the sample. In practice the spot size is ~2mm on the sample surface. The toroidal collection mirror is a good approximation of a concave ellipsoidal mirror with two focal points: one on the sample surface and the other in front of the convex spheroidal mirror (an approximation of a convex hyperboloid mirror). The incident angle of the infrared beam on the sample is approximately 10 degrees. The reflectance setup also includes the homebuilt cryogenic unit with an ultrahigh vacuum chamber which can be regularly pumped down to about  $10^{-8}$  mbar at room temperature. This enables temperature dependent measurements from 5 K to 400 K with a cryostat from ARS Inc.

### 3.2 Variable Angle Spectroscopic Ellipsometry

Spectroscopic ellipsometry measures the quantities  $\Psi(\omega)$  and  $\Delta(\omega)$  defined below:

$$\rho(\omega) = \frac{\tilde{r}_p(\omega)}{\tilde{r}_s(\omega)} = \tan(\Psi(\omega))e^{i\Delta(\omega)} \quad \mathbf{3.1}$$

Here  $\rho(\omega)$  is the ratio of  $\tilde{r}_p(\omega)$  and  $\tilde{r}_s(\omega)$ , the respective complex Fresnel coefficients for p-polarized light (polarized in the plane of incidence) and s-polarized light (polarized perpendicular to the plane of incidence) as a function of (angular) frequency  $\omega$ . The usual reflectance measurement like the symmetric FTIR is an intensity measurement obtained relative to the reflectance of a known material like gold and can usually achieve 0.1% accuracy. However, measurement of the ellipsometric coefficients  $\Psi$  and  $\Delta$  with spectroscopic

ellipsometry can achieve better accuracy. This is because compared with the usual reflectance intensity measurement, ellipsometry is a “self-referenced” measurement as it measures the ratio of p-polarized light to s-polarized light. For a bulk sample like a single crystal, spectroscopic ellipsometry can, in general, provide the dielectric function directly from the ellipsometric coefficients without the necessity of measuring another known sample as a reference. For more complex multilayer films on a substrate, additional data is required including measurements on a bare substrate as well as multi-angle measurements. Our variable angle spectroscopic ellipsometry (VASE) setup from J. A. Woollam Co. Inc covers the spectrum range of 0.6 eV ( $\sim 4800 \text{ cm}^{-1}$ ) to 6 eV ( $\sim 48,000 \text{ cm}^{-1}$ ). Temperature dependent measurements can be done from 5 K to 400 K with a homebuilt ultra-high vacuum cryogenic unit.

## CHAPTER 4

### Near-Field Experimental Method and Models

#### 4.1 Pseudoheterodyne Scattering Scanning Near Field Infrared Microscopy

In this chapter, we discuss the physical basis, experimental method, and analytical models for scattering-type scanning near-field optical microscopy. This experimental technique relies on light scattering from the tip of an atomic force microscope (AFM). The tip is generally in close proximity to the sample and the AFM is used in the tapping mode. While this experimental method can be used for visible and near-infrared frequencies, it has found its principal applications in the mid- and far-infrared frequency range.

Far field optical measurements are constrained by Abbe's diffraction limit and the spatial resolution is limited to the optical wavelength scale. Near-field detection involving evanescent wave coupling can circumvent this limitation by introducing a much broader lateral spatial frequency bandwidth due to the rapid exponential decay of optical amplitude in the  $z$  direction i.e. the direction perpendicular to the lateral surface. If the discussion is confined to the elastic scattering regime, the total photon momentum magnitude  $k$  and photon energy  $\hbar\omega$  are conserved in the process. A field expansion in the inhomogeneous plane wave basis can be performed on the electromagnetic field between the near field scatterer and the medium below it with the constraint

$$k^2 = k_{//}^2 - k_z^2$$

4. 1

Such that  $k^2$  is kept constant,  $k_{//}^2$  is the square of the magnitude of the in plane component of the wave-vector, while  $k_z^2$  is the square of the magnitude of the z component of the wave-vector.  $k_{//}$  and  $k_z$  are real numbers which can be either positive or negative. Note that the wavevector  $\vec{k} = k_{//}\hat{r} + ik_z\hat{z}$  is imaginary in the z-direction. To guarantee the exponential decay instead of growth of the magnitude of the electromagnetic wave amplitude away from the scatterer,  $k_z$  has the same sign as that of the z coordinate. As a result, only evanescent wave components which contribute most to the near field interaction are contained here. The spatial coordinates are shown in figure 4.1 below.

For the near field part of the electromagnetic (EM) modes between the scatterer and the sample surface, the basis of the typical wave components then becomes  $e^{i((k_{//}r+ik_zz)-\omega t)}$ . In this case, the origin of the coordinates is set at the center of the scatterer which is assumed small enough compared to the spatial wavelength of the incident electromagnetic wave.

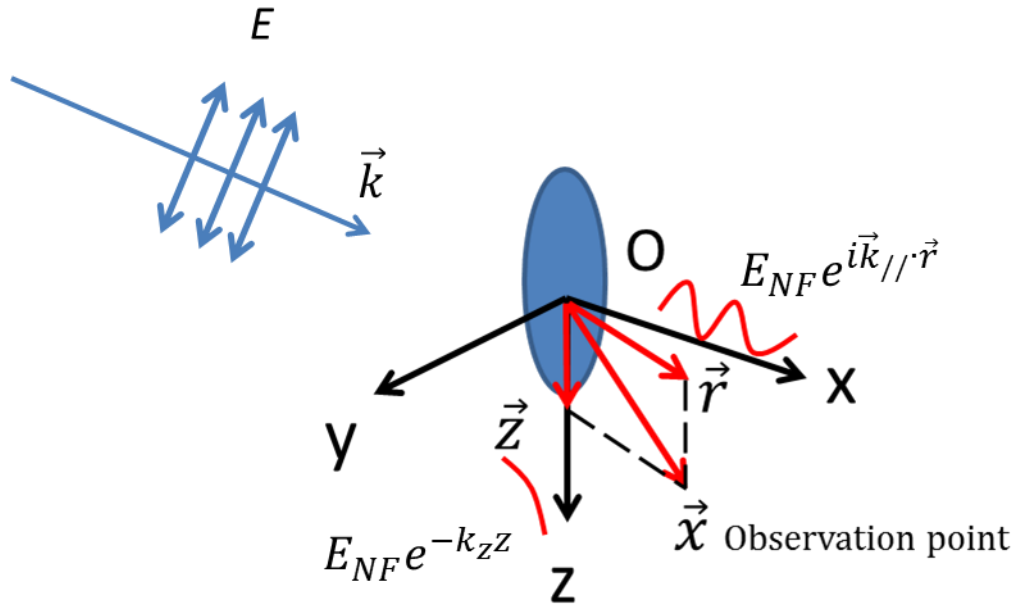


Figure 4.1 Schematic picture of the near-field scattering showing an ellipsoid scatterer, the incident EM wave, and the near-field components.

The wavevector  $\vec{k}$  can point in an arbitrary spatial direction, in principle. Multiple scattering between the scatterer and the sample surface should be included and a self-consistent definition of spatial coordinates should be introduced to include all electromagnetic sources. If the distance between the scatterer and the sample surface is small (usually at nanometer scale), the evanescent modes with more dramatic decay rate in the  $z$  direction (spatial components with larger  $k_z$ ) will be able to couple efficiently between the scatterer and sample surface while other components with slower decay rate in the  $z$  direction (spatial components with smaller  $k_z$ ) may also couple simultaneously. There is enough  $k_z$  bandwidth coupling the combined system of the near field scatterer and the local sample region nearby through the EM gap modes. Since

the distance between the tip apex and the sample surface is usually kept at tens of nanometers due to application of the tapping mode AFM, and the AFM tip has a finite radius of curvature (specifically, a point dipole corresponding to a polarized sphere with its radius equal to the local tip radius of curvature can be assigned near the tip apex), the highest sensible  $k_z$  component should be at the scale of  $\frac{1}{a}$  if the decay rate of  $e^{-k_z z}$  is considered. Because " $a$ " ( $\sim 20\text{nm}$ ) is the tip radius around the apex of the AFM, this serves as the nearest interaction distance between the point dipole and the sample below. Larger  $k_z$  components from the point dipole thus cannot reach the sample surface due to the very fast spatial decay. As a result, we can obtain an estimate of the EM bandwidth of the  $k_z$  for the near field interaction between the point dipole and the sample surface as  $\leq \frac{1}{a}$ . (Actually, for an arbitrary point dipole with a certain temporal oscillation frequency, the inhomogeneous wave component can have arbitrary large  $k_z$  according to the Weyl identity, but if they are not detected by the sample, they do not improve the near field detection spatial resolution). The magnitude of  $\vec{k}$  which is the wave vector of the light propagation in free space is much smaller compared with  $|k_z|$  for most of the evanescent modes coupling the point dipole and the sample surface below it. Thus the bandwidth of  $k_{//}$  is determined by the bandwidth of  $k_z$  and is also about  $\frac{1}{a}$  due to equation 4.1. The lateral spatial resolution of the near-field imaging  $\Delta r$  thus is kept at the scale of " $a$ " which is about 20 nm due to the uncertainty principle.

$$\Delta r \cdot \Delta k_{//} \sim 1$$

**4. 2**

However, the realization of this spatial resolution also relies on filtering of the wave modes of the coupling field between the near field scatterer and the local sample region with smaller  $k_z$  (with a slower decaying rate when propagating in the z direction) since these modes involve EM scattering from larger spatial regions and may degrade the physical spatial resolution of the instrument. This filtering can be achieved by the detection of higher order harmonic demodulation of the near field scattering signals with a tapping tip. This is because the scattered optical signal detected in the far-field is proportional to the changing polarization (the optical susceptibility) of the combined system formed by the near field scatterer and the local sample region which is strongly modulated by the strength of the mutually coupled EM field between them that now varies in time with changing tip-sample distance. Only the gap EM modes between the tip and sample with the larger spatial decay rate when propagating in z direction are selected if solely the far-field optical scattering signals with a steeper temporal variation are detected. This pushes the center spatial frequency of the gap EM modes detected to a higher value with a certain compromise of its spatial frequency bandwidth. Thus the local nanoscale dielectric response of the sample which is embedded in the small change of the polarization of the combined system of the tip and sample below it induced by the near field coupling is deduced from its far field scattering signals. Introducing a mechanical slow temporal modulation of the near field coupling at the lock in detection frequency makes it possible to separate the far field optical scattering due to the relevant polarization variation induced by the high spatial frequency band of the

evanescent gap EM modes from the overwhelming far field induced polarization of the combined tip sample system within the focus region of the incident light (see figure 4.2).

To further improve the lateral spatial resolution (as well as achieving smaller detection depth in z direction), a better  $k_z$  band filter will be required. A compromise must be made if the problem is confined within the classical wave optics domain. Similar spatial frequency (or wavevector) band filtering by the mechanical modulation of the probe sample distance is also required in the aperture-type near-field microscope for a certain tip-sample equilibrium distance. A more confined spatial region measurement can be achieved since only scattered signals due to the polarization from the near field evanescent modes selected by the lock-in detection are involved here instead of the scattered signals which can come from a more extended spatial region polarized by the near-field coupling [53]. Such schemes are experimentally challenging to implement for long wavelength infrared light. If the quantum nature of light is considered and the fluorescence type measurement is made, then the  $k$  bandwidth can be increased effectively and the relevant spatial resolution can also be increased [54]. In general, fluorescence measurements work with visible light for biological systems.

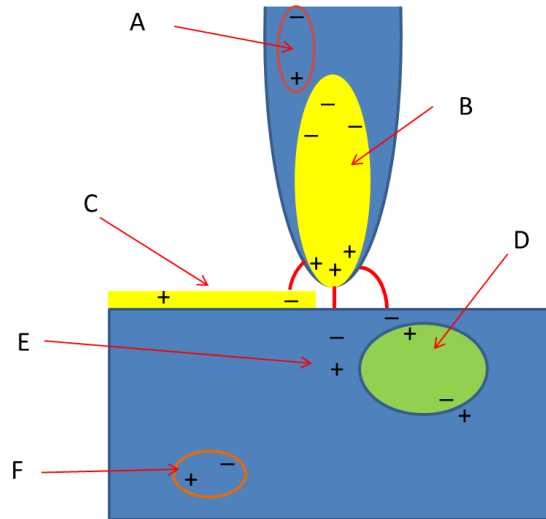


Figure4.2. Polarization induced by the tip-sample interaction in an external electromagnetic field. A: the polarization induced by the electromagnetic field, but not significantly modulated by the mechanical tapping of the AFM tip; B. the polarization significantly modulated by the mechanical tapping of the AFM tip through the gap evanescent wave modes. C, D, E the polarization significantly modulated by the tapping AFM tip through the gap modes. F the polarization not significantly modulated by the tapping AFM tip.

Historically, scattering-type near-field infrared microscopy employed homodyne amplification relying on a single beam interferometric measurement [55]. This measurement relied on amplification with background scattering from the shaft and cantilever of the AFM tip system. While the infrared signal at higher harmonics of the tip oscillation frequency  $\Omega$  contains near-field contribution, quantitative modeling and analysis of the data is difficult because of mixing of the near-field and background scattering. Even when homodyne amplification with a

reference beam in a controlled interferometric measurement is employed, this method is not ideal for measurements of weak dielectric contrast because the data analysis is complicated due to the multiplication of the amplitude and phase signals in the final result (the multiplicative background) [56]. Hence, the local complex dielectric function cannot be readily obtained with the homodyne method, and the material identification capability of this method is very limited. This is also because optical phase is sensitive to environmental perturbation and thus hard to measure accurately, and if the multiplicative background is included, the data becomes vulnerable to error.

This point can be presented as follows: experimentally the lock in detection of the zeroth order harmonic demodulation provides much larger detected electric field intensity (amplitude) than the first order one and the same relation between the first order detection and second order one. The far field scattered optical signal  $E_{SC}$  can always be written as

$$\mathbf{E}_{SC} = \mathbf{E}_{NF} + \mathbf{E}_{BG} \quad \mathbf{4.3}$$

$E_{NF}$  is the far field detected optical scattering signal coming from the spatially confined polarized region which is a result of the near field interaction between the tip and the sample.  $E_{BG}$  is the background signal contained in the total far field detected optical scattering other than the portion treated as the contribution from the near field polarized part mentioned above.

The Fourier series expansion can be made as follows:

$$\mathbf{E}_{SC} = \sum_{n=-\infty}^{\infty} \mathbf{s}_n e^{i\varphi_n} e^{-in\Omega t} = \sum_{n=-\infty}^{\infty} \mathbf{E}_{SC,n} e^{-in\Omega t} \quad \mathbf{4.4}$$

Similarly

$$E_{NF} = \sum_{n=-\infty}^{\infty} s_{n,NF} e^{i\varphi_{n,NF}} e^{-in\Omega t} \quad 4.5$$

$$E_{BG} = \sum_{n=-\infty}^{\infty} s_{n,BG} e^{i\varphi_{n,BG}} e^{-in\Omega t} \quad 4.6$$

For a single beam interferometric measurement, the  $n$ th harmonic demodulation then becomes:

$$I_n \propto E_{SC,0} E_{SC,n}^* e^{in\Omega t} + E_{SC,n} E_{SC,0}^* e^{-in\Omega t} \quad 4.7$$

as an approximation of the accurate  $n$ th harmonic demodulation term ignoring the sum frequency and different frequency generation terms not containing  $E_{SC,0}$  if the zeroth order demodulation term is very large compared to other terms. This can also turn out to be a bad approximation if the relative phase of the  $E_{SC,0}$  and  $E_{SC,n}$  is such that it makes the term  $I_n$  above very small and more terms of the sum frequency and difference frequency need to be kept to obtain the correct value of  $I_n$ . This defect can be corrected if the interferometric amplification term of  $E_{SC,0}$  is replaced by a well controlled reference beam using Michelson-type interferometry, and the relative phase can be tuned to verify the repeatability and stability of the data collected in the relative measurements. However, as mentioned above, even this controlled homodyne method can be unreliable because the reference beam interferes with the near-field component in the same way as the background.

Hence, the  $n$ th harmonic demodulation term can be written as:

$$I_n \approx s_{0,BG} s_{n,NF} \cos(\varphi_{0,BG} - \varphi_{n,NF} + n\Omega t) + \rho s_{n,NF} \cos(\psi_R - \varphi_{n,NF} + n\Omega t) \quad 4.8$$

where the reference wave has the form  $E_R = \rho e^{i\psi_R}$ . The accuracy of the

homodyne method depends on the relative amplitude of the reference beam and the background scattering as well as the relation between the phases  $\varphi_{0,BG}$  and  $\psi_R$ . More advanced methods are required to disentangle the near-field amplitude and phase information, for example, heterodyne detection [57] and pseudo heterodyne detection[56].

We have used the pseudo-heterodyne technique for the near-field infrared work presented in this dissertation, and this method is explained below:

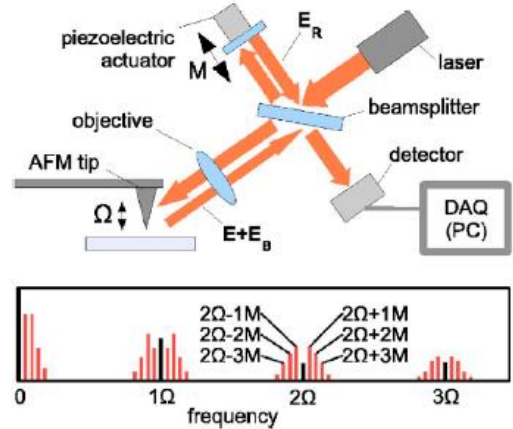


Figure 4.3. Schematic picture of pseudo-heterodyne near field detection [56]

The pseudo-heterodyne method relies on a Michelson interferometer as shown in Fig 4.3. The optical beam is incident on a beam splitter (zinc selenide in our application). Part of the beam that goes through the beam splitter is focused with an achromatic parabolic mirror (the objective) onto the tip, and is scattered by the tip apex which is mechanically tapping at the frequency  $\Omega$ . The backscattered beam from the tip-sample system is collected by the same objective and

reflected by the beam splitter towards the detector. If only this beam is incident on the detector and the reference beam is blocked, then solely the harmonics of the tip frequency  $n\Omega$  will be detected (the black colored peaks in Fig.4.3). This is equivalent to the homodyne detection scheme. However, if the reference beam which is reflected by the beam splitter and the piezoelectric driven reference mirror vibrating at the frequency  $M$  is combined at the beam splitter with the tip scattered beam, then side band structures at different harmonics will appear in the detector signal. The side bands near the second and higher harmonics of the tip oscillation frequency are used to generate the measured amplitude and phase signals.

If the electric phasor of the reference beam  $E_R$  is written as

$$\mathbf{E}_R = \rho \mathbf{e}^{(i\gamma \sin(Mt) + i\psi_R)} \quad \mathbf{4.9}$$

$\rho$  is the optical amplitude as a real number,  $\gamma$  is the modulation depth fulfilling the relation:

$\gamma = \frac{4\pi\Delta l}{\lambda}$  where  $\Delta l$  is the amplitude of the mechanical oscillation of the reference mirror ( $2\Delta l$  is the peak to peak value),  $\lambda$  is the optical wavelength, and  $\psi_R$  is the phase offset which can be tuned by shifting the central position of the vibrating reference mirror. The phase offset affects the relative optical phase difference between the signal beam and the reference beam.

As a result the optical intensity  $u_{n,m}$  measured by the lock in detection at the side band frequency  $(n\Omega + mM)$  can be written as:

$$\mathbf{u}_{n,m} \propto \rho J_m(\gamma) s_n \cos(\varphi_n - \psi_R - \frac{m\pi}{2}) \quad 4.10$$

$J_m(\gamma)$  is the Bessel function of the first kind,  $m$ th order.

If two signal amplitude  $u_{n,j}$  and  $u_{n,l}$  are measured simultaneously, enough information is then collected to reconstruct the near-field amplitude and phase. If  $j$  and  $l$  are an even and odd number respectively, we have:

$$K s_n e^{i(\varphi_n - \psi_R)} = \mathbf{u}_{n,j}/J_j(\gamma) + i \mathbf{u}_{n,l}/J_l(\gamma) \quad 4.11$$

Where  $K$  is a real number and serves as a proportionality factor related to the optics, source intensity profile and the detector sensitivity.  $\psi_R$  is the relative phase difference of the signal and reference beam which is not significantly affected by the source's temporal phase fluctuation if the beam path difference for the two interferometer arms is small.

A relative measurement between the sample and a reference (for example, a gold film or silicon) is needed to cancel out the factor  $K$  and phase difference  $\psi_R$  and obtain the relative quantities  $\frac{s_{n,s}}{s_{n,r}}$  and  $(\varphi_{n,s} - \varphi_{n,r})$  where  $s_{n,s}$  and  $s_{n,r}$  are the near field scattering amplitude measured on the sample and the reference respectively, and  $\varphi_{n,s}$  and  $\varphi_{n,r}$  are the near field scattering phase measured on the sample and the reference respectively. Hence, successive measurements of the sample and reference provide values of the relative amplitude and phase shift, which in principle, can be compared to results from modeling of the near-field interaction.

If the tip apex touches the topographic convex or concave part, the topographic artifact may appear in the near field optical contrast. One can

consider surface roughness as a perturbation [58,59], and choose the local lowest point of topography as the reference point. Then if a convex feature is measured, the roughness may be treated as an additional layer above the reference level to the zeroth order approximation. For a convex-shaped feature, the position of the tip apex will be further away from the height of the reference level chosen here and the far field detected optical scattering amplitude should be less than that from a perfect flat surface without roughness due to the exponential decay of the evanescent wave modes in z direction. For samples with very smooth surfaces (surface roughness of about one nanometer or less), the near-field scattering amplitude and phase depend exclusively on the local dielectric function of the sample below the tip apex. However, surface roughness of the order of the radius of curvature of the tip apex can affect the near-field signal at the ten percent level. This is consistent with the data obtained on the insulating phase of VO<sub>2</sub> film with surface roughness of about 10 nm[60]. . However, the change in near-field amplitude is a factor of two or more in the metallic regions when VO<sub>2</sub> undergoes a thermally-driven insulator-to-metal transition. This change in the near-field amplitude due to the change in the local dielectric function of VO<sub>2</sub> is much larger than any signal variation due to topography. In cases where the changes in the signal due to variation of the local dielectric function and the topography are comparable, numerical methods can be used to model the data because simultaneous infrared and topography maps are obtained in a near-field infrared microscopy experiment.

## 4.2 Point dipole model

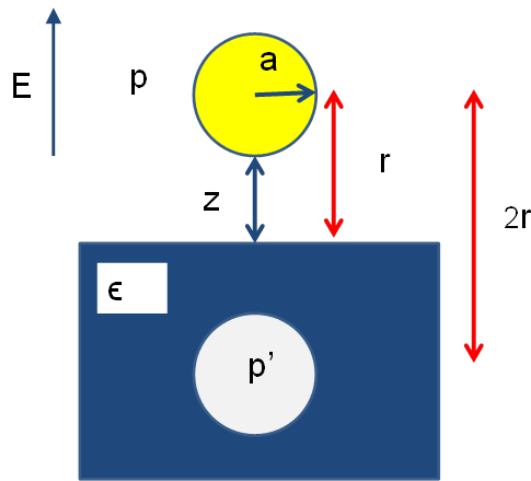


Figure 4.4. Schematic figure of the point dipole model.

Here we discuss the simplest model for optical near-field interaction. The tip apex is modeled by a polarizable sphere with radius  $a$  and the complex dielectric function  $\epsilon_p$ . This sphere sits above a flat dielectric surface with distance  $r$  from the center of the sphere to the top surface of the dielectric, and  $z$  is the distance from the bottom of the sphere to the top of the flat surface. When a linearly polarized electric field  $E$  with the polarization aligned within the incident plane encounters the sphere, it polarizes the sphere whose polarization  $p$  is given by:

$$p = 4\pi a^3 E (\epsilon_p - 1) / (\epsilon_p + 2) \quad 4.12$$

And we define  $\alpha$  as:

$$\alpha = 4\pi a^3 (\epsilon_p - 1) / (\epsilon_p + 2) \quad 4.13$$

The field in the upper domain generated by the induced charge inhomogeneity

within the flat dielectric or conducting medium below this polarized sphere can be effectively described by the field from an image dipole  $p'$  directly below the flat surface of the dielectric media with distance  $2r$  from the center of the polarizable sphere.

We can define a surface response function  $\beta$  as:

$$\beta = (\varepsilon - 1)/(\varepsilon + 1) \quad 4.14$$

where  $\varepsilon$  is the complex dielectric function of the flat dielectric media below the sphere. Then the magnitude of the image dipole is given by:

$$p' = \beta p \quad 4.15$$

The electric field which the oscillating dipole  $\vec{p}$  generates below it has the same polarization direction as this dipole and its magnitude can be written as:

$$E_{dipole}(r') = \frac{p}{2\pi r'^3} \quad 4.16$$

$r'$  is the distance of the observation point from the point dipole.

Then the final polarization of the dielectric sphere can be written as

$$p = \alpha \left( E + \frac{p'}{16\pi r^3} \right) \quad 4.17$$

Where the terms in brackets are the total electric field magnitude around the center of the sphere ( $E$  is the magnitude of the external, incident field and the second term in the bracket is the scattered field from the induced charge inhomogeneity from the sample below modeled by the image sphere. Hence,

$$p = \frac{\alpha}{1 - \frac{\alpha\beta}{16\pi r^3}} E \quad 4.18$$

The total far field radiation from the tip sample coupled system can be treated

approximately as the sum of the far field radiation of the two point dipoles.

$$\mathbf{p} = \frac{\alpha(1+\beta)}{1 - \frac{\alpha\beta}{16\pi r^3}} \mathbf{E} \quad 4.19$$

This step can be justified as follows: since the field within the near field zone from the induced charge on the sample surface can be well approximated by the quasi electrostatic field from the image dipole described above, we can set a virtual boundary condition enclosing the considered region:

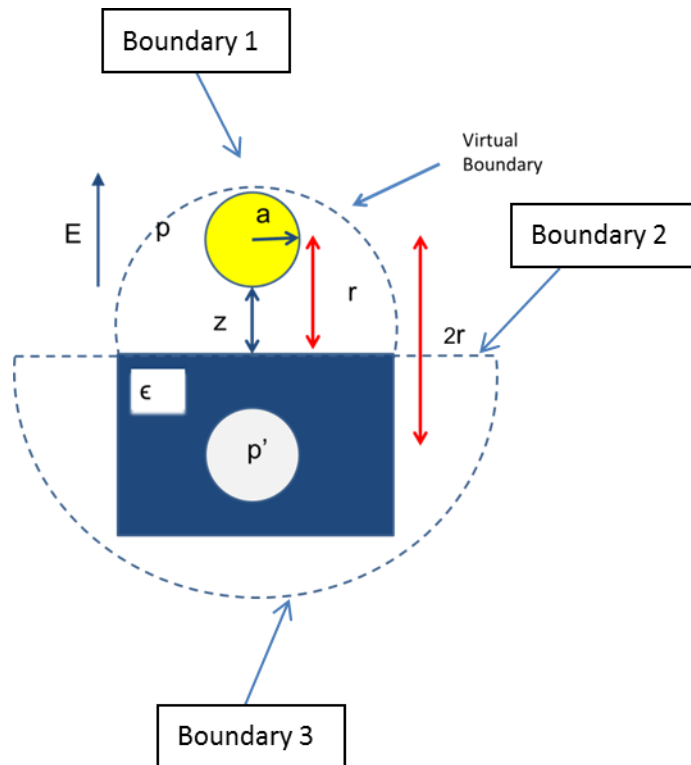


Figure 4.5. Schematic picture of the boundary value problem of the point dipole model.

While the upper hemisphere (Boundary 1) has a much smaller radius enclosing the near field zone of the sphere, the bottom hemisphere (Boundary 3) has an infinitely large radius and they share the same hemispherical center. An

infinitely large plane with an aperture (Boundary 2) connects the upper hemisphere and the lower hemisphere. The near field scattering field on boundary 1 from the sphere and sample region below it can be well approximated by the quasi electrostatic field from the system formed by the image dipole and the point dipole above it. However, the field on boundary 2 cannot be approximated well by this combined dipole system due to the quasi electrostatic nature of this model since a larger scale problem will involve the spatial phase distribution on this plane and the electrostatic description will enforce an in-phase electric field everywhere. Since the radius of the lower hemisphere is infinite, the electric field on it can be treated as zero. Due to an extended version of the Stratton-Chu formula [61], the far field electric and magnetic field distribution at the observation point (the position of the detector) can be obtained by an integral form of the electric and magnetic vector field on the closed surface boundary containing the source where the near field coupling and the far field propagating signals come from. One should note here that due to the omitted electrodynamic spatial phase distribution of the field on boundary 2, the far field signal can only be described approximately by formula 4.19.

This type of approximate calculation does not explicitly account for energy conservation and can overestimate the scattering intensity due to lack of information about the spatial phase distribution. However, the input energy should contain both the far field incident wave part and the mechanical tapping part. If the mechanical tapping of the AFM tip which tunes the near field coupling field between the tip apex and the sample below is included, it can generate the

energy transfer to the near field coupled system and induce the relevant propagating mode radiation itself. Experimentally, this process has been shown in Ref. [62].

Due to the mechanical tapping and the corresponding lock in detection of the higher harmonics, the radiation from the relevant charge polarization that is strongly modulated mechanically due to evanescent coupling is detected. Considering that the spatial frequency bandwidth of the  $k_z$  components and the  $k_{//}$  components are quite similar in magnitude in the elastic scattering region since  $k^2$  is conserved and  $|k_z|$  is much larger than  $|k_{//}|$  for the evanescent wave modes, the shape of the electric and magnetic near field around the charge distribution at the tip apex is nearly spherical in real space. This can be illustrated by measurement of the approach curve at higher order harmonic demodulation and demonstrated through lateral spatial optical resolution data on relatively insulating samples at a frequency far from resonances in the sample. So effectively, for the lock-in detection of the far-field scattered signals at different harmonics, the corresponding detection depth and lateral resolution can vary. Coarsely speaking, a spatially spherical shell-type near-field tomography can be done this way as shown in ref [63].

### **4.3 Monopole (or Finite Dipole) Model**

The charge polarization of the spatial region around the tip apex is important for higher order harmonic demodulation detection. If this part of the charge distribution due to the near field coupling is modeled accurately, the far

field higher order harmonic signal can then be calculated correctly.

The point dipole model considerably simplifies the charge distribution and serves as an approximation to the real situation. To improve the simulation, a monopole (or a finite dipole) model has been proposed [64].

Consider an extended spheroidal metallic body in the vicinity of a flat sample surface. This system is present in a homogenous external electric field. The near field is described by a finite dipole consisting of point charges  $Q_0$  and  $-Q_0$ . The charge  $Q_0$  near the sample surface induces the near-field interaction which further polarizes the spheroid. This additional charge polarization is modeled by a point charge  $Q_i$  at the spheroid's focus near the sample surface and another point charge  $-Q_i$  at the center of the spheroid. This charge configuration is shown in figure 4.6b. Due to far field detection, the fine structure of the charge distribution (as multipole terms) is usually smeared out, and the dipole term is reasonably assumed to dominate the electromagnetic radiation.

Two empirical parameters enter this model. The parameter  $L$  in ref [64] is the effective length of the near field polarized region along the tip fulfilling the constraint of equipotential and neutrality (which also requires the addition of point charges  $-Q_i$  and  $-Q_0$ ). This is because for a good metal, the electron dynamics happen at the time scale of femtoseconds, and the far- to mid-infrared optical oscillation we consider here happens at the time scale of thousands times slower than the former, so the quasi-electrostatic approximation still works. Next, the parameter  $g$ , a constant factor, is part of the response function of the tip to

external stimuli and can be fit to the experimental data (mainly the approach curve and the relative near-field contrast). The monopole model discussed here can be accurate if the distance between the tip apex and the sample surface is not too large (less than several times of the tip radius), and the radius of the tip and the distance between the tip apex and sample surface are much smaller than  $2L$ . Typical values of  $L$  and  $g$  are 300 nm and  $0.7e^{0.06i}$  with a tip radius 20 nm in Ref [64], and 1300 nm and  $0.999e^{0.145i}$  with a tip radius 250 nm in Ref [65].

Coarsely speaking, the spheroid's properties of equipotential and neutrality can be understood such that only the induced surface charge containing one node mainly contributes to the far field detection at higher harmonics as shown in figure 4.6 a (the right hand side one)[66].

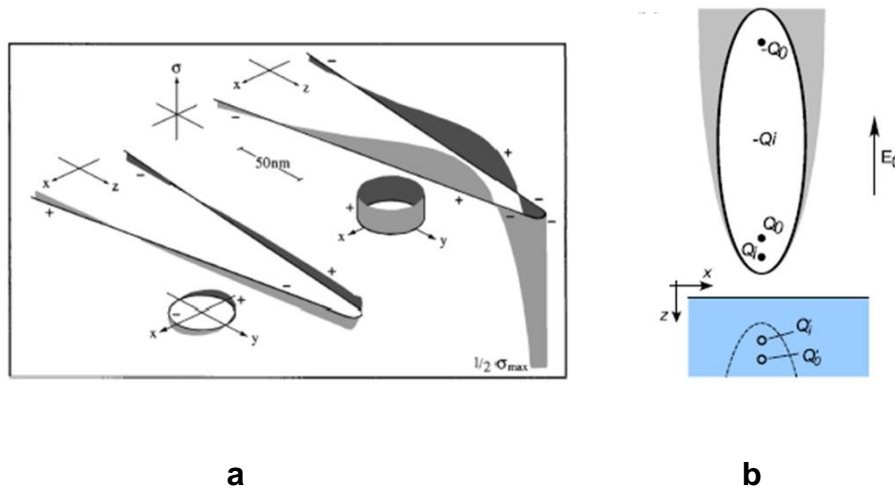


Figure 4.6 (a) induced surface charge distribution by two different monochromatic waves ;  $k$  vector along the  $z$  axis,  $E$  vector along the  $x$  axis (left);  $k$  vector along  $x$  axis,  $E$  vector along the  $z$  axis (right) [66]; (b) geometric configuration of the monopole model[64].

While the finite dipole model provides a better description of the experimental amplitude and phase data, its utility is limited to isotropic, bulk samples with extremely smooth surfaces. Further improvements in simulating the near-field interaction can be made using more advanced analytic models. However, given the need to precisely simulate realistic tip-sample geometry and the local anisotropic optical properties of the sample, numerical modeling of the near-field interaction is the most attractive way forward in this age when increased computational power is available to researchers.

## CHAPTER 5

### **Novel aspects of charge and lattice dynamics in $\text{La}_{0.67}\text{Sr}_{0.33}\text{MnO}_3$ film on Lanthanum Aluminate (LAO)**

The nature of metallic conduction in correlated systems like  $\text{La}_{0.67}\text{Sr}_{0.33}\text{MnO}_3$  (LSMO) is of considerable interest and an outstanding, unresolved problem. Certain ferromagnetic manganites are reported as bad metals because they appear to violate the Ioffe-Regel-Mott criterion [12]. Moreover, the optical conductivity in the metallic phase cannot be explained by a simple Drude model alone [9,10,12]. Based on low temperature reflection data, we use a Drude mode and two Tauc-Lorentz oscillators to analyze the low-frequency infrared behavior of an annealed  $\text{La}_{0.67}\text{Sr}_{0.33}\text{MnO}_3$  film grown on an  $\text{LaAlO}_3$  (LAO) substrate. Our model considers both electron and hole free carriers as well as localized carriers and differs from previous approaches [9,10,12] in that it provides a view that is consistent with other reported experimental results [67–73]. Unlike previous infrared studies, our analysis allows us to quantify the dynamical parameters (carrier densities, scattering rates, effective masses, and mean free paths) of both electrons and holes. We discover that LSMO is not a bad metal at low temperatures because the mean free path of the charge carriers exceeds the Ioffe-Regel Mott limit. We also report the first observation of splitting of an infrared phonon in the LSMO film which we attribute to local Jahn-Teller distortion. It provides evidence that local lattice distortions in correlated electron systems can be detected with infrared spectroscopy.

## 5.1 Experimental methods

$\text{La}_{0.67}\text{Sr}_{0.33}\text{MnO}_3$  (LSMO) films of thickness  $\sim 85$  nm were grown on (100) oriented LAO substrates, employing the pulsed laser deposition method using a KrF excimer laser. Films were grown at  $800^\circ\text{C}$  in an oxygen pressure of 400 mTorr and laser fluence  $\sim 1.5$  J/cm<sup>2</sup>, and subsequently post-annealed at  $800^\circ\text{C}$  for  $\sim 8$  hours in flowing oxygen to reduce oxygen vacancies and minimize any residual strain due to the compressive mismatch ( $\sim 1.8\%$ ) between the in-plane lattice constants of LSMO and (100) LAO. The as-grown and post-annealed films were analyzed using a 4-circle X-ray diffractometer. Films are single phase and (001) oriented (in cubic index) as indicated by  $2\theta$ - $\omega$  scans (Fig 5.1a). Rocking angle FWHM's are  $\sim 0.2^\circ$  indicating good crystallinity, and  $\Phi$ -scans indicate in-plane cube-on-cube in-alignment with the substrate. Post-annealing causes a decrease in the out-of-plane lattice constant and a concomitant decrease in dc resistivity, which is consistent both with strain relaxation and oxygenation. DC resistivity at room temperature in post-annealed films has been measured to be about  $300 \mu\Omega\text{cm}$  or lower, which is comparable to the best quality single crystals of LSMO with the same composition [10]. The temperature dependence of the resistivity shows metallic behavior below room temperature.

Near normal incidence reflectance measurements were performed to obtain the complex dielectric function of the LSMO film. Absolute reflectance data with unpolarized light was acquired in a vacuum Fourier transform infrared (FTIR) spectrometer (VERTEX 80v, Bruker Optics Inc.). A reflectance unit, mechanical translation system, and high vacuum equipment have been added to the FTIR

spectrometer in order to obtain the reflectance spectra at elevated and cryogenic temperatures. The sample was mounted on a sample holder attached to the end of the cold-finger of a variable temperature cryostat. The infrared reflectance data on the oxygen-annealed LSMO film is obtained from 30K to 400K with respect to a thick gold film in the spectral range from  $60 \text{ cm}^{-1}$  to  $6000 \text{ cm}^{-1}$ . In addition, room temperature spectroscopic ellipsometry data from  $0.6 \text{ eV}$  ( $\sim 4800 \text{ cm}^{-1}$ ) to  $6 \text{ eV}$  ( $\sim 48000 \text{ cm}^{-1}$ ) was obtained with a V-VASE ellipsometer (J. A. Woollam Co. Inc.). The higher frequency ellipsometry data enables a more accurate determination of the complex dielectric function in the infrared spectral range. The infrared and optical properties of the bare LAO substrate were also obtained via the spectroscopic methods described above. The infrared and optical spectroscopy data on the substrate and the LSMO film-substrate system were analyzed using WVASE32 software (J. A. Woollam Co. Inc.). Optical conductivity of the LSMO film was obtained by modeling the data with Kramers-Kronig consistent Drude, Lorentz and Tauc-Lorentz oscillators.

The surface morphology of the  $\text{La}_{0.67}\text{Sr}_{0.33}\text{MnO}_3$  film has been measured with tapping mode AFM. The analysis of the surface morphology provides important information about surface roughness that is utilized when modeling the optical data. An effective medium layer is used to include the surface roughness in the optical data analysis. The RMS value  $1.48 \text{ nm}$  of surface roughness for the LSMO film has negligible effect at infrared and visible wavelengths. However, if not taken into account, surface roughness can lead to systematic uncertainty (at the ten percent level) in the optical constants in the ultraviolet spectral range.

We estimate that the  $T_c$  of the insulator to metal transition is about 360 K from the sharp drop in the temperature-dependent dc resistivity data shown in Figure 5.1(b). The temperature dependence of the dc resistivity of the film is similar to that of a single crystal of comparable doping [16].

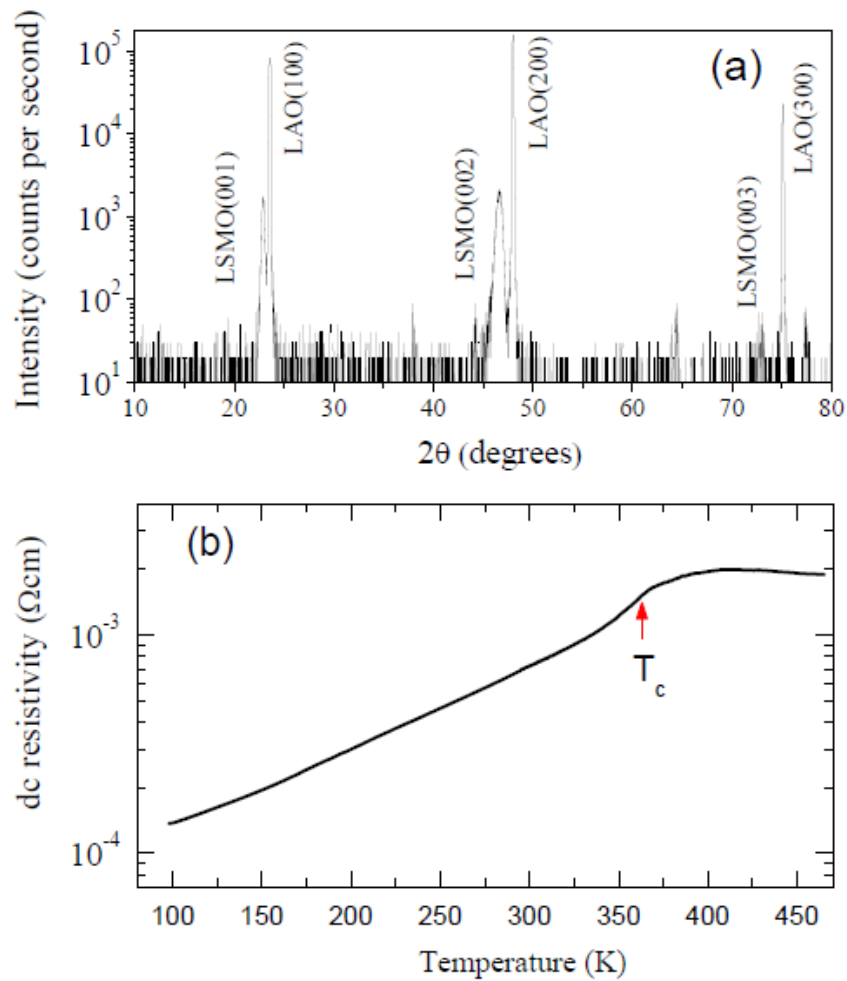


Figure 5.1 (a) XRD measurement for annealed  $\text{La}_{0.67}\text{Sr}_{0.33}\text{MnO}_3$  on  $\text{LaAlO}_3$  (b) Temperature dependence of dc resistivity of annealed  $\text{La}_{0.67}\text{Sr}_{0.33}\text{MnO}_3$  on  $\text{LaAlO}_3$ .

## 5.2 Metallic conductivity

The temperature dependent reflectance of the annealed  $\text{La}_{0.67}\text{Sr}_{0.33}\text{MnO}_3$  film is plotted in figure 5.2. The data shows the increase of the reflectance in the far- and mid- infrared with decreasing temperature.

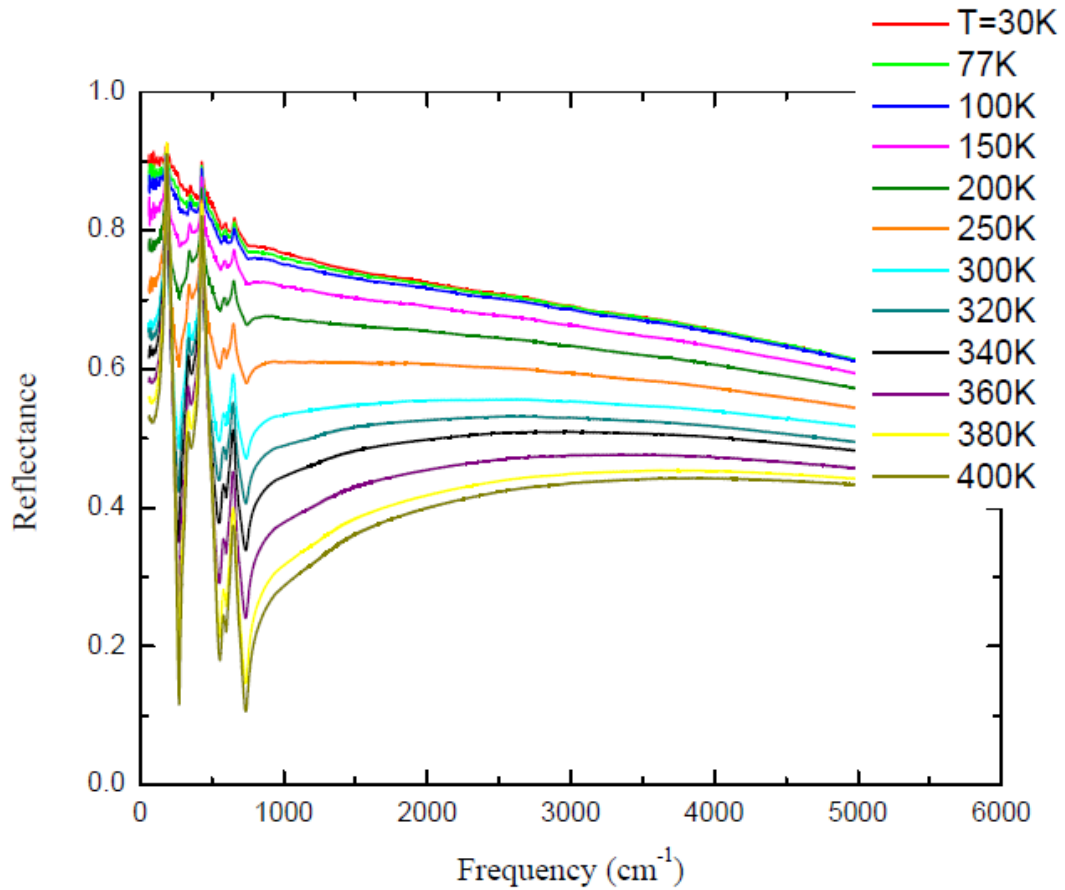


Figure 5.2 Frequency dependence of reflectance of annealed  $\text{La}_{0.67}\text{Sr}_{0.33}\text{MnO}_3$  film on  $\text{LaAlO}_3$  substrate from  $T=30$  K to  $T=400$  K.

The optical conductivity of the LSMO film is shown from  $60 \text{ cm}^{-1}$  to  $6000 \text{ cm}^{-1}$  for representative temperatures in Fig. 5.3. The low frequency conductivity at  $400 \text{ K}$  is consistent with an energy gap in the semiconducting phase. The

increase of the low frequency conductivity with decreasing temperature reveals the phase transition to a metallic phase. The growth of a narrow Drude-like feature below 200 K is observed. Moreover, as previous researchers have pointed out [9,10,12], a broad absorption feature centered about  $2500\text{ cm}^{-1}$  in the mid-infrared persists to the lowest measured temperature and must be considered in a definitive explanation of  $\text{La}_{0.67}\text{Sr}_{0.33}\text{MnO}_3$  film's metallic nature.

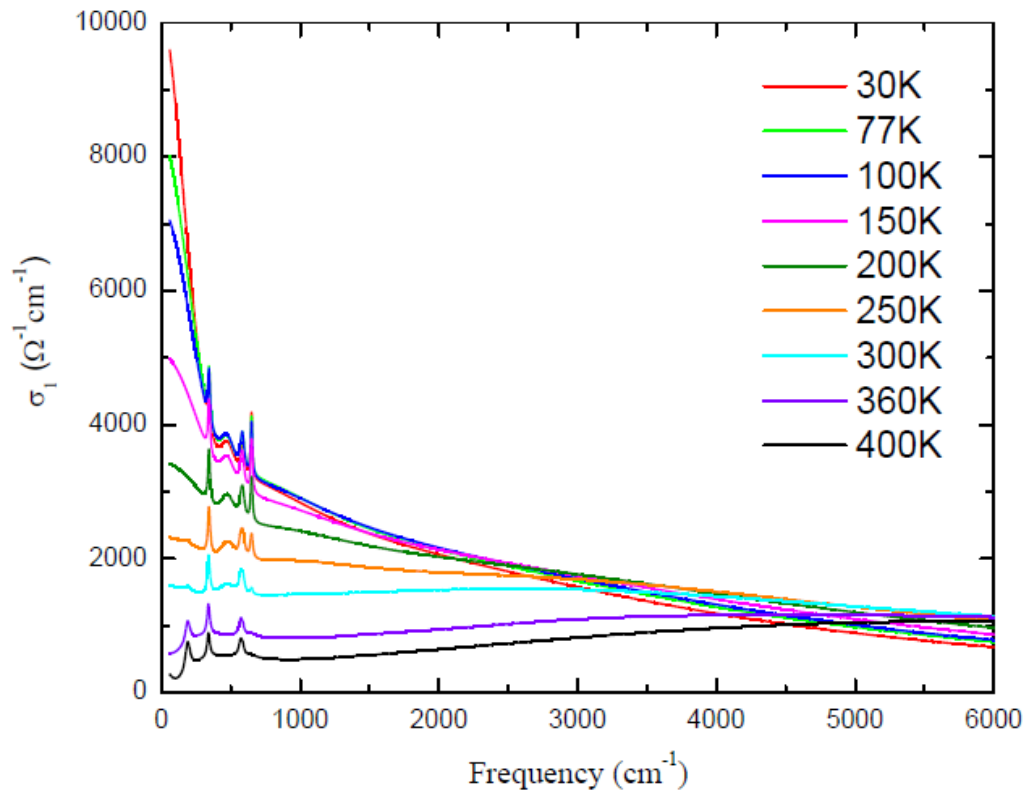


Figure 5.3 Frequency dependence of optical conductivity of annealed  $\text{La}_{0.67}\text{Sr}_{0.33}\text{MnO}_3$  film between  $T=30\text{ K}$  and  $T=400\text{ K}$ .

Previous infrared data in the literature on LSMO was explained with a combination of a simple Drude oscillator and a Lorentz oscillator [10]. However,

only one type of carrier is considered contributing to the Drude feature in Ref [10]. More recently, the extended Drude analysis has been applied by a few researchers instead of the conventional Drude-Lorentz model [9,12]. However, no more than one type of carrier is considered with the extended Drude approach. Existing experimental evidence clearly shows the necessity of considering two types of free carriers. The angle-resolved photoemission spectroscopy (ARPES) data show solid evidence of a nearly spherical electron pocket [67–70]. An electron–positron annihilation experiment measured the nearly cubic structure of the hole pocket in  $\text{La}_{0.7}\text{Sr}_{0.3}\text{MnO}_3$  [71]. The sizes and shapes of both the electron and hole Fermi surfaces are consistent with electronic structure calculations [74]. Furthermore, a two carrier model including both electron and hole carriers can explain the Hall effect data of  $\text{La}_{0.7}\text{Sr}_{0.3}\text{MnO}_3$  [72], while an exclusive hole-carrier model will lead to much higher hole density compared with the Sr doping level [75]. Here we show that two types of free carriers including electrons and holes with nearly equal mobilities need to be taken into consideration to explain the infrared data of metallic LSMO at lower temperatures.

The Hall coefficient [72,75] is positive and nearly temperature independent below 200K for unstrained LSMO samples with similar doping level to that studied in this work. The simplest explanation for these results is that the hole and electron mobilities are nearly equal and their ratio is independent of temperature. This follows from considering the analytic form for the Hall coefficient:

$$R_H = \frac{r_h n_h \mu_h^2 - r_e n_e \mu_e^2}{e(n_h \mu_h + n_e \mu_e)^2} \quad 5.1$$

where  $r_h$  and  $r_e$  are fixed Fermi surface shape factors for holes and electrons,  $n_h$ ,  $\mu_h$ ,  $n_e$ , and  $\mu_e$  are the number density and the mobility of holes and electrons respectively, and  $e$  is the electron charge [72].

If the mobilities of the hole and electron carriers are the same, then the expression for the Hall coefficient is independent of the mobilities:

$$R_H = \frac{r_h n_h - r_e n_e}{e(n_h + n_e)^2} \quad 5.2$$

$R_H$  now depends only on the carrier densities and the shapes of the Fermi surfaces. This sets the stage for analysis of our infrared reflectance data. We are able to fit the infrared reflectance at and below 200 K to one Drude [5] and two Tauc-Lorentz oscillators [76]. The Tauc-Lorentz oscillator is similar to a Lorentzian oscillator but has an additional energy gap parameter. The free carriers contribute to the narrow Drude feature. The quasi-localized charges lead to the broader mid-infrared mode in the optical conductivity which is described by the two Tauc-Lorentz oscillators as shown in Fig 5.4.

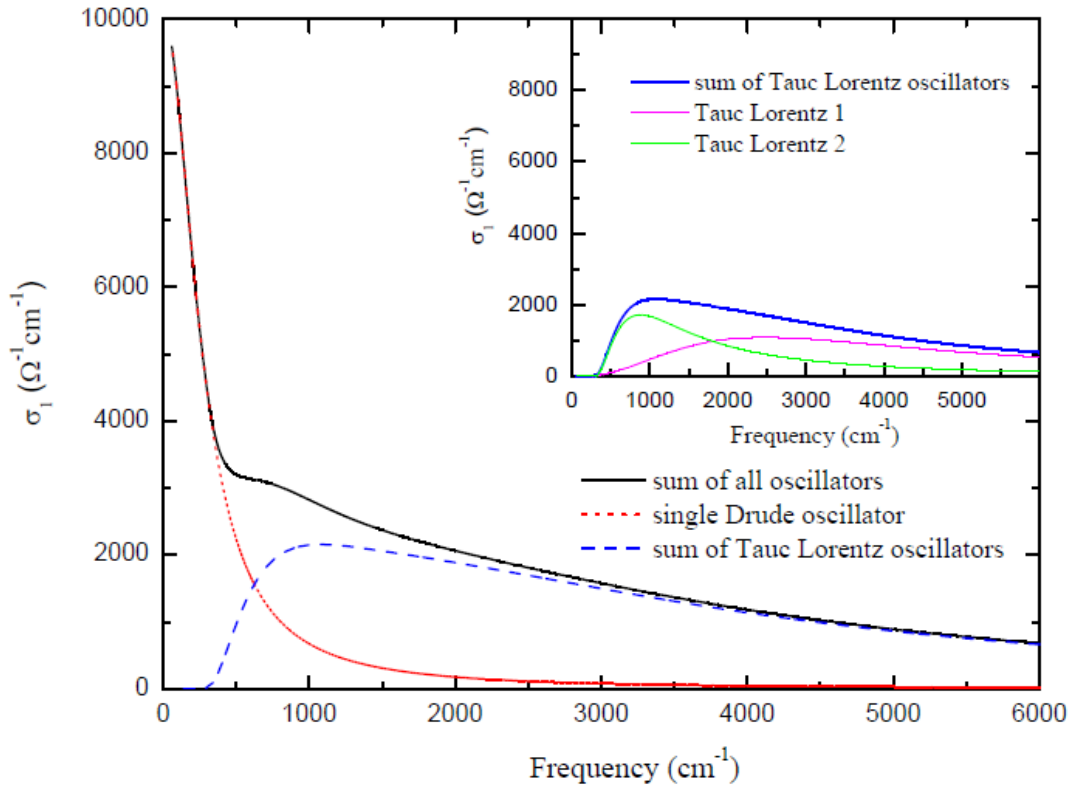


Figure 5.4 The electronic part of the optical conductivity at  $T=30$  K. The main figure consists of the sum of a single Drude oscillator and two Tauc-Lorentz oscillators. The inset shows the sum of the two Tauc-Lorentz oscillators.

Only one Drude mode is required to model the free-carrier infrared response. This suggests that the scattering rate (or inverse carrier lifetime) is the same for both electrons and holes at a particular temperature. Moreover, the carrier lifetimes for both electrons and holes have the same temperature dependence because one Drude mode is required to model the free carrier part of the infrared spectra for all temperatures  $\leq 200$  K. This fact taken together with the observation of the same mobilities of electrons and holes, tells us that both types of carriers have the same effective masses. From fits to the infrared

reflectance data, we obtain the temperature dependence of the plasma frequency and the scattering rate of the free-carriers and these quantities are shown in Fig. 5.5.

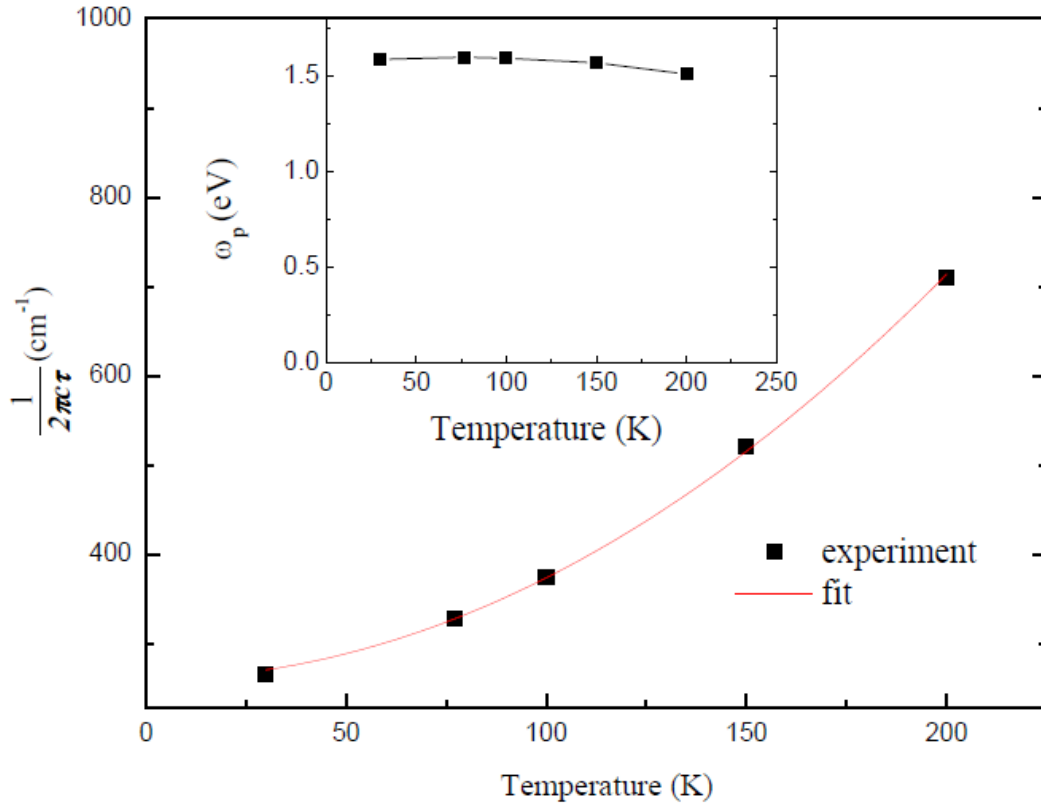


Figure 5.5 The temperature dependence of the scattering rate. The inset shows the temperature dependence of the plasma frequency of the Drude mode.

The plasma frequency has the form  $\omega_p = \left(\frac{4\pi n e^2}{m^*}\right)^{\frac{1}{2}}$  and depends upon the ratio of the free carrier density ( $n$ ) and effective mass ( $m^*$ ). If we take the mass of the carriers to be nearly equal to the free electron mass in accord with the ARPES dispersion near the Fermi energy [67], we find the total free carrier density from

our infrared data to be approximately  $1.8 \times 10^{21} \text{cm}^{-3}$  (0.1 free carriers per Mn site). From the Hall effect data [72], one obtains the ratio of 7:3 for the holes and electron carrier densities assuming identical mobilities. The model of two-carriers with nearly equal mobilities and with the holes as majority carriers is qualitatively consistent with a positive and temperature independent Seebeck coefficient at low temperatures [73][77].

We also attempted to calculate the density of electron and hole carriers from the size of Fermi surfaces measured by ARPES and electron-positron annihilation. The (pseudo-cubic) lattice constant  $a$  of LSMO is about  $3.9 \text{ \AA}$  [70]. According to Ref [68], and references therein, a sphere with radius between  $0.43 \frac{\pi}{a}$  and  $0.48 \frac{\pi}{a}$  can be used to estimate the size of the electron pocket. A spin polarization of 50% for the electrons is assumed which is consistent with spin resolved photoemission data [68]. A Fermi surface radius of  $0.45 \frac{\pi}{a}$  is adopted for calculating the electron carrier density. The hole pocket is approximated by a cube with side length of  $0.65 \frac{2\pi}{a}$  [71]. Holes which are the dominant carriers are treated as completely spin-polarized. This is consistent with the existence of a nearly half-metallic ferromagnetic ground state [78]. Carrier densities of  $1.1 \times 10^{21} \text{cm}^{-3}$  (0.07 carriers per Mn site) for the electrons and  $4.6 \times 10^{21} \text{cm}^{-3}$  (0.27 carriers per Mn site) for the holes are obtained from the volume enclosed by the electron and hole Fermi surfaces according to the band structure picture.

However, the free carrier density from infrared data ( $1.8 \times 10^{21} \text{cm}^{-3}$ ) is significantly smaller than that obtained from the simple free carrier interpretation

of the ARPES and electron-positron annihilation data (approximately  $5.7 \times 10^{21} \text{cm}^{-3}$  which is approximately 0.34 carriers per Mn site). We explain this difference by postulating that about one-third of carriers in the electron and hole pockets are actually mobile while the remaining majority are localized due to charge and magnetic correlation effects or domain wall scattering induced by the compressive strain of the LAO substrate [79]. Averaged to every Mn site, approximately 0.1 free carriers are obtained compared to 0.33 expected based on the Sr concentration. This again justifies our assertion that the mid- infrared absorption comes from localization induced by correlation effects or domain wall scattering. If we assume that both free and localized charge carriers have effective masses almost equal to the bare electron mass, the number density of charge carriers obtained by integrating the optical conductivity below  $6000 \text{cm}^{-1}$  at low temperatures is approximately  $5 \times 10^{21} \text{cm}^{-3}$ , which accounts for nearly all the carriers obtained from the size of the electron and hole pockets within the single particle picture.

The temperature dependence of the relaxation rate of the free carriers is shown in Fig 5.5. They can be fit by a quadratic curve of the form  $A+BT^2$ , where  $A$  is the residual scattering rate and  $B$  is the coefficient of the quadratic term. However, the coefficient of the quadratic temperature-dependent term obtained from the fit is  $1.88 \times 10^9 \text{K}^{-2}\text{s}^{-1}$  which is about 270 times larger than the value of  $6.95 \times 10^6 \text{K}^{-2}\text{s}^{-1}$  in Au which is a good metal. We also note the large residue scattering in the limit of low temperatures in LSMO [18]. To estimate the mean free path of the free carriers, we assume both electron and holes have

approximately equal Fermi velocity  $5 \times 10^5 \text{ m s}^{-1}$  obtained from the measured dispersion in the ARPES data. Then the mean free path is approximately 10 nm at 30 K and 3.5 nm at 200 K compared with the Fermi wavelength of 1.4 nm and lattice constant about 3.9 Å. At 200 K and lower temperatures, the mean free path of the coherent carriers exceeds the Ioffe-Regel-Mott limit. Our model cannot be applied to the conductivity above 200 K because of the expected instability towards insulating behavior and possible phase-separation. We note that the quadratic temperature dependence of the scattering rate with an anomalously large coefficient ( $B$ ), may be qualitatively explained within the framework of the hidden Fermi liquid picture [80]. At the same time, the large residual scattering at very low temperatures would also need to be accounted for in a realistic theoretical model. Besides scattering due to impurities and domain walls induced by the compressive strain of the substrate [79], the many body effects involving dynamical electron-electron interactions may make significant contribution to the low temperature residual scattering rate observed in our experiments [81]. We also note that the spectral weight of the Drude mode has a weak temperature dependence below 200 K (see inset of Fig. 5.5) which is consistent with the nearly temperature-independent Hall and Seebeck coefficients. There is also a mild increase (less than 10 %) in the spectral weight of the mid-infrared feature with decreasing temperature and this can be explained by spectral weight transfer from higher frequencies.

We also attempted to fit the infrared reflectance data with two Drude oscillators, one narrow and the other quite broad. A reasonable fit was obtained

and two possible scenarios were explored. First, the narrow Drude was assumed to arise from hole carriers and the broad Drude from the electron carriers. The second scenario was to reverse the assignment of the two Drude oscillators. However, neither scenario gave results that were consistent with the Hall effect measurements of Ref [72] indicating that these alternative models are not realistic.

### 5.3 Infrared active phonons

The rhombohedral primitive cell of  $\text{La}_{0.67}\text{Sr}_{0.33}\text{MnO}_3$  contains 10 atoms and corresponds to 30 phonon modes. Group theory predicts that the rhombohedral crystal exhibits 8 infrared active phonon modes  $3A_{2u} + 5E_u$  and 5 Raman active phonon modes as  $A_{1g} + 4E_g$ . Including 5 silent modes  $2A_{1u} + 3A_{2g}$  and 3 acoustic modes, there are a total of 30 modes including double degeneracy of  $E_u$  and  $E_g$  modes [82]. Our thin film has the orientation of [001] in cubic notation. The [111] axis of the rhombohedral unit cell coincident with the [111] axis of the cubic cell aligns with an angle about  $35^\circ$  relative to the sample surface. However, the optical anisotropy of LSMO can be better described with a hexagonal unit cell instead of the rhombohedral primitive cell. The  $c_h$  axis of the larger hexagonal cell is in the same direction as the [111] axis of the rhombohedral cell [83]. Four possible rhombohedral domains induced by twinning exist in the film [83]. As a result, all 8 infrared active phonon modes could be observed in principle.

The infrared-active phonon features of annealed  $\text{La}_{0.67}\text{Sr}_{0.33}\text{MnO}_3$  film are shown in Fig 5.6.

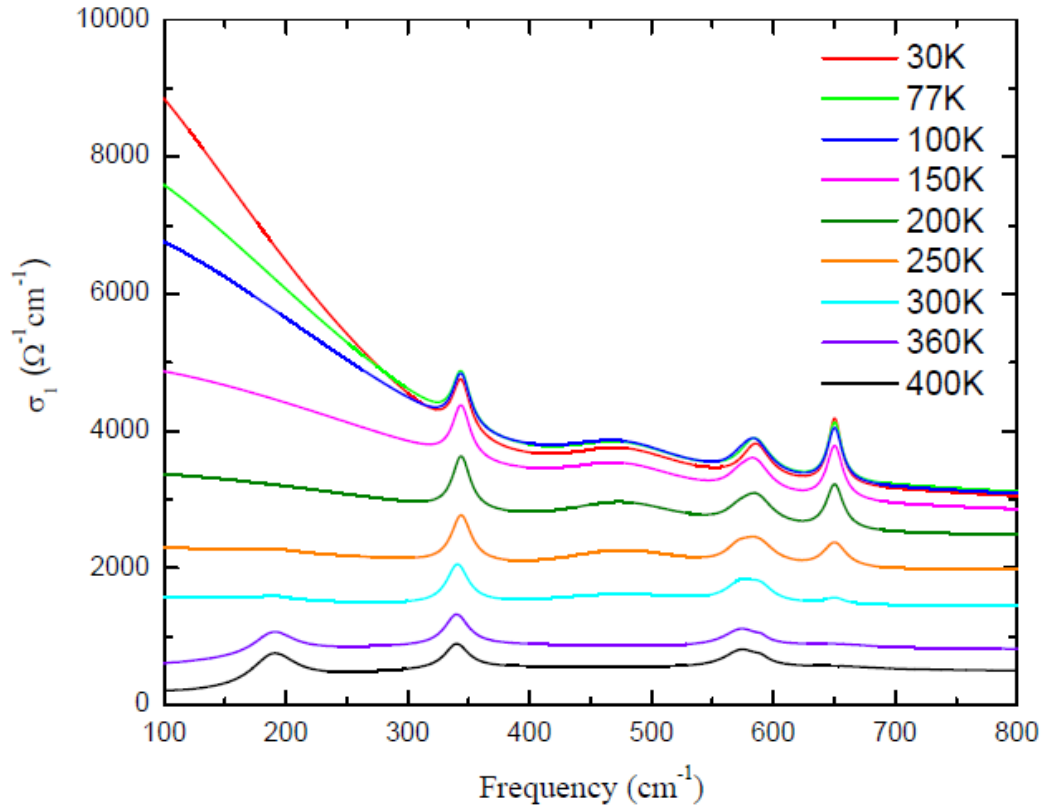


Figure 5.6. Frequency dependence of the optical conductivity of  $\text{La}_{0.67}\text{Sr}_{0.33}\text{MnO}_3$  film measured at different temperatures from  $T=30\text{ K}$  to  $T=400\text{ K}$ . The phonon features between  $100\text{ cm}^{-1}$  to  $800\text{ cm}^{-1}$  are shown. This figure is a zoom-in of Fig. 5.3.

We can clearly resolve only the most prominent phonons around  $340\text{cm}^{-1}$  and  $580\text{ cm}^{-1}$  in the reflectance spectra. Both of them are  $A_{2u}$  modes. The  $340\text{ cm}^{-1}$  is the bending mode and the  $580\text{ cm}^{-1}$  is the stretching mode [16]. The polarization of the  $A_{2u}$  mode phonons is along the  $[111]$  direction of the cubic cell and thus the  $c_h$  direction of the hexagonal unit cell [84]. As a result, they can be clearly resolved by our near normal reflectance measurement with unpolarized light. The reasons that other phonons cannot be clearly resolved are following: lower signal from the film whose thickness is much less than infrared

wavelengths, the presence of strong phonon features of LAO substrate, and the screening effect of mobile charges in the metallic phase. The oscillator parameters of the  $340\text{ cm}^{-1}$  infrared phonon mentioned above agrees with previous reported results [15–17]. The inclusion of two additional Lorentzian oscillators was required in order to improve the fits to the data and these oscillators likely correspond to infrared active phonons. The infrared phonon around  $200\text{ cm}^{-1}$  is present in the insulating phase but it is heavily screened by the high reflectivity of metallic electrons and cannot be resolved at lower temperatures. The oscillator parameters for the phonon at  $650\text{ cm}^{-1}$  have some uncertainty because the oscillator frequency coincides with that of the strong phonon feature from LAO substrate.

We emphasize the observation of the splitting of the infrared phonon mode around  $580\text{ cm}^{-1}$  in  $\text{La}_{0.67}\text{Sr}_{0.33}\text{MnO}_3$  film that has not been reported in earlier works to the best of our knowledge. We are able to resolve this splitting due to the high spectral resolution of  $2\text{ cm}^{-1}$  used to obtain the data. We zoom in on the  $580\text{ cm}^{-1}$  infrared phonon shown in Fig. 5.7 (a) and we see that the phonon peaks are separated by  $17\text{ cm}^{-1}$ . This phonon is a stretching mode which is more easily visualized and discussed in a pseudo-cubic unit cell [15][85]. The main characteristic feature of the stretching mode is that the manganese atom within the oxygen octahedra moves against the oxygen atoms in the axial direction. This phonon mode usually corresponds to a higher frequency than the bending mode which has the manganese atom and the axial oxygen atoms moving along the same direction but against the 4 oxygen atoms within the horizontal plane.

These two modes are sensitive to the bond length and strength along the axial direction connecting the oxygen atoms and manganese atom. The infrared phonon splitting observed in our experiment can be explained by local Jahn-Teller distortion which modifies the bond length and strength along the axial direction of the oxygen octahedra. The Jahn-Teller effect in the paramagnetic insulating phase distorts the oxygen octahedra making the Mn-O bond length larger along the axial direction. The oxygen octahedra near the Sr sites remain undistorted because hole doping by Sr leads to empty Mn site  $e_g$  orbital, thus no Jahn Teller distortion is expected there. This distortion is reduced as the film becomes ferromagnetic metallic and subsequently vanishes at the lowest temperatures. Our observations thus confirm previous reports of this phenomena including both PDF analysis and XAFS experiments [86–88]. The local Jahn-Teller distortion is randomly oriented [87]. Thus the Sr doping introduces random distribution of undistorted oxygen octahedra and different bond length and strength along the axial direction within the oxygen octahedra in the insulating regions. The mixed distribution of the different kinds of Mn-O bonds along the axial direction splits the stretching phonon near  $580\text{ cm}^{-1}$ .

The phonon splitting that we observe is quite similar to that observed by Barker *et al.* in mixed  $\text{KMgF}_3\text{-KNiF}_3$  crystal[89]. The random distribution of different bonds caused by the random distribution of Mg and Ni is not simply a macroscopic mixing of the dielectric function of two different materials. The mixed  $\text{KMgF}_3\text{-KNiF}_3$  crystal also has perovskite structure with Mg and Ni atoms at the same locations as Mn in our LSMO system. The phonon splitting observed in the

reststrahlen band within the  $200\text{ cm}^{-1}$  and  $300\text{ cm}^{-1}$  region in the mixed  $\text{KMgF}_3$ - $\text{KNiF}_3$  crystal corresponds to the stretching mode, a counterpart of the situation in LSMO. The main difference is that the phonon splitting of the mixed  $\text{KMgF}_3$ - $\text{KNiF}_3$  crystal involves both the mass difference of Mg and Ni atoms and the variation of the bond strength, while in LSMO only the variation of bond strength is involved. The phonon splitting will remain in the hypothetical situation in which the Ni atom is replaced by a much lighter atom with similar mass to Mg atom but with the bond strength unchanged and non-zero Grüneisen constant [89]. This hypothetical situation is exactly the analogy to what we meet in our LSMO system. Thus the phonon splitting observed in LSMO can be qualitatively explained within the framework of the mixed crystal theory once changes in bonding caused by local Jahn-Teller distortion are taken into consideration. The disappearance of the phonon splitting at low temperatures as seen in Fig.5.7b is consistent with the vanishing of Jahn-Teller distortion deep into the metallic phase.

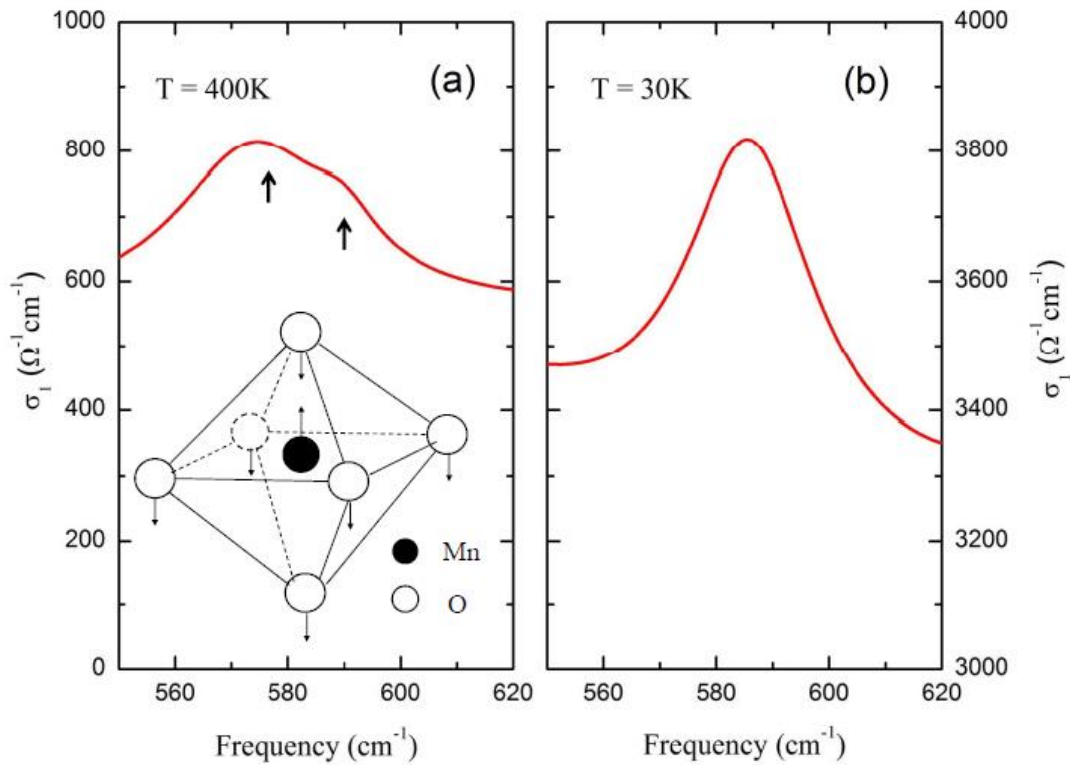


Figure 5.7 (a) Optical conductivity at  $T = 400 \text{ K}$  shows splitting of the stretching mode phonon due to Jahn-Teller distortion. The two arrows are displayed at the center frequencies of  $573 \text{ cm}^{-1}$  and  $590 \text{ cm}^{-1}$  of two Lorentz oscillators that were used to model the phonon doublet. A schematic figure of the stretching mode vibration is shown in the inset. (b) Optical conductivity at  $T = 30 \text{ K}$  shows a single phonon mode.

## 5.4 Conclusions

We performed temperature dependent infrared spectroscopy on an annealed  $\text{La}_{0.67}\text{Sr}_{0.33}\text{MnO}_3$  film grown on (100)  $\text{LaAlO}_3$  substrate. The electronic part of the optical conductivity is modeled with one Drude and two Tauc Lorentz oscillators. Our analysis is consistent with the presence of hole and electron carriers in metallic LSMO, and by reconciling our infrared data with Hall effect, ARPES, and electron-positron annihilation experiments, we find that these two

types of carriers have essentially similar dynamical properties. Thus, we provide a complete picture of metallic conduction in LSMO including quantitative values of the dynamical parameters and number densities of both electron and hole charge carriers. Our results indicate that only one-third of the doped charges in LSMO are mobile. The mean free path of the mobile carriers exceeds the Ioffe-Regel-Mott limit of metallic transport and therefore metallic LSMO cannot be regarded as a bad metal. The majority of the doped charge is localized due to many-body correlation effects or domain wall scattering and appears as a broad mid-infrared feature in the optical conductivity. Our analysis reveals a quadratic temperature dependence of the scattering rates of both electrons and holes, consistent with the recently proposed “hidden Fermi liquid” model [80]. The quadratic temperature dependence would have been obscured if the extended Drude model had been used to analyze the infrared data. We report the first observation of splitting of the stretching phonon mode induced by local Jahn-Teller distortion in this material. We provide an explanation of this phenomenon based on the mixed crystal theory [89]. Our work provides evidence that infrared spectroscopy can be utilized to detect local lattice distortions in correlated electron systems.

## CHAPTER 6

### **Dichotomy between bulk and interface properties of $\text{La}_{0.67}\text{Sr}_{0.33}\text{MnO}_3$ thin films**

#### **6.1 Introduction**

The colossal magnetoresistive manganites have been extensively studied because their entangled electronic, magnetic and structural degrees of freedom lead to remarkable magnetic and transport properties that also hold promise for applications [90]. Specifically, the hole-doped manganite  $\text{La}_{0.67}\text{Sr}_{0.33}\text{MnO}_3$  (LSMO) has attracted special interest because of potential spintronics applications given that it is a wide-band half-metallic ferromagnet with a coupled magnetic and metal-insulator phase transition near room temperature [91,92]. Similar to other classes of manganites, the properties of LSMO were found to be influenced by competing ground states that led to spatial phase inhomogeneity at nanometer and micrometer length-scales in crystals and films depending upon strain, morphology, and sample synthesis methods. This was inferred by employing probes with nanoscale spatial resolution, particularly, magnetic force microscopy (MFM) and scanning tunneling microscopy (STM) [23,25,79,93–101]. In recent years, there has been a renewal of interest in thin films of LSMO grown on various substrates. The substrate profoundly affects the properties of LSMO at the film-substrate interface leading to the emergence of novel phases at the interface that do not occur in the bulk material or thicker films [102–107]. It has been suggested that LSMO at the interface may be spatially inhomogeneous due to phase segregation [103,108]. However, this has not been directly observed

because neither MFM nor STM is particularly suitable for probing the film-substrate interface properties. Furthermore, due to the difficulty of zero field measurement with MFM and the application of STM to such broad continuous metal-insulator transition, accurate nano-imaging of critical phenomena in second order phase transitions such as in LSMO thin films is hard to achieve by these methods.

In the work contained in this chapter, we employ scattering-type scanning near-field infrared microscopy (s-SNIM) with 20 nm spatial resolution to probe both bulk and interface properties of 18 nm thick LSMO films grown on SrTiO<sub>3</sub> (STO) substrates. We directly observe phase coexistence at the LSMO/STO interface that is unaffected by increasing temperature. In contrast, the bulk of the film undergoes a continuous, non-percolative phase transition from a metal to an insulator upon increasing temperature. Moreover, we directly observe for the first time with s-SNIM, slow fluctuation of the local conductivity in LSMO near its phase transition temperature.

## **6.2 Experimental Methods**

Epitaxial (100) La<sub>0.67</sub>Sr<sub>0.33</sub>MnO<sub>3</sub> films of 47 unit cell (~18 nm) thickness were grown on (100) STO substrates with pulsed laser deposition. The as-received STO substrates were first acid etched and annealed to obtain TiO<sub>2</sub> terminated surfaces. A KrF excimer laser ( $\lambda = 248$  nm) was used for ablation at an energy density of 0.5 J/cm<sup>2</sup> and a 5 Hz repetition rate. The substrate temperature was kept at 780°C and the films were grown in an oxygen

atmosphere of 60 – 70 mTorr. The temperature dependent resistivity of the film is shown in Figure 6.1(a) for heating and cooling runs. No hysteresis is observed in the temperature dependent resistivity data which agrees with a second order phase transition. The phase transition from the ferromagnetic metallic phase at low temperatures to a paramagnetic insulating phase at high temperatures can be observed above 300 K in dc resistivity. The derivative of the resistivity with respect to temperature (Figure 6.1(b)) shows a maximum value at  $T^* \sim 330$  K which we define as the nominal phase transition temperature. The sample topography does not change during the heating process as demonstrated in Figure 6.1 (c) (d).

Apertureless scanning near-field infrared microscopy based on the tapping mode atomic force microscope (AFM) along with a pseudo-heterodyne optical interferometric setup is applied to obtain the amplitude and phase of the near field scattering signals. A cantilevered tip of an AFM tapping sinusoidally at  $\approx 250$  kHz is used in close proximity to the sample surface. The platinum-coated tip is illuminated by a focused, monochromatic infrared beam of  $10.8\mu\text{m}$  wavelength from a  $\text{CO}_2$  laser. A feedback mechanism allows constant light intensity from the  $\text{CO}_2$  laser over many hours. The scattered light is recorded by a mercury cadmium telluride (MCT) detector. The radius of curvature of the tip apex ( $\approx 20$  nm) determines both the mechanical and the optical resolution. The near-field infrared amplitude data presented in this work was obtained at the third harmonic demodulation of the tapping frequency of the AFM tip.

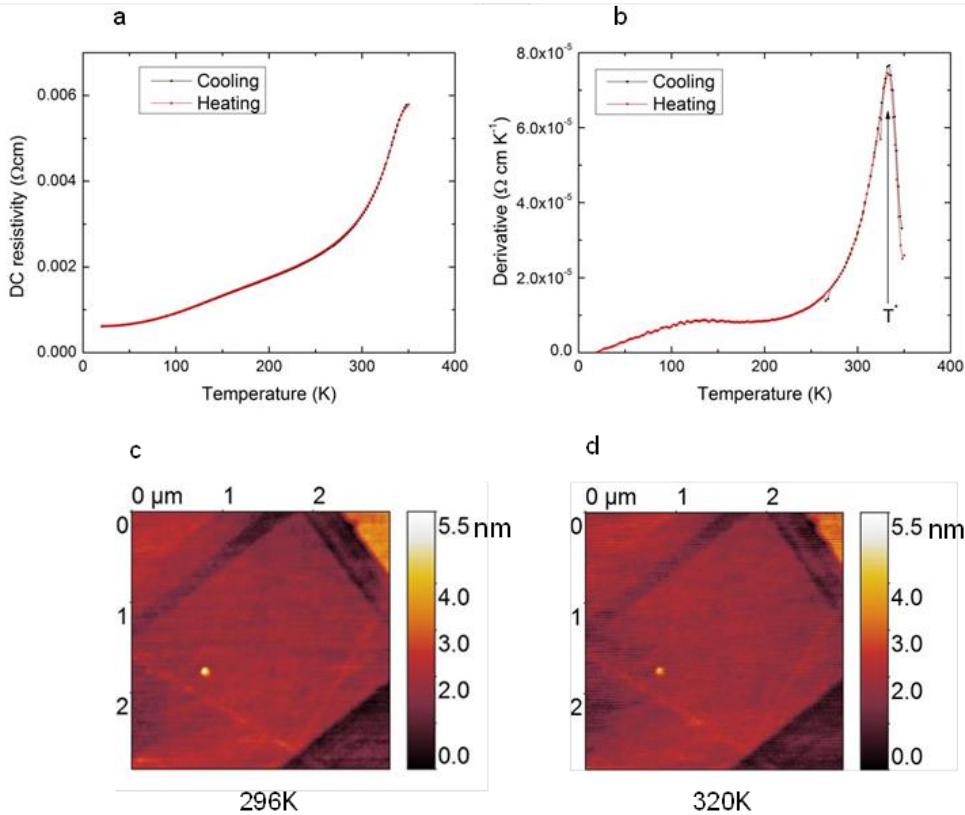


Figure 6.1 Resistivity and AFM measurements. (a) The temperature dependent resistivity of the 18 nm  $\text{La}_{0.7}\text{Sr}_{0.3}\text{MnO}_3$  thin film grown on  $\text{SrTiO}_3$  substrate measured in both heating and cooling runs. (b) Derivative of the resistivity with respect to temperature is plotted as a function of temperature;  $T^*$  indicates the nominal temperature of the phase transition. (c) and (d), AFM measurements of the surface topography in the same area obtained at 296 K and 320 K respectively.

The sample was mounted with silver paint on an aluminum heating stage designed in-house. A heater and thermometer are mounted on the heating stage and are electrically connected to a Lakeshore temperature controller that allows us to vary and control the temperature with the stability of less than 0.1 K. This variable temperature set-up was used in conjunction with the s-SNIM instrument from Neaspec GmbH for obtaining temperature dependent near-field infrared data.

We present the topography of the LSMO film at 296 K and 320 K in Figure 6.1c,d. Notice the steps of about 2 nm in the LSMO film which are likely due to steps on the substrate. Elsewhere, in much of the scanned area, the film is remarkably featureless to within 1 nm vertical resolution of the AFM. An exception is an island in the scanned area of about 5 nm height which is seen as a bright speck in the lower left quadrant of the topographic images. This island along with the peculiar pattern of steps in the scanned area allows us to relocate the same area in case of thermal drift of the sample upon changing the temperature. Note that the topography of the LSMO film in the same area shows no variation with temperature as expected. Remarkably, as we show in Figure 6.2, the infrared near-field amplitude signal in the same area shows spatial variation at all measured temperatures.

### **6.3 Results and discussion**

The spatial and temperature dependence of the infrared near-field amplitude in a common area are presented in Figure 6.2. The same color scale is used for all measured temperatures. One clearly sees patches of lower amplitude near the center of the scan area, around the 5 nm island, and near some of the steps in the film. There are no topographic features near the center of the scan that can potentially affect the infrared near-field signal. Therefore, the infrared near-field amplitude contrast is due to differences in the local dielectric function: The lower amplitude is from regions that are more insulating compared to the surrounding material. Note that the island appears as a dip in the near-field infrared signal. However, the topography in the immediate vicinity of the island is

featureless. Hence, the low near-field infrared signal around the island is due to this region's relatively insulating character and not due to any topographic artifacts. Regions near some of the steps are also relatively insulating based on the low near-field infrared amplitude. The static patches of insulating character persist at all measured temperatures and their spatial configuration is unaffected by temperature. In addition, we observe that the overall near-field infrared signal in the scan area decreases with increasing temperature as the film undergoes a phase transition from the more metallic to the more insulating phase. For smooth surfaces, the infrared near-field amplitude depends entirely on the local dielectric function and hence on the local conductivity of the material. The spatial variation and temperature dependence of the near-field infrared amplitude is observed because the conductivity varies as a function of position as well as with temperature.

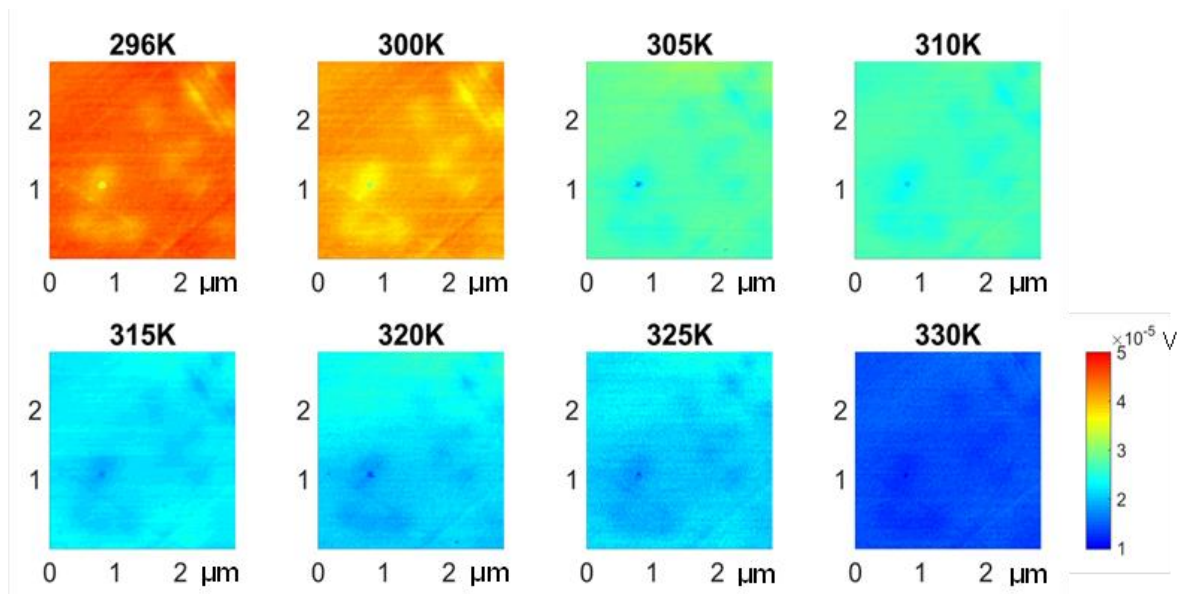


Figure 6.2. Amplitude of the scattering near field infrared signals at different temperatures. Amplitude of the scattering near field infrared signals are shown using a

common color scale. Scans are carried out in the same spatial area of  $2.84 \mu\text{m} \times 2.84 \mu\text{m}$  at different temperatures between 296 K and 330 K during a heating run. Interferometric detection is carried out at the infrared wavelength of  $10.8 \mu\text{m}$ .

To gain further insight into the thermally-driven local dynamics of the phase transition, scans are normalized to the maximum near-field infrared amplitude of each scan, and plotted in Fig. 6.3. These self-normalized scans reinforce the observation of persistent patches of lower near-field infrared amplitude whose size and shape does not vary with temperature. The infrared signal from the more insulating regions is about 20 percent lower than the signal from the more metallic ones.

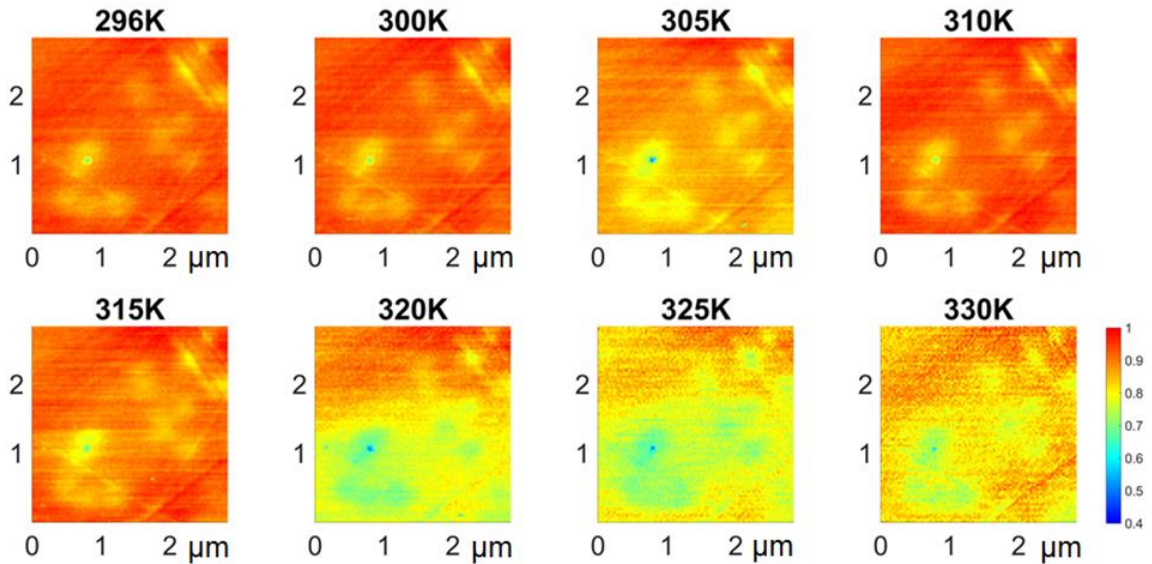


Figure 6.3: Self normalized amplitude of the scattering near field infrared signals. The amplitude of the scattering near field infrared signals in the scans shown in Figure 6.2 is normalized to the maximum value in each scan. All scans have spatial area  $2.84 \mu\text{m} \times 2.84 \mu\text{m}$ , and are shown in the same color scale.

The ratios obtained by dividing the near-field infrared amplitude scans at different temperatures by the scan at room temperature are shown in Fig. 6.4. The persistent spatial variation of the near-field infrared amplitude at all temperatures is canceled out in much of the scanned area by taking these ratios except for the island and in the vicinity of some of the steps on the film. The imperfect cancellation for the island is due to topography but for the steps it could be due to either topography or local variation of the conductivity. Since these ratios are spatially uniform in much of the scanned area, we deduce that the bulk of the film undergoes a continuous, uniform metal-insulator transition.

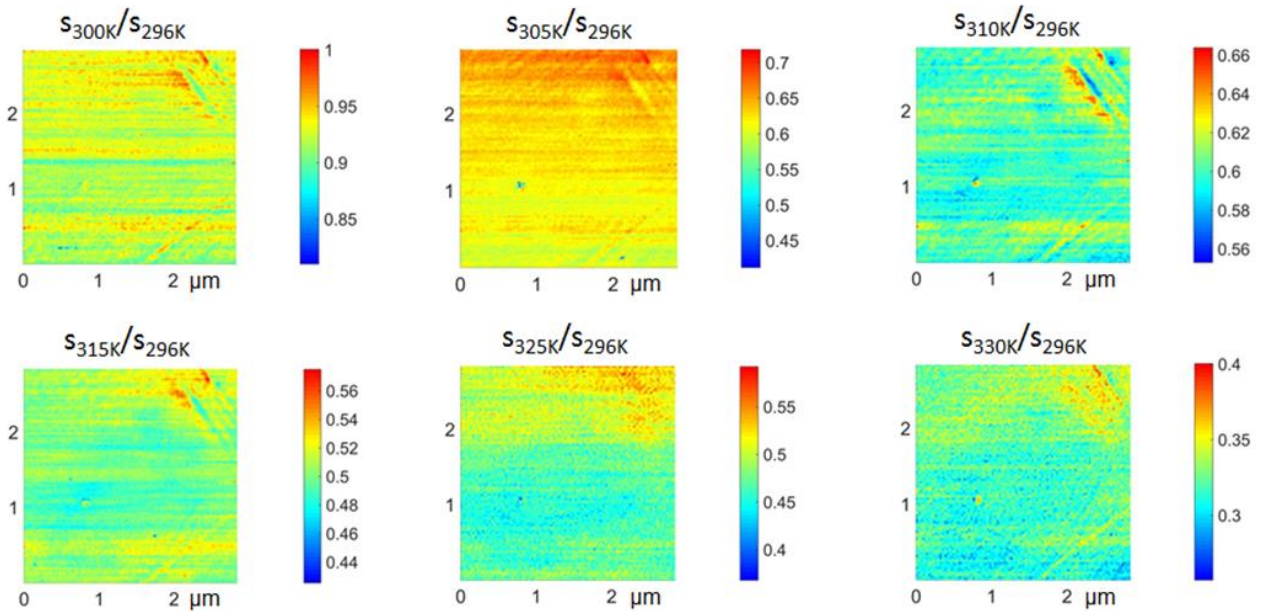


Figure 6.4: The ratios of scans of near-field infrared amplitude “s” for the heating run shown in Figure 6.2. These ratios were obtained by dividing the scans at different temperatures by the scan obtained at room temperature (296 K). Note that each panel has a color scale with different minimum and maximum values so as to clearly show the absence of persistent spatial variation that is evident in the raw scans.

Note that if the static optical contrast was due to the different phases within the main body of the thin film, it will be very hard to fulfill the stringent

constraint that for a broad temperature range, the local static optical contrast between the relatively metallic regions and insulating regions is removed by the normalization of higher temperature data relative to the lowest temperature data taken at 296 K. This is because the dielectric functions of the two different phases are independent and should evolve independently with temperature. Another evidence is that the fluctuation of the optical conductivity measured by infrared near field optical microscopy near the critical temperature of the phase transition between the ferromagnetic metallic phase and the paramagnetic insulating phase is spatially uniform and not affected by the local static optical contrast in figure 6.6 and figure 6.7. (The scan area of figure 6.7 largely overlaps with the one of figure 6.2 and 6.3 with the 5nm island as the spatial marker). Furthermore, the four probe measurement of the temperature dependence of the dc resistivity shown in figure 6.1a mainly measures the properties of the bulk of the 18 nm LSMO thin film. The absence of the hysteresis is also a signature of a uniform spatial phase within the thin film layer without significant phase inhomogeneity. As a result, the most reasonable and direct picture is that, the static optical contrast is generated from the phase inhomogeneity near the interface of the LSMO and STO and the overall continuous change of the optical conductivity during the heating process comes from the spatially uniform phase transition within the main body of the 18 nm LSMO thin film. Note that the interface phase inhomogeneity does not have significant temperature dependence according to figure 6.3.

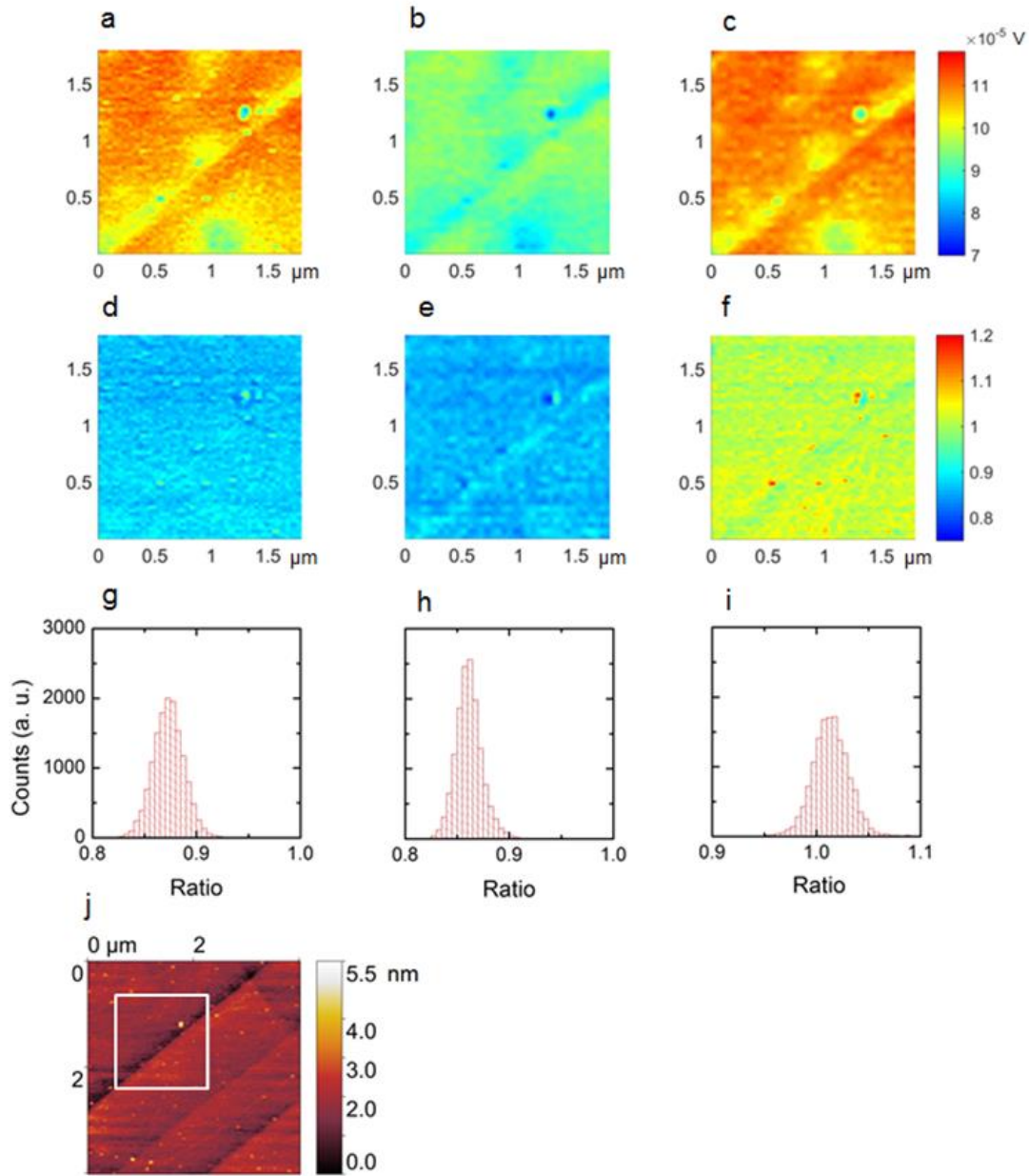


Figure 6.5. Temporal fluctuation in the  $\text{La}_{0.7}\text{Sr}_{0.3}\text{MnO}_3$  thin film at 320K. a, b, c, Scattering near field infrared amplitude obtained from scans in the same area. The scan area is  $1.8 \mu\text{m} \times 1.8 \mu\text{m}$ . Scan b is started 13.3 minutes after scan a is finished and scan c is started 17.4 minutes after scan b is finished. Scans a, b, c are done in the same spatial region and the scan time periods are 8, 4.8 and 4.8 minutes respectively. Panels d, e, f are the ratios of the scattering near field infrared amplitudes shown in a, b, c. Panel d is the ratio of the optical amplitude in panel b divided by the one shown in a. Panel e is the value of the optical amplitude in panel b divided by the one shown in panel c while f is obtained by dividing c by a. Panels g, h, i are histograms of the data shown in d, e, f respectively. Panel j shows the topography measured in a  $4 \mu\text{m} \times 4 \mu\text{m}$  area. The  $1.8 \mu\text{m} \times 1.8 \mu\text{m}$  scan area shown in a, b, c is marked by the white box.

The suggestion of the persistent spatial variation of the near-field infrared amplitude at all temperatures of phase inhomogeneity of the LSMO at the interface with STO is also supported by the data obtained with linear dichroism of X-ray absorption spectroscopy (LD-XAS) in Ref. [103]. The LD-XAS technique finds that for LSMO films less than 6 unit cells grown on STO, the  $3d - e_g (3z^2 - r^2)$  orbital occupation is favored due to symmetry breaking at the interface leading to a C-type antiferromagnetic structure of insulating character. The  $(3z^2 - r^2)$  preferential orbital occupation suppresses the double exchange mechanism which is responsible for the ferromagnetic metallic state in LSMO. For films thicker than 6 unit cells, for example 50 unit cell thickness, LD-XAS finds preferential  $3d - e_g (x^2 - y^2)$  orbital ordering at 300K.

Our s-SNIM data suggests that for our 47 unit cell film, there is persistent, temperature independent phase segregation at the interface leading to some regions of insulating character with  $(3z^2 - r^2)$  orbital occupation that coexist with other regions with  $(x^2 - y^2)$  orbital ordering that are more conducting. The relatively conducting regions cannot be the bulk-like ferromagnetic metallic phase because of the temperature independence of the spatial variation in the infrared contrast. It is likely that the more conducting regions are A-type antiferromagnetic [103] with higher in-plane conductivity compared to the C-type structure. The possibility of phase coexistence at the interface was suggested in Ref. [103,108]. Our work is a direct experimental demonstration of this phenomenon.

Further investigation of the local dynamics of the phase transition in the 47 unit cell thick LSMO film focused on the time dependence of the near-field

infrared amplitude at constant temperature. At a temperature of 320 K, we observe temporal dependence of near-field infrared amplitude as shown in Fig. 6.5. The data shows lower near-field infrared amplitude upon repeating the scan in the same area compared to the first scan. Upon scanning the same area a third time, we find that the near-field infrared amplitude recovers to the same values as in the first scan. This cannot be due to optical drift which is usually monotonic and hardly periodic. Moreover, since the signal change is well above the normal signal fluctuation level of 5%, the temporal variation of the optical amplitude is attributed to the temporal fluctuation of the optical conductivity of LSMO thin film. The time period of the temporal oscillation is of the order of minutes. In other words, we directly observe slow fluctuations of the order parameter in the vicinity of the second order phase transition. Note that our measurement is carried out in zero static magnetic field.

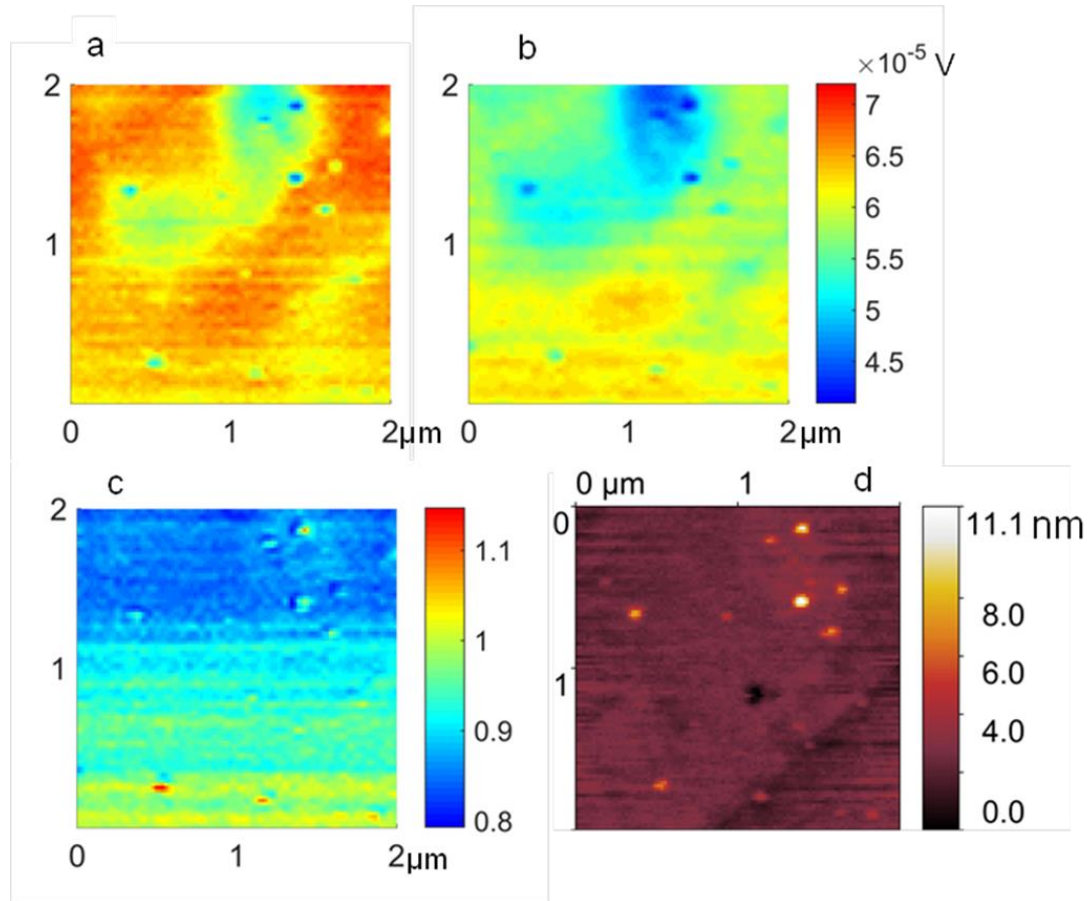


Figure 6.6. Temporal fluctuation in progress in the  $\text{La}_{0.7}\text{Sr}_{0.3}\text{MnO}_3$  thin film at 320K. a,b scattering near field infrared amplitude measured in the same area. The scan area is  $2\ \mu\text{m} \times 2\ \mu\text{m}$ . Note this area is different from the one shown in Fig. 6. 5. Scan b is started 4.6 minutes after scan a is finished. Scan a and b are done in the same spatial region and take 3.3 minutes and 2.7 minutes respectively to complete. Panel c is the ratio of the infrared amplitude in b divided by the one shown in a. d is the topography obtained by AFM in the same region.

Fig. 6.6 shows near-field infrared amplitude scans at 320 K of a region of the film different from that shown in Fig. 6.5. The scans in panels 6.6(a) and 6.6(b) are separated in time and show that the near-field infrared signal is indeed time dependent. Moreover, the ratio of scan (b) to scan (a) shown in 6.6(c) normalizes out the spatial variation of infrared signal due to phase segregation at the interface, and one can see a gradient in the infrared signal. This gradient in

the infrared signal is the result of a change in the infrared conductivity that occurs while data in scan (b) was in the process of being acquired. It returns to unity at the later time shown at the bottom of the figure 6.6(c) and this fact excludes the possibility that this ratio change is due to optical drift. An oscillation-type behavior is observed in figure 6.6(c).

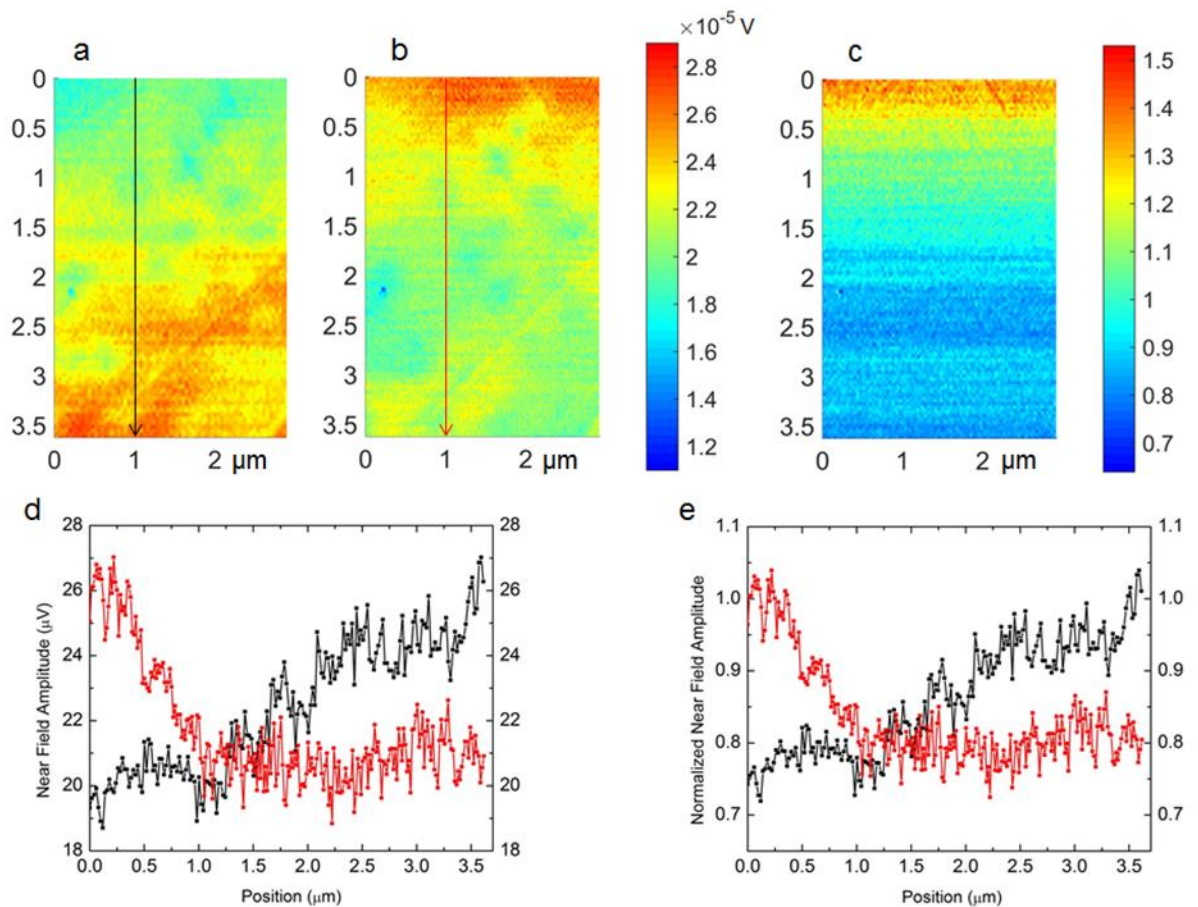


Figure 6.7. Temporal fluctuation in progress in the  $\text{La}_{0.7}\text{Sr}_{0.3}\text{MnO}_3$  thin film at 325 K. a, b near field infrared amplitude scanned in the same area. The scan area is  $2.9 \mu\text{m} \times 3.6 \mu\text{m}$ . Note this area is different from the ones shown in Figures 6.5 and 6.6. Scan b is started 5.4 minutes after scan a is finished. Scan a and b take 12.1 and 19.8 minutes respectively. Panel c is the ratio of the infrared amplitude in b divided by the one shown in a. Black and red plots in d, e are line cuts taken along the black and red lines with arrows shown in figure a and b. The zero value of the position coordinate plotted in d

and e is measured from the base of the arrows depicting the line cuts. The plots in d are the absolute values of the near-field infrared amplitude directly from the linecuts in a and b. The plots in e are obtained by dividing the ones in d by  $26 \mu\text{V}$ , the maximum value of the near-field infrared amplitude in d.

The same phenomenon is observed at 325 K and is shown in Fig. 6.7. Panels 6.7(a) and 6.7(b) are scans of the same area but at different times. The spatial scans in Fig. 6.7 are obtained in a region different from those shown in Fig. 6.5 and Fig. 6.6 but have considerable overlap with the scanned area shown in Fig. 6.2. Once again, scans 6.7(a) and 6.7(b) capture fluctuating conductivity. In scan 6.7(a), the near-field infrared signal is higher in the lower part of the scan area whereas in scan 6.7(b) it is higher in the upper part of the scan area. The ratio of the scans shown in panel (c) and the line cuts shown in panels (d) and (e) further support the observation that the system fluctuates between two states: one of lower conductivity that gives nearly 20% lower infrared signal compared to the state with higher conductivity. Moreover, these observations are reproducible and therefore intrinsic to the LSMO film near the critical temperature of its phase transition.

The timescale of the fluctuation of the infrared conductivity is of the order of minutes. This is extremely slow compared to timescales associated with charge and heat transport. We only observe these slow fluctuations close to the transition temperature of 330 K. We do not observe these fluctuations at room temperature (296 K) which is well below the 330 K phase transition temperature. The near-field infrared amplitude at room temperature is time independent within

5 % uncertainty in our measurements upon repeating the scan in the same area (see figure 6.8).

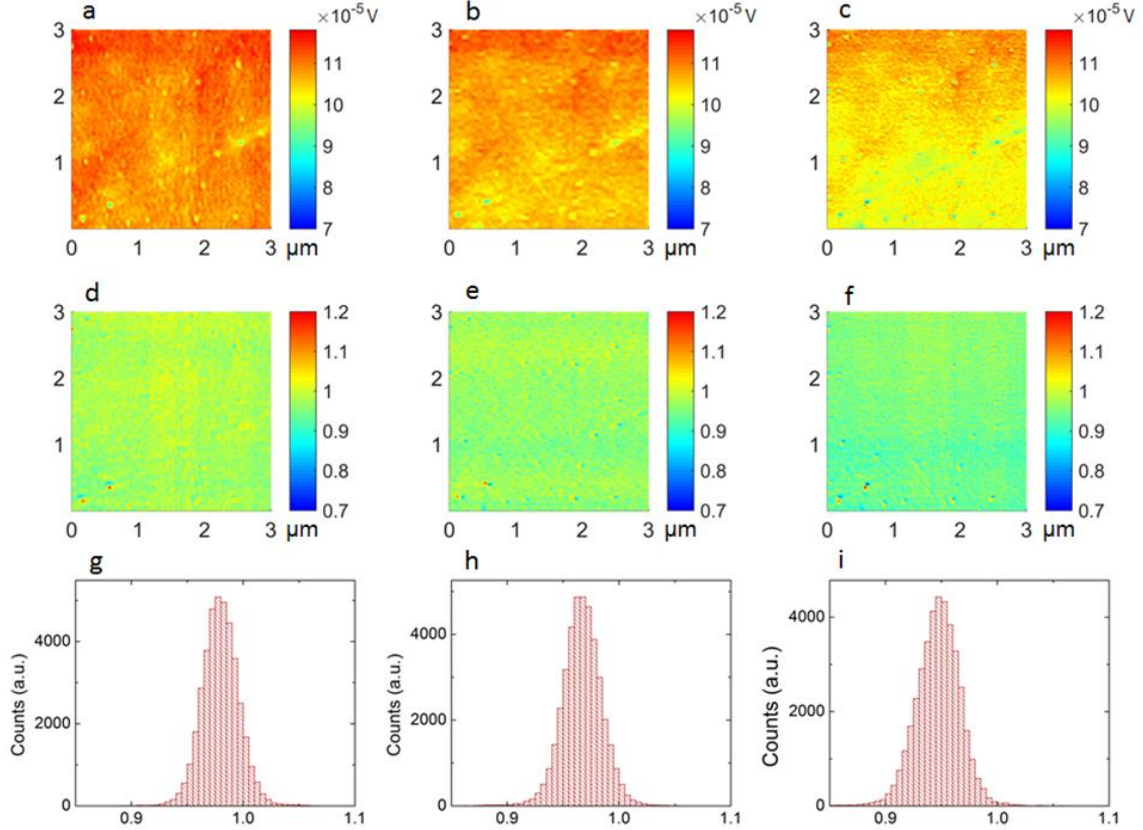


Figure 6.8 a, b, c, Near field infrared amplitude scans at room temperature (296 K) obtained in the same spatial region at different times. Panel d shows the ratio of amplitudes in panel b divided by the ones in a. Panel e shows the ratio of amplitudes in panel c divided by the ones in b, while panel f shows the ratio of amplitudes in c divided by the ones in a. The histogram of the near-field infrared amplitude ratios in panels d, e, f are plotted in panels g, h, i respectively.

Besides the possibility of the fluctuation of the magnetic order parameter which leads to the variation of the conductivity due to the double exchange mechanism, the fluctuation of the orbital ordering between the  $3d e_g (x^2 - y^2)$  state and the superposition of the  $3d e_g (x^2 - y^2)$  and  $3d - e_g (3z^2 - r^2)$  states

which corresponds to the double exchange ferromagnetic metal near the critical temperature may also lead to the variation of the thin film conductivity. However preferential  $3d e_g (x^2 - y^2)$  occupation of  $Mn^{3+}$  is present in the 50 unit cell thick sample measured by the LD-XAS at 300K in ref [103] while the ferromagnetic metal without this orbital ordering emerges at lower temperature. Since the fluctuation of the optical conductivity appears at higher temperature near 330K in our LSMO film according to figure 6.5, 6.6, 6.7 and disappears at 296K as shown in figure 6.8, it is unlikely that this fluctuation of the optical conductivity observed by us is mainly due to orbital order fluctuation.

Charge transport measurements on  $La_{1-x}Ca_xMnO_3$  and  $La_{5/8-y}Pr_yCa_{3/8}MnO_3$  systems have demonstrated temporal fluctuations of the resistivity in the vicinity of their coupled electronic and magnetic phase transitions [109–114]. However, note that the phase transition in these systems is percolative, and the fluctuations observed are notably faster than those observed in our work on LSMO which undergoes a continuous and uniform, non-percolative transition. Slow domain fluctuations on the timescale of minutes have been observed in antiferromagnetic chromium metal by resistivity and X-ray photon correlation spectroscopy[115],[116]. The latter technique found that the domain walls move on the order of micrometers. The dynamical behavior in chromium is attributed to changes in the spin order that occur only in the antiferromagnetic phase below the critical temperature of the weak first-order Neel transition. In LSMO, the slow fluctuations occur between ferromagnetic, more conductive domains and paramagnetic, less conductive domains and this phenomenon is likely related to

critical slowing down close to the critical temperature of the second-order phase transition. Our experimental work provides a rare, direct insight into this phenomenon at microscopic length scales.

## CHAPTER 7

### Conclusions and Outlook

The transport properties of manganites can be significantly modified by temperature, chemical doping, strain, interfacial boundary and similar external perturbations. In this dissertation, we focus on far-field and near-field infrared studies of single crystalline thin films of Sr-doped manganite at 0.33 doping level. At this Sr doping level, the films undergo a thermally induced metal-insulator transition above room temperature. The films were grown on different substrates with different thicknesses by the PLD method.

The temperature dependent far field infrared spectra of 85 nm  $\text{La}_{0.67}\text{Sr}_{0.33}\text{MnO}_3$  thin film grown on (100) LAO substrate is analyzed together with other data in the literature including dc Hall effect measurements, ARPES experiments, electron-positron annihilation work, and thermo-electric properties. Our comprehensive analysis reveals that the electron and hole free carriers behave quite similarly in the low temperature ferromagnetic metallic state of the thin film. Their effective masses are close to the bare electron mass, and their mean free path is above the Ioffe-Regel-Mott limit. If we assume the localized carriers in the mid infrared region have the same effective mass as the free ones, we can reconcile the far infrared to mid infrared spectral weight with the band structure revealed by ARPES and electron-positron annihilation experiments and with Sr chemical doping level. We discover that only one-third of the doped charges are coherent and contribute to dc transport. Two-thirds of the doped

charges are localized and contribute to a broad mid-infrared response. The mid-infrared localization can be attributed to correlation effects and this phenomenon is observed in a number of other correlated electron systems. The temperature dependence of the relaxation rate of free carriers at low temperature fulfills the formula  $A+BT^2$  with anomalously large  $A$  and  $B$  coefficients compared to a simple metal, and this should be related to correlation effects. We detected some of the 8 infrared phonons predicted for the rhombohedral lattice. The splitting of the  $580\text{ cm}^{-1}$  infrared phonon at high temperatures is observed and we explain it with differing bond lengths induced by the local Jahn-Teller distortion.

We also performed scattering near-field optical microscopy at a mid-infrared wavelength of  $10.8\ \mu\text{m}$  on  $18\text{ nm}$  thick  $\text{La}_{0.67}\text{Sr}_{0.33}\text{MnO}_3$  film grown on (100) STO substrate. In contrast to the first-order metal-insulator transition in  $\text{VO}_2$ , no percolation is discovered when LSMO is heated up from the room temperature to  $330\text{ K}$  near the critical temperature of the second order phase transition of the ferromagnetic metal to paramagnetic insulator. A continuous, non-percolative phase transition is observed within the bulk of the thin film. Furthermore, slow, time-dependent critical fluctuations are discovered at fixed temperatures near  $330\text{ K}$  and these disappear near room temperature. Temperature independent phase separation at the film-substrate interface is identified. This is probably related to nanoscale coexistence between the more conducting regions with A-type antiferromagnetic order and the less conducting ones with C-type antiferromagnetic structure.

The far field optical detection method is constrained by the diffraction limit

and only a spatially averaged optical response of the sample can be obtained. This makes measurement of spatially varying nanoscale properties of inhomogeneous materials difficult. Thin film samples with varying thicknesses on different substrates can lead to material properties that are spatially inhomogeneous in the lateral or perpendicular direction of the film surface. Scanning near-field infrared microscopy is an indispensable tool for obtaining direct and accurate physical understanding of certain important phenomena such as nanoscale inhomogeneity, percolative-type phase transitions, real space critical fluctuations, surface plasmons etc. with nanoscale spatial resolution. In order to obtain frequency-dependent information on the above-mentioned physical phenomena, we are developing broadband infrared nano-spectroscopy with our nano-FTIR setup. Moreover, we are testing numerical modeling methods for obtaining the local dielectric function from the spectroscopy data.

- [1] Dagotto E 2003 *Nanoscale Phase Separation and Colossal Magnetoresistance The physics of Manganites and Related Compounds* (Berlin Heidelberg New York: Springer-Verlag)
- [2] Dagotto E, Hotta T and Moreo A 2001 Colossal magnetoresistant materials: the key role of phase separation *Phys. Rep.* **344** 1–153
- [3] Haghiri-Gosnet A-M and Renard J-P 2003 CMR manganites : physics , thin films and devices *J. Phys. D Appl. Phys.* **36** R127–50
- [4] Dressel M and Scheffler M 2006 Verifying the Drude response *Ann. Phys.* **15** 535–44
- [5] Dressel M and Gruner G 2002 *Electrodynamics of Solids: Optical Properties of Electrons in Matter* (Cambridge, United Kingdom: Cambridge University Press)
- [6] Ferlauto A S, Ferreira G M, Pearce J M, Wronski C R, Collins R W, Deng X and Ganguly G 2002 Analytical model for the optical functions of amorphous semiconductors from the near-infrared to ultraviolet: Applications in thin film photovoltaics *J. Appl. Phys.* **92** 2424–36
- [7] Basov D N, Averitt R D, van der Marel D, Dressel M and Haule K 2011 Electrodynamics of correlated electron materials *Rev. Mod. Phys.* **83** 471–541
- [8] Millis A J 1998 Lattice effects in magnetoresistive manganese perovskites *Nature* **392** 147–50

- [9] Takenaka K, Shiozaki R and Sugai S 2002 Charge dynamics of a double-exchange ferromagnet  $\text{La}_{1-x}\text{Sr}_x\text{MnO}_3$  *Phys. Rev. B* **65** 184436
- [10] Okimoto Y, Katsufuji T, Ishikawa T, Arima T and Tokura Y 1997 Variation of electronic structure in  $\text{La}_{1-x}\text{Sr}_x\text{MnO}_3$  as investigated by optical conductivity spectra *Phys. Rev. B* **55** 4206–14
- [11] Millis A J, Littlewood P B and Shraiman B I 1995 Double Exchange Alone Does Not Explain the Resistivity of  $\text{La}_{1-x}\text{Sr}_x\text{MnO}_3$  *Phys. Rev. Lett.* **74** 5144–7
- [12] Haghiri-Gosnet A, Koubaa M, Santander-Syro A, Lobo R, Lecoeur P and Mercey B 2008 Metallic nature of strained thin single-crystal  $\text{La}_{2/3}\text{Sr}_{1/3}\text{MnO}_3$  films *Phys. Rev. B* **78** 115118
- [13] Jung J H, Kim K H, Noh T W, Choi E J and Yu J 1998 Midgap states of  $\text{La}_{1-x}\text{Ca}_x\text{MnO}_3$ : Doping-dependent optical-conductivity studies *Phys. Rev. B* **57** 11043–6
- [14] Quijada M, Cerne J, Simpson J R, Drew H D, Ahn K H, Millis A J, Shreekala R, Ramesh R, Rajeswari M and Venkatesan T 1998 Optical conductivity of manganites: Crossover from Jahn-Teller small polaron to coherent transport in the ferromagnetic state *Phys. Rev. B* **58** 16093–102
- [15] Hartinger C, Mayr F, Loidl A and Kopp T 2004 Cooperative dynamics in doped manganite films: Phonon anomalies in the ferromagnetic state *Phys. Rev. B* **70** 134415

- [16] Hartinger C, Mayr F, Loidl A and Kopp T 2005 Phonon metamorphosis in ferromagnetic manganite films: Probing the evolution of an inhomogeneous state *Phys. Rev. B* **71** 184421
- [17] Dore P, Funaro A, Sacchetti A, Angeloni M and Balestrino G 2003 Study of infrared phonons in the  $\text{La}_{0.7}\text{Sr}_{0.3}\text{MnO}_3$  manganite by means of reflectance measurements on epitaxial films *Eur. Phys. J. B - Condens. Matter* **37** 339–44
- [18] Simpson J, Drew H, Smolyaninova V, Greene R, Robson M, Biswas A and Rajeswari M 1999 Temperature-dependent scattering rate and optical mass of ferromagnetic metallic manganites *Phys. Rev. B* **60** R16263–6
- [19] Zhang L W, Israel C, Biswas A, Greene R L and de Lozanne A 2002 Direct observation of percolation in a manganite thin film *Science* (80-. ). **298** 805–7
- [20] Kanki T, Li R W, Naitoh Y, Tanaka H, Matsumoto T and Kawai T 2003 Nanoscale observation of room-temperature ferromagnetism on ultrathin  $(\text{La},\text{Ba})\text{MnO}_3$  films *Appl. Phys. Lett.* **83** 1184–6
- [21] Biswas A, Rajeswari M, Srivastava R C, Venkatesan T, Greene R L, Lu Q, de Lozanne A and Millis A J 2001 Strain-driven charge-ordered state in  $\text{La}_{0.67}\text{Ca}_{0.33}\text{MnO}_3$  *Phys. Rev. B* **63** 184424
- [22] Bakaul S R, Lin W and Wu T 2011 Evolution of magnetic bubble domains in manganite films *Appl. Phys. Lett.* **99** 42503

- [23] Bakaul S R, Miao B F, Lin W, Hu W, David A, Ding H F and Wu T 2012 Domain-related origin of magnetic relaxation in compressively strained manganite thin films *Appl. Phys. Lett.* **101** 12408
- [24] Bakaul S R, Hu W, Wu T and Kimura T 2012 Intrinsic domain-wall resistivity in half-metallic manganite thin films *Phys. Rev. B - Condens. Matter Mater. Phys.* **86** 184404
- [25] Dho J, Kim Y N, Hwang Y S, Kim J C and Hur N H 2003 Strain-induced magnetic stripe domains in  $\text{La}_{0.7}\text{Sr}_{0.3}\text{MnO}_3$  thin films *Appl. Phys. Lett.* **82** 1434–6
- [26] Desfeux R, Bailleul S, Da Costa A, Prellier W and Haghiri-Gosnet A M 2001 Substrate effect on the magnetic microstructure of  $\text{La}_{0.7}\text{Sr}_{0.3}\text{MnO}_3$  thin films studied by magnetic force microscopy *Appl. Phys. Lett.* **78** 3681–3
- [27] Landau L D and Lifshitz E 1980 *Statistical Physics* (Butterworth-Heinemann)
- [28] Becker T, Streng C, Luo Y, Moshnyaga V, Damaschke B, Shannon N and Samwer K 2002 Intrinsic inhomogeneities in manganite thin films investigated with scanning tunneling spectroscopy *Phys. Rev. Lett.* **89** 237203
- [29] Fath M, Freisem S, Menovsky A A, Tomioka Y, Aarts J and Mydosh J A 1999 Spatially inhomogeneous metal-insulator transition in doped manganites *Science* (80-. ). **285** 1540–2

- [30] Born M and Wolf E 1999 *Principles of Optics: Electromagnetic Theory of Propagation, Interference and Diffraction of Light* (Cambridge: Cambridge University Press)
- [31] Knoll B and Keilmann F 1999 Electromagnetic fields in the cutoff regime of tapered metallic waveguides *Opt. Commun.* **162** 177–81
- [32] Keilmann F and Hillenbrand R 2004 Near-field microscopy by elastic light scattering from a tip *Philos. Trans. A. Math. Phys. Eng. Sci.* **362** 787–805
- [33] Hemberger J, Krimmel A, Kurz T, Krug von Nidda H -a., Ivanov V, Mukhin A, Balbashov A and Loidl A 2002 Structural, magnetic, and electrical properties of single-crystalline  $\text{La}_{1-x}\text{Sr}_x\text{MnO}_3$  ( $0.4 < x < 0.85$ ) *Phys. Rev. B* **66** 94410
- [34] Xu P, Huffman T J, Branagan N C, Qazilbash M M, Srivastava P, Goehringer T, Yong G, Smolyaninova V and Kolagani R 2015 Novel aspects of charge and lattice dynamics in the hole-doped manganite  $\text{La}_{0.67}\text{Sr}_{0.33}\text{MnO}_3$  *Philos. Mag.* **95** 2078
- [35] Tsui F, Smoak M C, Nath T K and Eom C B 2000 Strain-dependent magnetic phase diagram of epitaxial  $\text{La}_{(0.67)}\text{Sr}_{(0.33)}\text{MnO}_{(3)}$  thin films *Appl. Phys. Lett.* **76** 2421–3
- [36] Huijben M, Martin L W, Chu Y-H, Holcomb M B, Yu P, Rijnders G, Blank D H A and Ramesh R 2008 Critical thickness and orbital ordering in ultrathin  $\text{La}_{0.7}\text{Sr}_{0.3}\text{MnO}_3$  films *Phys. Rev. B* **78** 094413

- [37] Zhang M, Ma X L, Li D X, Lü H B, Chen Z H and Yang G Z 2003 Microdomains in thin films of rhombohedral  $\text{La}_{0.7}\text{Sr}_{0.3}\text{MnO}_3$  *Phys. Status Solidi* **196** 365–71
- [38] Sedykh V, Shekhtman V S, Zverkova I, Dubovitskii A and Kulakov V 2006 Reversibility of structure phase transitions in  $\text{LaMnO}_{3+\delta}$  manganite under heat treatment *Phys. C* **433** 189–94
- [39] Aruta C, Ghiringhelli G, Tebano A, Boggio N G, Brookes N B, Medaglia P G and Balestrino G 2006 Strain induced x-ray absorption linear dichroism in  $\text{La}_{0.7}\text{Sr}_{0.3}\text{MnO}_3$  thin films *Phys. Rev. B* **73** 235121
- [40] Huang Q, Santoro A, Lynn J W, Erwin R W, Borchers J A, Peng J L and Greene R L 1997 Structure and magnetic order in undoped lanthanum manganite *Phys. Rev. B* **55** 14987–99
- [41] Iliev M N and Abrashev M V. 2001 Raman phonons and Raman Jahn-Teller bands in perovskite-like manganites *J. Raman Spectrosc.* **32** 805–11
- [42] Jonker G H and Van Santen J H 1950 Ferromagnetic compounds of manganese with perovskite structure *Physica* **16** 337–49
- [43] Zener C 1951 Interaction between the d-shells in the transition metals. II. Ferromagnetic compounds of manganese with Perovskite structure *Phys. Rev.* **82** 403–5
- [44] Anderson P W and Hasegawa H 1955 Considerations on Double Exchange *Phys. Rev.* **100** 675–81

- [45] Reznik D, Bourges P, Fong H, Regnault L, Bossy J, Vettier C, Milius D, Aksay I and Keimer B 1996 Direct observation of optical magnons in  $\text{YBa}_2\text{Cu}_3\text{O}_{6.2}$  *Phys. Rev. B* **53** R14741
- [46] Wadati H, Yoshida T, Chikamatsu A, Kumigashira H, Oshima M, Eisaki H, Shen Z-X, Mizokawa T and Fujimori A 2006 Angle-resolved photoemission spectroscopy of perovskite-type transition-metal oxides and their analyses using tight-binding band structure *Phase Transitions* **79** 617–635
- [47] Fishman R and Jarrell M 2003 Magnetic susceptibility of the double-exchange model *Phys. Rev. B* **67**100403(R)
- [48] Bocquet A E, Mizokawa T, Saitoh T, Namatame H and Fujimori A 1992 Electronic-Structure of 3d-Transition-Metal Compounds by Analysis of the 2p Core-Level Photoemission Spectra *Phys. Rev. B* **46** 3771–84
- [49] Griffiths F and de Haseth J 2007 *Fourier Transform Infrared Spectrometry* (Hoboken, NJ: John Wiley and Sons, Inc.)
- [50] Chamberlain J, Gibbs J E and Gebbie H A 1969 The determination of refractive index spectra by fourier spectrometry *Infrared Phys.* **9** 185–209
- [51] Brooker D J 2012 *Infrared Reflectance of Materials at Elevated and Cryogenic Temperatures* (College of William and Mary)
- [52] Anon 2010 *WVASE32* (Lincoln, NE: J.A. Woollam Co. Inc.)
- [53] Ash E A and Nicholls G 1972 Super-Resolution Aperture Scanning Microscope *Nature* **237**510--

- [54] Ben-Aryeh Y 2013 Super-resolution measurements related to uncertainty relations in optical and biological fluorescence systems *J. Quant. Spectrosc. Radiat. Transf.* **131** 43–51
- [55] Knoll B and Keilmann F 2000 Enhanced dielectric contrast in scattering type scanning near field optical microscopy *Opt. Commun.* **182** 321–8
- [56] Ocelic N, Huber A and Hillenbrand R 2006 Pseudoheterodyne detection for background-free near-field spectroscopy *Appl. Phys. Lett.* **89** 101124
- [57] Hillenbrand R and Keilmann F 2000 Complex optical constants on a subwavelength scale *Phys. Rev. Lett.* **85** 3029–32
- [58] Sun J, Carney P S and Schotland J C 2007 Strong tip effects in near-field scanning optical tomography *J. Appl. Phys.* **102** 103103
- [59] Maradudin A A and Mills L L 1975 Scattering and absorption of electromagnetic radiation by a semi-infinite medium in the presence of surface roughness *Phys.Rev.B* **11** 1392
- [60] Frenzel A, Qazilbash M M, Brehm M, Chae B-G, Kim B-J, Kim H-T, Balatsky A V, Keilmann F and Basov D N 2009 Inhomogeneous electronic state near the insulator-to-metal transition in the correlated oxide VO<sub>2</sub> *Phys. Rev. B* **80** 115115
- [61] Török P, Munro P R T and Kriezis E E 2006 Rigorous near- to far-field transformation for vectorial diffraction calculations and its numerical implementation. *J. Opt. Soc. Am. A. Opt. Image Sci. Vis.* **23** 713–22

- [62] Jones A C and Raschke M B 2012 Thermal infrared near-field spectroscopy *Nano Lett.* **12** 1475–81
- [63] Govyadinov A a, Mastel S, Golmar F, Chuvilin A, Carney P S and Hillenbrand R 2014 Recovery of Permittivity and Depth from Near-Field Data as a Step toward Infrared Nanotomography. *ACS Nano* **8** 6911
- [64] Cvitkovic A, Ocelic N and Hillenbrand R 2007 Analytical model for quantitative prediction of material contrasts in scattering-type near-field optical microscopy *Opt. Express* **15** 8550–65
- [65] Ishikawa M, Katsura M, Nakashima S, Ikemoto Y and Okamura H 2012 Broadband near-field mid-infrared spectroscopy and application to phonon resonances in quartz *Opt. Express* **20** 11064
- [66] Novotny L, Bian R X and Xie X S 1997 Theory of nanometric optical tweezers *Phys. Rev. Lett.* **79** 645–8
- [67] Chikamatsu A, Wadati H, Kumigashira H, Oshima M, Fujimori A, Lippmaa M, Ono K, Kawasaki M and Koinuma H 2007 Gradual disappearance of the Fermi surface near the metal-insulator transition in  $\text{La}_{1-x}\text{Sr}_x\text{MnO}_3$  thin films *Phys. Rev. B* **76**201103R
- [68] Krempaský J, Strocov V, Patthey L, Willmott P, Herger R, Falub M, Blaha P, Hoesch M, Petrov V, Richter M, Heckmann O and Hricovini K 2008 Effects of three-dimensional band structure in angle- and spin-resolved photoemission from half-metallic  $\text{La}_{2/3}\text{Sr}_{1/3}\text{MnO}_3$  *Phys. Rev. B* **77** 165120

- [69] Chikamatsu a., Wadati H, Kumigashira H, Oshima M, Fujimori A, Hamada N, Ohnishi T, Lippmaa M, Ono K, Kawasaki M and Koinuma H 2006 Band structure and Fermi surface of  $\text{La}_{0.6}\text{Sr}_{0.4}\text{MnO}_3$  thin films studied by in situ angle-resolved photoemission spectroscopy *Phys. Rev. B* **73** 195105
- [70] Krempaský J, Strocov V N, Blaha P, Patthey L, Radović M, Falub M, Shi M and Hricovini K 2010 Bulk vs. surface effects in ARPES experiment from  $\text{La}_{2/3}\text{Sr}_{1/3}\text{MnO}_3$  thin films *J. Electron Spectros. Relat. Phenomena* **181** 63–9
- [71] Livesay E A, West R N, Dugdale S B, Santi G and Jarlborg T 1999 Fermi surface of the colossal magnetoresistance perovskite  $\text{La}_{0.7}\text{Sr}_{0.3}\text{MnO}_3$  *J. Phys. Condens. Matter* **11** L279–85
- [72] Dildar I M, Beekman C, He X and Aarts J 2012 Hall effect measurements on strained and unstrained thin films of  $\text{La}_{0.7}\text{Ca}_{0.3}\text{MnO}_3$  and  $\text{La}_{0.7}\text{Sr}_{0.3}\text{MnO}_3$  *Phys. Rev. B* **85** 205103
- [73] Asamitsu a, Moritomo Y and Tokura Y 1996 Thermoelectric effect in  $\text{La}_{1-x}\text{Sr}_x\text{MnO}_3$ . *Phys. Rev. B. Condens. Matter* **53** R2952–5
- [74] Pickett W E and Singh D J 1997 Transport and fermiology of the ferromagnetic phase of  $\text{La}_{2/3}\text{A}_{1/3}\text{MnO}_3$  ( A = Ca , Sr , Ba ) *J. Magn. Magn. Mater.* **172** 237–46
- [75] Asamitsu A and Tokura Y 1998 Hall effect in  $\text{La}_{1-x}\text{Sr}_x\text{MnO}_3$  *Phys.Rev.B* **58** 47–50
- [76] Jellison G E and Modine F a. 1996 Parameterization of the optical

functions of amorphous materials in the interband region *Appl. Phys. Lett.*  
**69** 371

- [77] Hashimoto T, Hirasawa R, Yoshida T, Yonemura Y, Mizusaki J and Tagawa H 1995 Coexistence of electrons and holes in  $\text{BaBi}_{0.25}\text{Pb}_{0.75}\text{O}_{3-d}$  detected by thermoelectric-power measurements *Phys.Rev.B* **51** 576
- [78] Salamon M B and Jaime M 2001 The physics of manganites: Structure and transport *Rev. Mod. Phys.* **73** 583–628
- [79] Bakaul S R, Hu W, Wu T and Kimura T 2012 Intrinsic domain-wall resistivity in half-metallic manganite thin films *Phys. Rev. B - Condens. Matter Mater. Phys.* **86** 1–5
- [80] Xu W, Haule K and Kotliar G 2013 Hidden Fermi Liquid, Scattering Rate Saturation, and Nernst Effect: A Dynamical Mean-Field Theory Perspective *Phys. Rev. Lett.* **111** 36401
- [81] Nazarov V U, Vignale G and Chang Y-C 2014 Dynamical many-body corrections to the residual resistivity of metals *Phys. Rev. B* **89** 241108
- [82] Abrashev M V, Litvinchuk A P, Iliiev M N, Meng R L, Popov V N, Ivanov V G, Chakalov R A and Thomsen C 1999 Comparative study of optical phonons in the rhombohedrally distorted perovskites  $\text{LaAlO}_3$  and  $\text{LaMnO}_3$  *Phys. Rev. B* **59** 4146–53
- [83] Zhang M, Ma \* X L and Li D X 2005 Crystallographic study of the rhombohedral-oriented domains in a  $\text{La}_{0.7}\text{Sr}_{0.3}\text{MnO}_3$  film *Philos. Mag.* **85**

1625–36

- [84] Delugas P, Fiorentini V and Filippetti A 2005 Dielectric properties and long-wavelength optical modes of the high- $\kappa$  oxide  $\text{LaAlO}_3$  *Phys. Rev. B* **71** 134302
- [85] Last J T 1957 Infrared absorption studies on Barium Titanate and Related Materials *Phys.Rev.* **105** 1740
- [86] Shibata T, Bunker B and Mitchell J 2003 Local distortion of  $\text{MnO}_6$  clusters in the metallic phase of  $\text{La}_{1-x}\text{Sr}_x\text{MnO}_3$  *Phys. Rev. B* **68** 24103
- [87] Louca D and Egami T 1999 Local lattice distortions in  $\text{La}_{1-x}\text{Sr}_x\text{MnO}_3$  studied by pulsed neutron scattering *Phys. Rev. B* **59** 6193–204
- [88] Louca D, Egami T, Brosha E L, Roder H and Bishop A R 1997 Local Jahn-Teller distortion in  $\text{La}_{1-x}\text{Sr}_x\text{MnO}_3$  observed by pulsed neutron diffraction *Phys. Rev. B* **56** R8475--R8478
- [89] Barker A S, Ditzemberger J and Guggenheim H J 1968 Long-Wavelength Optical Lattice Vibrations in Mixed  $\text{KMgF}_3$ - $\text{KNiF}_3$  Crystals *Phys. Rev.* **175** 1180
- [90] Dagotto E 2010 *Nanoscale Phase Separation and Colossal Magnetoresistance in Manganites* (Springer)
- [91] Vescovo E, Park J H, Vescovo E, Kim H J, Kwon C, Ramesh R and Venkatesan T 1998 Direct evidence for a half-metallic ferromagnet *Nature* **392** 794–6

- [92] Okimoto Y, Katsufuji T, Ishikawa T, Arima T and Tokura Y 1997 Variation of electronic structure in  $\text{La}_{1-x}\text{Sr}_x\text{MnO}_3$  ( $0 \leq x \leq 0.3$ ) as investigated by optical conductivity spectra *Phys. Rev. B* **55** 4206–14
- [93] Desfeux R, Bailleul S, Da Costa A, Prellier W and Haghiri-Gosnet A M 2001 Substrate effect on the magnetic microstructure of  $\text{La}_{0.7}\text{Sr}_{0.3}\text{MnO}_3$  thin films studied by magnetic force microscopy *Appl. Phys. Lett.* **78** 3681–3
- [94] Becker T, Streng C, Luo Y, Moshnyaga V, Damaschke B, Shannon N and Samwer K 2002 Intrinsic inhomogeneities in manganite thin films investigated with scanning tunneling spectroscopy. *Phys. Rev. Lett.* **89** 237203
- [95] Liebmann M, Kaiser U, Schwarz a, Wiesendanger R, Pi U ., Noh T ., Khim Z . and Kim D-W 2004 Tilted magnetization of a  $\text{La}_{0.7}\text{Sr}_{0.3}\text{MnO}_3/\text{LaAlO}_3$  (001) thin film *J. Magn. Magn. Mater.* **280** 51–9
- [96] Dho J and Hur N H 2007 Thickness dependence of perpendicular magnetic anisotropy in  $\text{La}_{0.7}\text{Sr}_{0.3}\text{MnO}_3$  films on  $\text{LaAlO}_3$  *J. Magn. Magn. Mater.* **318** 23–7
- [97] Jiang Y, Gao G Y, Wang Y and Chan H L W 2010 Temperature evolution of anisotropic stress induced highly ordered stripe magnetic domains in  $\text{La}_{0.7}\text{Sr}_{0.3}\text{MnO}_3$  thin film on (110)  $\text{NdGaO}_3$  substrate *Solid State Commun.* **150** 2028–31
- [98] Houwman E P, Maris G, De Luca G M, Niermann N, Rijnders G, Blank D

- H A and Speller S 2008 Out-of-plane magnetic domain structure in a thin film of  $\text{La}_{0.67}\text{Sr}_{0.33}\text{MnO}_3$  on  $\text{SrTiO}_3$  (001) observed by magnetic force microscopy *Phys. Rev. B* **77** 184412
- [99] Liebmann M, Schwarz A, Kaiser U, Wiesendanger R, Kim D W and Noh T W 2005 Magnetization reversal of a structurally disordered manganite thin film with perpendicular anisotropy *Phys. Rev. B - Condens. Matter Mater. Phys.* **71** 1–9
- [100] Olson T W, Olson J M W, Scholl A and Suzuki Y 2004 Magnetic domain structure of colossal magnetoresistance thin films and islands *J. Appl. Phys.* **95** 7354–6
- [101] Bakaul S R, Lin W and Wu T 2011 Evolution of magnetic bubble domains in manganite films *Appl. Phys. Lett.* **99** 2011–4
- [102] Sidorenko A A, Allodi G, De Renzi R, Balestrino G and Angeloni M 2006 Mn55 NMR and magnetization studies of  $\text{La}_{0.67}\text{Sr}_{0.33}\text{MnO}_3$  thin films *Phys. Rev. B - Condens. Matter Mater. Phys.* **73** 1–7
- [103] Tebano A, Aruta C, Sanna S, Medaglia P G, Balestrino G, Sidorenko A A, De Renzi R, Ghiringhelli G, Braicovich L, Bisogni V and Brookes N B 2008 Evidence of orbital reconstruction at interfaces in ultrathin  $\text{La}_{0.67}\text{Sr}_{0.33}\text{MnO}_3$  Films *Phys. Rev. Lett.* **100** 2–5
- [104] Aruta C, Ghiringhelli G, Bisogni V, Braicovich L, Brookes N B, Tebano A and Balestrino G 2009 Orbital occupation, atomic moments, and magnetic

ordering at interfaces of manganite thin films *Phys. Rev. B - Condens. Matter Mater. Phys.* **80** 1–8

- [105] Tebano A, Orsini A, Medaglia P G, Di Castro D, Balestrino G, Freelon B, Bostwick A, Chang Y J, Gaines G, Rotenberg E and Saini N L 2010 Preferential occupation of interface bands in  $\text{La}_{2/3}\text{Sr}_{1/3}\text{MnO}_3$  films as seen via angle-resolved photoemission *Phys. Rev. B - Condens. Matter Mater. Phys.* **82** 1–5
- [106] Lee J S, Arena D A, Yu P, Nelson C S, Fan R, Kinane C J, Langridge S, Rossell M D, Ramesh R and Kao C C 2010 Hidden magnetic configuration in epitaxial  $\text{La}_{1-x}\text{Sr}_x\text{MnO}_3$  films *Phys. Rev. Lett.* **105** 1–4
- [107] Lee J S, Arena D A, Santos T S, Nelson C S, Hyun S I, Shim J H and Kao C C 2012 Controlling competing interactions at oxide interfaces: Enhanced anisotropy in  $\text{La}_{0.7}\text{Sr}_{0.3}\text{MnO}_3$  films via interface engineering *Phys. Rev. B - Condens. Matter Mater. Phys.* **85** 1–5
- [108] Brey L 2007 Electronic phase separation in manganite-insulator interfaces *Phys. Rev. B - Condens. Matter Mater. Phys.* **75** 1–7
- [109] Ward T Z, Zhang X G, Yin L F, Zhang X Q, Liu M, Snijders P C, Jesse S, Plummer E W, Cheng Z H, Dagotto E and Shen J 2009 Time-resolved electronic phase transitions in manganites *Phys. Rev. Lett.* **102** 10–3
- [110] Merithew R, Weissman M, Hess F, Spradling P, Nowak E, O'Donnell J, Eckstein J, Tokura Y and Tomioka Y 2000 Mesoscopic Thermodynamics of

an Inhomogeneous Colossal-Magnetoresistive Phase *Phys. Rev. Lett.* **84**  
3442–5

- [111] Podzorov V, Gershenson M E, Uehara M and Cheong S-W 2001 Phase separation and 1/f noise in low- $T_{MI}$  colossal magnetoresistance manganites *Phys. Rev. B* **64** 115113
- [112] Podzorov V, Chen C H, Gershenson M E and Cheong S-W 2001 Mesoscopic, non-equilibrium fluctuations of inhomogeneous electronic states in manganites *Europhys. Lett.* **55** 411–7
- [113] Palanisami A, Weissman M B and Mathur N D 2005 Magnetoresistive dynamics and noise in low-strain manganite films *Phys. Rev. B - Condens. Matter Mater. Phys.* **71** 1–7
- [114] Raquet B, Anane A, Wirth S, Xiong P and von Molnár S 2000 Noise Probe of the Dynamic Phase Separation in  $\text{La}_{2/3}\text{Ca}_{1/3}\text{MnO}_3$  *Phys. Rev. Lett.* **84**  
4485–8
- [115] Michel R P, Israeloff N E, Weissman M B, Dura J A and Flynn C P 1991 Electrical-noise measurements on chromium films *Phys. Rev. B* **44** 7413–25
- [116] Shpyrko O G, Isaacs E D, Logan J M, Feng Y, Aeppli G, Jaramillo R, Kim H C, Rosenbaum T F, Zschack P, Sprung M, Narayanan S and Sandy a R 2007 Direct measurement of antiferromagnetic domain fluctuations. *Nature* **447** 68–71